University of Alberta

Library Release Form

Name of Author: Evan Bianco

Title of Thesis: Seismic rock physics of steam injection

Degree: Master of Science

Year this Degree Granted: 2008

_____

Evan Bianco

University of Alberta

SEISMIC ROCK PHYSICS OF STEAM INJECTION IN BITUMINOUS OIL SAND RESERVOIRS

by

Evan Bianco

A thesis submitted to the Faculty of Graduate Studies and Research in partial fulfillment of the requirements for the degree of **Master of Science**

Department of Physics

Edmonton, Alberta, 2008

University of Alberta

Faculty of Graduate Studies and Research

The undersigned certify that they have read, and recommend to the Faculty of Graduate Studies and Research for acceptance, a thesis entitled **Seismic rock physics of steam injection** submitted by Evan Bianco in partial fulfillment of the requirements for the degree of **Master of Science**.

_____
Dr. Douglas Schmitt

_____
Dr. Mauricio Sacchi

_____
Dr. Douglas Gingrich

_____
Dr. Rick Chalaturnyk

Date: _____

Dedication

To Dan, Arlene, and Tara

Abstract

This thesis explores the seismic rock physics pertaining to oil sands reservoirs subject to the Steam Assisted Gravity Drainage (SAGD) thermal enhanced recovery process. Rock physics modeling is applied to the shallow McMurray reservoir (135-160 m depth) encountered by the Underground Test Facility (UTF) within the bituminous Athabasca oil sands deposit in Western Canada in order to construct a petrophysical velocity model of the SAGD process. Injected steam pressure and temperature controls the fluid bulk moduli within the pore space, and the stress dependant elastic frame modulus is the most poorly known yet most important factor governing the changes of seismic properties during this recovery operation. The results of the fluid substitution are used to construct a 2D synthetic seismic section in order to establish seismic attributes for analysis and interpretation of the physical SAGD process. The findings of this modeling promote a more complete description of 11 high resolution time lapse 2-D seismic profiles collected at the UTF by the University of Alberta.

Acknowledgements

My first official introduction to the oil sands was in the summer of 2004, when I landed a summer student job in the Long Lake business unit at Nexen Inc. Thanks to Laurie Bellman, my boss that summer, for introducing me to the practical aspects of seismic rock physics. I think I get the point now! At that time, the industry majors in Canada had only pilot in-situ projects underway, and only a few companies had any commercial production. Now, as I submit my thesis for graduation, I am amazed (just as everyone else is) by the rapid development of the Western Canadian oil sands. It seems impossible to flip through the newspaper today without finding an article headlining one of the many issues related to the oil sands. It has become mainstream, en vogue, criticized and cheered, protested and praised. Surely, the shear immensity of this resource will ensure that it remains a heated topic in global economic, environmental, and energy circles. I feel privileged that my thesis may in fact be conveniently well timed, and the subject of a thriving topic where there is still much to learn.

I wish to thank my Supervisor, Doug Schmitt, for supporting me and guiding me through my studies. Doug has been more than a research supervisor, he has been an academic role model and it has been a lot of fun traveling around the world with him to do seismic experiments. And I couldn't think of more exotic places!; Outokumpu, Finland, Flin Flon, Manitoba, and Milk River, Alberta! Thank you Doug, for providing me with enough guidance when I needed it, but keeping enough space to allow me to reach my own discoveries. And thanks for sending me to Beijing for my first technical presentation, even though, my audience DID speak AND understand English! Thanks to Mauricio Sacchi for all the relaxed and sometimes off-topic discussions, as well as the occasional instructional chat. Thanks to Curtis Lettley for teaching me about the McMurray formation; your competence was enlightening and corrected some of my over simplistic descriptions of McMurray depositional environments.

The earlier field work for this project was funded by earlier Alberta Oils Sands Technology and Research Authority (AOSTRA) grants to Doug Schmitt. Financial support for my stipends came from Doug Schmitt's NSERC Discovery grant and from teaching assistantship from the Department of Physics at the University of Alberta. Scholarship awards from CSEG, CWLS, and the Government of Alberta during my tenure were also greatly appreciated.

Sam Kaplan and Ted Bertrand are two friends that I met during my program who I am very grateful for. I have learned a lot from each of them, and I appreciate the coffee, conversations, and contemplations. They are two grad students for whom I have great respect and appreciate the ways in which they have helped me. I would also like to

extend gratitude to the other geophysics grad students in the department for their technical help and fresh ideas. I owe thanks to the geology grad students with whom I competed in the AAPG IBA competition; it was a fantastic experience to work with such bright and keen individuals.

Now, on a more personal note, I am very much in debt to my family for all their love and support. No job is ever done in isolation, and those who are closest to me are as much to blame for this document as I! To Tara, my partner and best friend; your enthusiasm and support is uplifting. Thank you for showing genuine interest for all the little details along the way, and for keeping me focused (well, trying to). Dad, I appreciate your no-nonsense approach to giving me advice and I will forever strive to keep up with your work ethic. Thanks for lending a helping hand when I needed it. Mom, your grace, compassion, and strength cannot be fully described and it propels me to not only to live happily, but to be happiness.

As any author wishes his work to reach the largest possible readership, finally, I thank you, the reader, for taking on the pages that lie ahead.

Contents

List of tables

List of figures

1.10. Steam pressure-enthalpy schematic. While the enthalpy of steam over 1000-3500 kPa is relatively constant, the proportion of latent heat (gray bars) is higher at lower pressures. Since latent heat is the primary form of heat transfer to the reservoir, one can see the appeal of injecting steam at low pressures. Image modified from Collins, 2007.

1.11. Steam assisted gravity drainage concept, after Chow and Butler, 1996. a) Rising chamber, b) spreading chamber.

1.12. Shaft and Tunnel Access Concept (SATAC), modified from Collins (1994).

1.13. Plan view of the UTF Phase B site. 3 horizontal injector / producer well pairs (B1, B2, and B3) extend for approximately 600 m through the base of the reservoir. The 12 acre pattern is highly instrumented with monitoring equipment and geotechnical devices from 29 vertical observation wells as shown (Collins, 1994).

2.1 SEM image of, A) un-cleaned oil sands material, and B) oil sands material with organic components removed (cleaned). The reflective and resinous material in cracks and pores of A is bitumen, and trace amounts of clay can be seen in both A and B.

2.2. Map of oil sands deposits in Western Canada. The Athabasca Oil Sands is found predominantly in the McMurrary Formation which is shallowest in the northern part of the deposit (where it is mine-able from surface) to over 600 m depth in the south near Cold Lake. The white circles denote the location of the UTF facility where the oil sands lie about 150 m below the surface. Image modified from http://en.wikipedia.org/wiki/Image:Athabasca_Oil_ Sands_map.png..

2.3. Stratigraphic chart showing the geologic setting of the Athabasca oil sands (modified from Wightman, 1982). .

2.4. Depositional model of the McMurray formation. Much of the McMurray formation was deposited in upper estuarine channel sand laterally accreting point bars. The distribution of reservoir facies (1-3) and non-reservoir facies (4-5) are indicated in yellow and grey respectively.

2.5. Core photographs of the 5 major facies within the McMurray formation characteristic of a meandering river system with laterally accreting point bars: 1) oil sand (reservoir facies), 2) oil sand with intermittent inclined mud beds, 3) oil sand with mud clast breccia, 4) muddy dominated inclined heterolithic stratification, 5) mud plug.

2.6. Schematic of a point bar lateral accretionary complex morphology. The facies shown in figure 2.5 are shown in numbered here (1-5) in their likely position within this system.

2.7. Wireline logs for AB/16-05-093-12W4 (well 1).

2.8. Scatter-plot of *Vp* vs. *Vs* values for AB/16-05-093-12W4 (top row), and AA/09-10-093-12W4 (bottom row). The color-scales display values of gamma ray, depth and resistivity at each point sampled going left to right across the columns.

2.9. Facies distribution in V_P versus V_S cross-plot space.

2.10. Cross-plot relationships for a number of different elastic parameters for well 1. Each sample is colored according to its Gamma-ray value, low values are yellow, high values are green.

2.11. Cross-plot relationships for a number of different elastic parameters for well 2. Each sample is colored according to its Gamma-ray value, low values are yellow, high values are green.

2.12. Facies distribution of McMurray facies in $\lambda\rho$ vs. $\mu\rho$ cross-plot space. This cross-plot combination allows easy correlation with seismic data that has undergone inversion and shows excellent discrimination between the different lithologies.

2.13. Elastic impedance (A) and Shear impedance (B) as a function of P-wave incidence angle.

2.14. Computation of absolute *NEI* and *NPSEI* values for all possible incidence angles *(0-90°)*. This is a typical well log through the McMurray formation. Log tracks of A) V_p, V_s, and density (the input parameters to equations 2.2 and 2.4), B) normalized elastic impedance as a function of angle, and C) normalized P-to S-converted wave elastic impedance as a function of angle, and D) Gamma-ray and resistivity logs (the facies indicators).

2.15. Computation of scaled *NEI* and *NPSEI* values for all possible incidence angles *(0-90°)*. Typical well log through the McMurray formation. Log tracks of A) V_p, V_s, and density (the input parameters to equations 2.2 and 2.4), B) normalized elastic impedance (*NEI(θ°)*) divided by vertical incidence elastic impedance (*NEI(0°)*) value. C) P-to S-converted wave elastic impedance (*NPSEI(θ°)*) divided by vertical incidence elastic impedance (note $EI(0^o) = PSEI(0^o) = AI = \rho V_p$) , and D) Gamma-ray and resistivity logs (the facies indicators).

3.1. Schematic of the SAGD method.

3.2. Processed seismic section showing amplitude variation along 3 well pairs actively steaming in an Athabasca reservoir. Well pairs are coming in and out of the page (from Schmitt, 1999).

3.3. Contour plots of the bulk modulus (top) and density (bottom) of water and steam as a function of pressure and temperature (figure modified from Theune, 2004).

3.4. Typical well log from the shallow part of the Athabasca reservoir.

3.5. SEM image of A) oil sands material (un-cleaned), and B) oil sands material with organic components removed (cleaned).

3.6. Temperature dependence of Alberta heavy oils and bitumens versus temperature. Ranges of viscosity values fall within the gray zone. The lower bound and upper bounds are typical of Lloydminster heavy oils and Athabasca bitumen, respectively. For comparison, the viscosities of a number of food products shown by the gray filled circles, most are given at 20ºC. Figure modified from D. Schmitt, personal documentation, 2005.

3.7. a) Variation of the P-velocity with effective pressure. b) Velocity-Pressure gradients against effective pressure. The gray dotted line shows the pre-steam effective pressure for the Athabasca reservoir.

3.8. Colored contoured surface of K_d expressed as a function of K_{eff} and K_f as described by equation 3.5. The sonic-log-derived upper bound 'SUB', and lower bound 'SLB', indicate the range of data points determined from borehole dipole sonic log measurements. The bounds come from the high and low V_P values b) Scatter plot of K_{eff} vs. μ_{eff} for oil sands, and c) histogram depicting the spread of K_{eff} values found within the borehole. The Hertz-Mindlin lower bound (HMLB) was determined from equations 9 and 11. The curve $K_d=0$ corresponds to Wood's formula; a fluid saturated suspension of grain particles.

3.9. Dry frame bulk modulus as a function of effective pressure for 9 values of the porosity representing unconsolidated sediments. The curves were calculated based on the heuristically modified Hashin-Strikman lower bound of the Hertz-Mindlin contact model for uncemented mineral grains ((Dvorkin and Nur, 1996) as shown in equations 3.9-12. The dots indicate the effective pressure conditions that we explicitly evaluate for this reservoir.

3.10. Temperature dependence of bituminous oil and oil sands.

3.11. Schematic of a ternary diagram which can be used to plot all possible combinations of a 3-component fluid mixture. The black diamond corresponds to a saturation of 30% water, 20% steam, 50% oil.

3.12. Ternary diagrams for the oil-water-steam reservoir system with K_d=3.40 GPa (first row), K_d=3.50 GPa (second row), K_d=3.60 GPa (third row), for three different reservoir depletion scenarios (columns). In these plots, we assume that there is no pore pressure induced variation on K_d; velocity variations are a result of fluid substitution only. The fluid saturation within typical SAGD chamber (62% oil, 15% water, 23% steam) is indicated by the white circles.

3.13. Ternary diagrams for the oil-water-steam reservoir system with K_d=3.40 GPa (first row), K_d=3.50 GPa (second row), K_d=3.60 GPa (third row), for three different reservoir depletion scenarios (columns). In the calculations displayed here, variations in K_d are estimated based on increased fluid pressure, via the relationship shown in figure 3.7. The velocity variations are a result of both fluid substitution and pore pressure induced rock frame 'softening'. The fluid saturation within typical SAGD chamber (62% oil, 15% water, 23% steam) is indicated by the white circles. Note how increasing fluid injection temperatures and pressures (moving from column 1 to column 3) has a large effect on the frame and velocities drop dramatically.

3.14. Contour plot of V_{Peff} for a range of pressures affecting the fluids (horizontal axis) and the rock frame (vertical axis) within a model steam zone. Contour labels have units of velocity (m/s). V_{Peff} is calculated with the saturation held constant (at 62% oil, 15% water, and 23% steam invoked by the SAGD process). The gray circles indicate the velocity path a material would experience if its frame were not affected by pore pressure, and the gray dots indicate the velocity path a material would experience if the rock frame does change due in response to changes in pore pressure (i.e. changes in the effective confining stress). The black and gray dots indicate the pore-pressure, temperature, and frame values explicitly illustrated in ternary diagrams in figures 11 and 12.

3.15. A) Hypothetical temperature profile of a typical steam chamber in Athabasca reservoir B) Computed P-wave velocity anomaly result from rock physics and fluid substitution analysis. C) Un-migrated synthetic seismic profile generated using an acoustic finite difference algorithm. The steam anomaly in B) is superimposed on the background reflectivity determined by closely spaced well logs at the UTF. The offset range used in this stacked section is 48 -142m.

4.1. Well log cross-section running south to north across the 3-well pairs at UTF. Gamma-ray is green, resistivity is pink, and P-sonic is blue. The observations wells are spaced approximately 40 m apart and the greater stratigraphy seen from the log curve signatures are incredibly consistent across the short distance shown here. The approximate positions of the horizontal well pairs are indicated by the black circles (coming into and out of the page).

4.2. A) Hypothetical temperature profile of a typical steam chamber in Athabasca reservoir B) Computed P-wave velocity anomaly result from rock physics and fluid substitution analysis from Chapter 3. The maximum width of the steam zone is 48 m wide.

4.3. Cross-sectional velocity models used in generating synthetic seismic data. A 'reference' or 'baseline' data set was computed without the steam zone anomaly, using the background velocities only. These two velocity models represent a snapshot in time after steam chambers have developed.

4.4. Comparison between shot gathers generated in the field (A) and numerically (B). The finite difference approach fails at producing the near surface refractions (seen at near offsets in the left panel at ~80 ms), the ground roll and airwave (seen at near offsets on the left panel at ~300 ms), but generally does a acceptable job at estimating acceptable reflections within the region of interest (~125 - 250 ms).

4.5. Baseline shot gather (right panel) and monitor shot gather (left panel) generated from finite difference algorithm. For numerical stability reasons, a broadband Ricker wavelet, comprised of frequencies from 10-200 Hz was used as the seismic source. The monitor survey in this figure is shot over the very small velocity anomaly shown in figure 4.6. Blues are troughs, reds are peaks.

4.6. Taking the difference between time-lapse surveys may provide unphysical reflection signals.

4.7. Snapshots of the numerically generated acoustic wavefield taken after the shots have been fired. The bright arcuate transmitted pulse has propagated down into the Paleozoic carbonates at the time the snapshot was taken. In A, the wavefield propagates through the velocity model (C) without a steam anomaly inserted. In B, the wavefield is that through the velocity model (C) with a small elliptical velocity anomaly inserted as shown. The ellipse is 15 m wide and 20 m high, and the velocities within the ellipse are 90% of the surrounding background. This is 10% decrease in velocity indicative of a heated zone. The red values on the wavefield snapshots are compressions (peaks) and the blue values are dilatations (troughs). In the velocity model (C), the 'cold' blue colors are low velocities, and the 'hot' yellow and red colors are fast velocities.

4.8. Shot gather image and semblance profile showing reflection maxima.

4.9. Comparison between an 'ideal' seismic profile (left), and a more realistic seismic profile over one steam zone (right).

4.10. Post-stack synthetic seismic section showing steam chamber anomaly with velocities decreased by A) 10% relative to the background velocity model, and B) 35% relative to the background velocity model. The offset range used in these stacked sections is 48 -142m. No migration or deconvolution has been applied in the processing of these data. Note, these data have been filtered after stacking with a bandpass filter with corner frequencies 0-5-55-70. Blues are positive amplitudes and red are negative amplitudes. Furthermore, a t^{α}-style gain has been applied ($\alpha = 1.5$) in order to highlight the diffractions at later travel times.

4.11. Annotation of steam zone anomaly on seismic section. The true vertical thickness of the steam zone in B) is the same as the true vertical thickness as the steam zone in A). The apparent elongation of the steam zone is due to the increase travel time delay through the zone. The steam zone have the same shape, however the width of the steam zone in B (48 m) is three times wider than the steam zone in A (16 m).

4.12. The trivial summation of one steam zone shifted three times does not take into account the 2-D superimposing of diffracted energy and generated intra-steam zone reverberations. The three-steam zone model in B) was created by shifting the center steam zone seismic data (at 120 m) to make three independent steam zones models (with centers at positions 50, 120, and 190 m) and subsequently summed. Such interference can make time-lapse imaging problematic, but this model is too simplistic. Although the strength of the anomalies in B is significantly diminished relative to the anomaly from a single steam zone, the true physics of three steam zones is not accurately determined.

4.13. Annotation of key horizons and features within synthetic steam zone model. In A, a maximum travel time delay in A of 55 ms, and the local increase in amplitudes are clear indicators of the steam zone. The top of the steam zone is marked by a clear trough event, and the bottom of the steam zone is delayed and shows tuning with the Paleozoic Unconformity. In B, the maximum travel time delay along the Paleozoic Unconformity horizon is 4ms. Caution must be taken when picking Paleozoic Unconformity event as a travel time reference marker. The true position of the 3 steam zones (drawn in travel time) is not resolved by the reflection events in B).

4.14. The seismic profile generated over one steam zone (A), cannot be used as a trivial proxy for three steam zones closely spaced (B). The complicated smearing and blurring of the waveforms caused by multiple steam zones can make time-lapse interpretation problematic.

4.15. Annotation and interpretation of key horizons and features within synthetic steam zone model. The seismic profile generated over one steam zone (A), cannot be used as a trivial proxy for three steam zones closely spaced (B). The complicated smearing and blurring of the waveforms caused by multiple steam zones can make time-lapse interpretation problematic. In this case mapping the travel-time delay on the Paleozoic Unconformity would lead to an incorrect estimate of the steam distribution, whereby the maximum pull down does not coincide with the thickest part of the steam chamber.

4.16. Comparison of real seismic data collected after 3 years of steaming at UTF versus numerical seismic data of 3 symmetric steam zones. The numerical model accurately predicts the extended travel time pull-downs in undepleted reservoir between the steam zones, and this region might be erroneously be interpreted as a depleted portion of the reservoir filled with steam.

4.17. Comparison of real seismic data collected after ~7 years of discontinuous steaming at UTF versus numerical seismic data of 3 symmetric steam zones. This 1999 data set has higher overall bandwidth and higher vertical resolution than in 1995. The numerical model accurately predicts the extended travel time pull-downs in undepleted reservoir between the steam zones, as this region might be erroneously be interpreted as a depleted portion of the reservoir filled with steam.

5.2. Midpoint coverage of seismic profiles collected over the study area at UTF.

5.3. Raw shot gather at UTF. An example of the effect first arrivals, surface waves and air waves on the seismic reflection data. Energy arriving at times of less than 120 ms is primarily refraction

energy, but some shallow reflections can be seen at short offsets. Note the lower apparent frequency and the apparent dip of the refractions. The true reflections at times between 120 and 250 ms show higher frequency and a flat structure. Data have been normalized by the mean value over each trace for display purposes in this figure.

5.4. Non-hyperbolic reflections caused by large near surface velocity variations and static shifts. NMO-correction fails to align reflection events because events do not follow smooth travel-time hyperbolae. The repeatability between these two CMP gathers (collect one month apart) is notable.

5.5. Raw shot gather example (left) is cleaned after surgical muting and removing the bad traces (right).

5.6. Example CMP gather after application of shift-stack to flatten the reflections in the area of interest.

5.7. 11 time-lapse data profiles over three well pairs at UTF. Injector / Producer well pairs are located at 50m, 120m, and 190m along the profile. The largest positive amplitudes have been colored blue and they are located at the positions of the steam zones.

5.8. 3-dimensional representation of repeated 2-D seismic (time-lapse) data collected over 3 steaming horizontal well pairs at UTF. Position and two-way-travel time are on plotted the x and y axes respectively, and the volume of data is given a 'depth' perspective by stacking the repeated sections along the z-axis (in ascending calendar date). The 'brightest' amplitudes (both positive and negative) have been rendered as semi-transparent '*iso-surfaces'*. These *iso-surfaces* are thought to be indicators of the lateral extent of the steam chambers. The reverberations are proportional to the magnitude of steam in the reservoir and coincide with the modeled reverberations in Chapter 4. The approximate location of the well pairs are indicated by the black lines, however their size and vertical separation are not to scale.

5.9. Trace by trace Hilbert Transform of data in figure 5.8. Largest values are rendered in brown. Well pairs are located at 70 m, 150 m and 220m along the position axis.

5.10. Single-fold data showing constant offset gathers (100m source-receiver separation). Gaps show bad channels where the traces have been removed, and although there is a large amount of "noise", reflections and refractions are clearly seen and methodically reproduced at different dates. The first arrival (near surface refraction) occurs at ~110 ms for all traces, and the subtle variability of the waveform character from South to North is systematic from one survey to the next.

5.11. Constant processing and amplitude normalization on the Wabiskaw gas sand for 3 data sets.

5.12. Seismic time lapse difference over one month (top), and 4 years (bottom).

5.13. Steam injection rate, oil recovery rate and steam-oil ratio for one well pair at UTF.

List of symbols and abbreviations

Vp – compressional wave velocity *[m/s]*

Vs – shear wave velocity *[m/s]*

ρ or ρ_{eff} – effective or "bulk" density *[kg/m^3]*

K_{eff} – effective bulk modulus *[GPa]*

μ_{eff} – effective shear modulus *[GPa]*

λ – "Lamé" parameter *[GPa]*

v – Poisson's ratio

V – Volume *[m^3]*

P – Pressure *[Nm^{-2}]*

EI – Elastic impedance *[units depend on incidence angle of p-wave]*

PSEI – P- to S-converted wave elastic impedance *[units depend on incidence angle of p-wave*

NEI – Normalized elastic impedance *[kgm^{-2}s^{-1}]*

NPSEI – Normalized P- to S-converted wave elastic impedance *[kgm^{-2}s^{-1}]*

Chapter 1

Introduction

"Some day, historians will mark the first two decades of this century as another break point; another dawn of a new energy era. An understanding of history, technology and economics will help us find the solutions that are needed for a better, more secure energy future. In the midst of great uncertainty, one thing is clear: Those that don't actively seek out solutions now, may have unpleasant choices forced upon them soon."

Peter Tertzakian, A Thousand Barrels a Second, 2006

1.1.1 Basics of time-lapse monitoring

What is time-lapse reservoir monitoring and why is it important?

Reflection seismology, or 'seismic' as it is sometimes more erroneously[1] but commonly referred to within the oil industry, is a method of geophysical prospecting that uses the principles of elastic wave propagation to quantitatively estimate and image properties of the Earth's subsurface. Seismic exploration is the primary method of exploring for hydrocarbon accumulations, and although the technology of exploration techniques has improved dramatically in the past 50 years, the basic principles for acquiring seismic data have essentially remained the same. In simple terms and in all settings, the general principle is to send sound energy into the Earth and record the

[1] The word 'seismic' is an adjective, not a noun.

sequence of reflected energy that returns from different layers in the subsurface. Once this energy is recorded, it can be processed to make images and extract quantitative information about the subsurface. In the past, seismic surveys have primarily been used to obtain two and three dimensional images of the structure of the earth. During the last 15 years, there has been increasing interest in using seismic to monitor temporal changes in the subsurface. Time-lapse seismology is the term used to describe the practice of collecting multiple seismic data sets over a period of time at a place where the subsurface properties are changing.

Time-lapse reservoir monitoring enables geoscientists to study the evolutionary behavior of fluid-producing reservoirs. This knowledge is enormously important and increasingly urgent for the energy industry. Worldwide, the remaining discovered oil reserves are now just about as large as those already consumed (Tertzakian, 2006). That is still a vast amount of oil, but it is being consumed rapidly, and additional conventional reserves are increasingly hard to find. It is imperative for the industry, for consumers, and the greater global community that we produce the remaining oil as reliably and efficiently as possible.

Hydrocarbon reservoirs are complex systems and challenging to understand. Optimizing any system is impossible if you do not understand how that system works. Optimization includes aspects of cost and profit, safety, environmental impact, recovery factor, and timeliness. It is still not yet known how much recovery improvement ultimately will be possible from time-lapse data, but researchers are proving it is profitable to find out. If you consider the current yield of many of the in-situ oil sands

recovery projects currently underway in Northern Alberta, it is encouraging to contemplate the economic impacts of making the production process more efficient (table 1.1.). Generally speaking, to make a steam-based in-situ recovery project more efficient, operators must increase the amount of hydrocarbons coming out of the ground per unit of

Company (and Investment)	Project	Ave. Daily Production (bbpd)	Produced per Year (bbls)
PetroCanada (investment $298 million)	MacKay River	25,000	9.13 million
Japan Canada Oil Sands (investment $300 million)	Hangingstone	5,500	2.01 million
Devon Canada Corp. ($10 million)	Devon Dover SAGD project (formerly UTF)	4,000	1.46 million
Devon Canada Corp. ($300 million)	Jackfish	30,000	10.9 million
OPTI Canada / Nexen Inc. ($450 million)	Long Lake	70,000	25.6 million
EnCana Corp. ($400 million)	Christina Lake	70,000	25.6 million
ConocoPhilips Canada ($300 million)	Surmont	25,000	9.13 million
Husky Energy (proposed $1.6 billion but not yet approved)	Sunrise Thermal	50,000	18.3 million
Imperial Oil Ltd. (proposed $5-8 billion not yet approved)	Kearl	100,000	36.5 million

Table 1.1. Selection of in-situ oil sands recovery projects underway within the Athabasca region. These projects are all set to have daily production values increase, and more projects are being planned to come online within the next few years. Data taken from oilsandsdiscovery.com/oil_sands_story/pdfs/projects.pdf data from 1995.

heat inserted. The steam-to-oil ratio (SOR) is a term engineers use to describe the amount of input required to output a unit of oil. If the SOR is too high, the costs of fresh water and methane to make steam will outweigh the profits from the produced fluids. One way to reduce the SOR is to control and navigate the steam front to where it is needed; control it using pressure gradients, or navigating it through variable length injection strings. Time-lapse information (both quantitative and qualitative), if incorporated in a timely manner, can indicate where the steam should be injected next,

and whether operational adjustments need too be made. Needless to say, the environmental and economic costs associated with wasting fresh water and fuel, spent on a mediocre reservoir depletion strategy, is irresponsible on many levels and must be the focus of future improvements.

The simple physical principles of the 4D seismic method are shown in figure 1.1. If we survey a producing oil or gas field before and during production, we can estimate changes to the reservoir. As hydrocarbons are replaced by other fluids, and as pressure and temperature change, the seismic velocity and density of the reservoir will change. From time-lapse surveys, we can measure the effects of those changes and identify where the changes are occurring in the reservoir.

Time-lapse monitoring is valuable anytime fluids are injected under pressure into the subsurface, whether for CO_2 sequestration or for enhanced oil recovery (EOR). For safety and economic reasons, it is important to track where the injected fluids are going. The pictures (courtesy of StatoilHydro) of the CO_2 sequestration at Sleipner field nicely illustrate this (figure 1.2). Here, the time-lapse images clearly show amplitudes brightening as CO_2 leaks up through the formations. The change of seismic amplitudes is significant. The increased delays caused by the associated velocity slowdown are also visible.

Imagine how important such information would be for an internal blowout in which fluids are no longer sealed within the reservoir. Such an event can be very serious and can cause great losses, damage, and contamination. In such a situation, seismic monitoring might not be high on the list of considerations, but is should be. Four-dimensional (3D-space plus time) monitoring is one ideal tool for gathering information

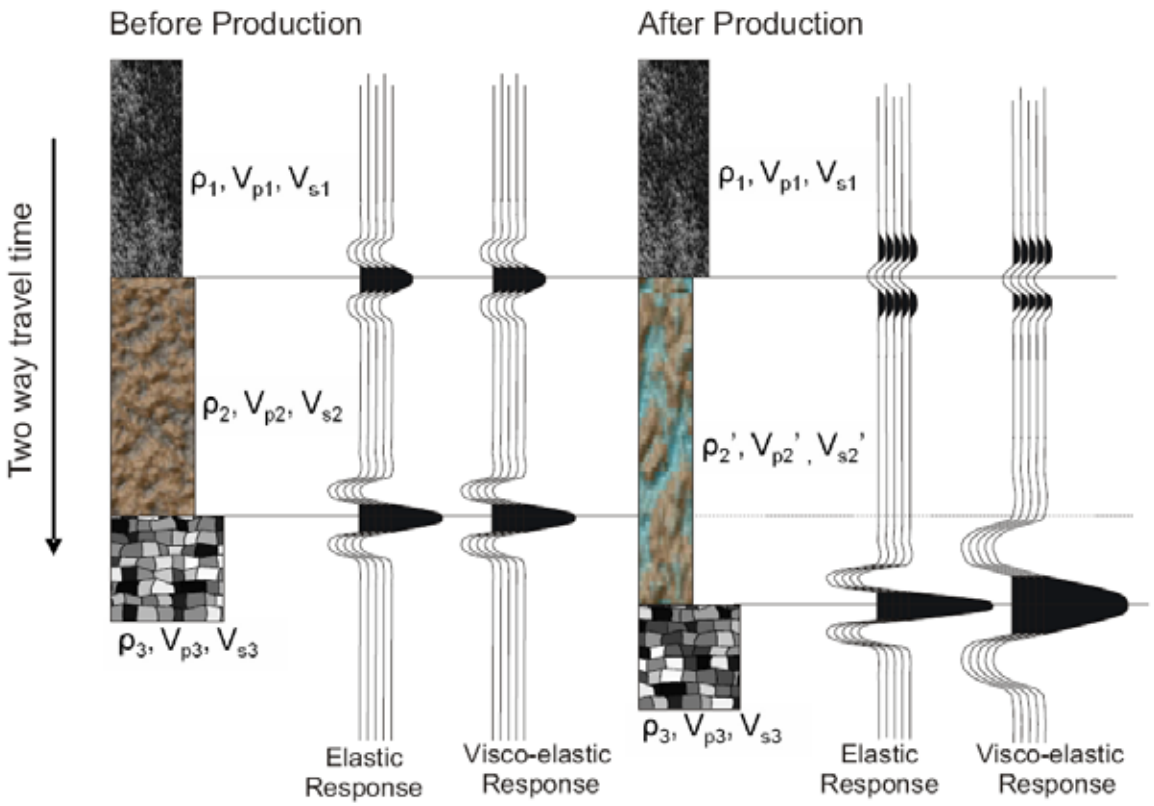

FIG. 1.1. Schematic of geophysical time-lapse monitoring. The width of the hypothetical lithology blocks shown here are proportional to the elastic impedance of each rock type. Density, P-wave velocity, and S-wave velocity change as a result of production and recovery processes. The full visco-elastic response will be sensitive to changes in the travel time, the amplitude, and the frequency characteristics of each reflection event. Elastic waves do not take into account dispersion and attenuation, so they are an approximation of real earth materials.

on where the fluids are moving, where to place relief wells, and assess when the situation is stable.

It is the multidisciplinary nature of time-lapse monitoring that makes it highly rewarding and challenging for everyone involved. Seismologists should be encouraged to go beyond the basic attributes of amplitudes and travel times and learn more about the nature of the real earth and of producing reservoirs. Reservoir modelers learn that flow properties between wells are very uncertain and cannot be interpolated reliably. Without

constraints on the measurements of flowing reservoirs, model predictions will almost

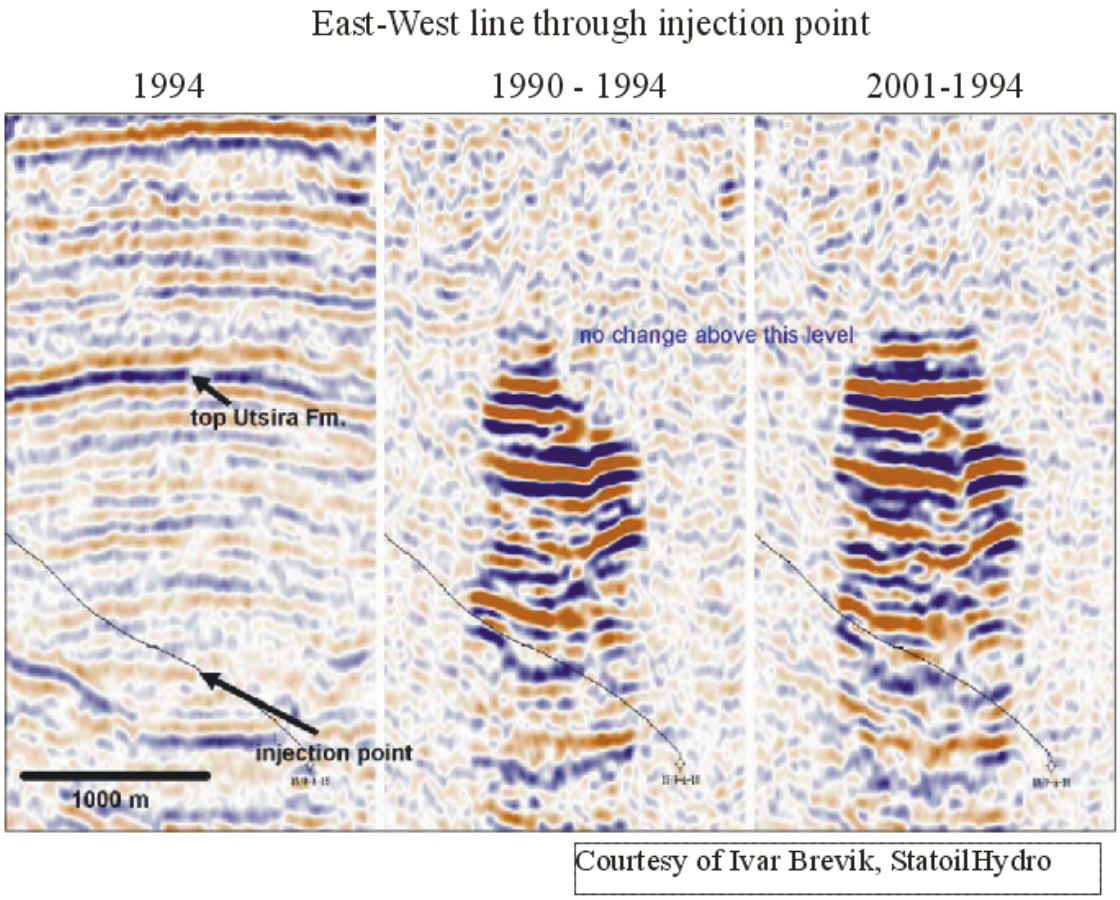

FIG 1.2. Some seismic responses to fluid are not subtle. However, correctly extracting fluid types and saturations can be difficult. Inversions for CO_2 content in this Sleipner CO_2 injection data range from 50% too low to 200% too high (M. Batzle, personal communication, 2007). The second and third panels are 'difference' images of two data sets. The laterally contiguous geologic reflections are consistent from one data set to the next and they are differenced away in order to highlight the time-lapse seismic anomaly caused by the injected fluid.

certainly be far from reality. Petrophysicists and geologists must realize that borehole and laboratory measurements on extracted core may not be representative of what is found away from the borehole.

1.1.2 Introduction to SAGD

At the moment, a steam-based enhanced oil recovery technique called steam-assisted gravity drainage (SAGD, e.g. Butler, 1996) is dominantly applied in Western Canada to produce from shallow heavy oil reservoirs. Installing and running a SAGD program is technically challenging. Many problems such as well completion failure or asymmetric or anisotropic steam propagation are possible. Such complications will cause an uneven distribution of the steam with parts of the reservoir bypassed, thus reducing the economic value of the reservoir. In order to detect such problems at an early state of the reservoir life, remote monitoring of the SAGD process has potential to be an important tool in providing almost-near-time data to aid in active engineering decision making and production planning.

Detecting small changes in the reservoir with seismic methods may be difficult. The hypothetical case shown on figure 1.1 is perhaps too optimistic. In the real earth, seismic waves are band-limited, meaning that they are insensitive to very small (high frequency) and very large (low frequency) changes in the subsurface. If a seismic wavelet has insufficient bandwidth, it will not be useful in resolving the top or base of a reservoir or it may not resolve the formation entirely (figure 1.3). Time-lapse seismology might be more difficult in such cases. Quantitative time-lapse attributes are elusive when fluids impose multiples and scattering effect not incorporated in a simple convolutional model of the earth. In order to assess the feasibility of seismic monitoring of the physical SAGD process, it is necessary to model the resolution limits with seismic data.

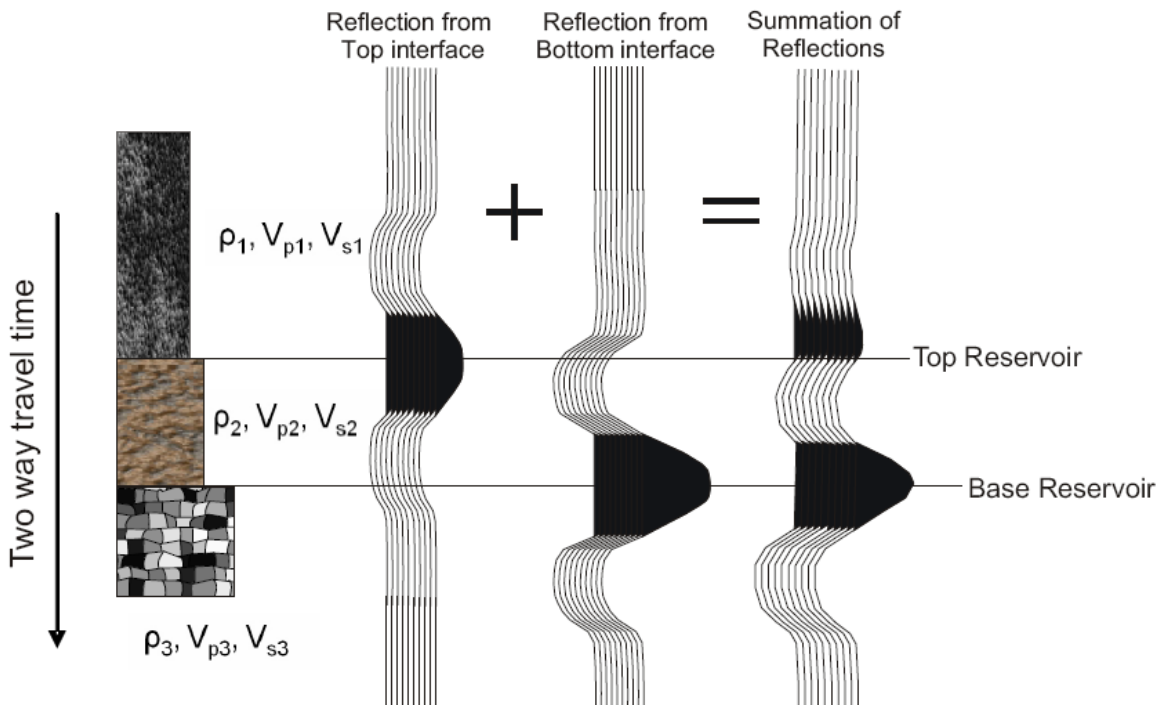

FIG. 1.3. If the reservoir is too thin or if the seismic waves lack high frequencies, imaging the top and base of an area of interest might not be straightforward. The superposition of two closely spaced reflection events sometimes results in waveform tuning or interference.

The focus of this thesis is to help address questions such as,

Do we understand the intricacies of oil sands reservoirs so that we can make realistic predictions of its' mechanical and seismic behavior? (Chapter 2),

What role can wireline measurements play in the characterization of oil sands reservoirs? (Chapter 2),

Are the changes caused by fluid substitution, pressure and temperature effects on the effective media large enough to monitor changes in the reservoir using time-lapse seismic surveys? (Chapter 3),

Can the growth of the steam chamber be accurately resolved using seismic reflection data? (Chapter 4),

What attributes or signals can be extracted from the seismic reflection data that will be useful for monitoring? (Chapter 4),

Is there an optimum survey design to monitor changes in the reservoir efficiently? (Chapter 4),

Given an assumed growth rate of the steam chamber, how frequent do seismic surveys need to be repeated to see changes between the surveys? (Chapter 4),

Do these observations and predictions correlate with field data? (Chapter 5),

Is the signal-to-noise ratio high enough, and have the acquisition parameters been sufficiently repeated to ensure reliable time-lapse differences? (Chapter 5).

As time-lapse seismology is still in its early stages, many of these questions have not yet been approached within a single project. This thesis first introduces the theoretical relationships that define seismic wave propagation, and explores the tools and technologies that can deliver (either directly or indirectly) the physical properties of the earth. Once these physical properties are determined for oil sands material, the rock physics of steam injection is studied. The results of the rock physics study provide constraints in which to perform a 2-D numerical simulation of a seismic survey over a SAGD project. These results are compared to real time-lapse data.

1.1.3 What are the time-lapse changes that can occur?

Seismic velocity and density changes in a producing reservoir depend on rock type, fluid properties, and the depletion mechanism. Time lapse-seismic responses may be caused by a number of factors. External factors such as ambient noise and seasonal variations in the weathering layer can have significant changes over time and may overwhelm any time lapse differences coming from the reservoir; this concept is summarized in figure 1.4. Geometry and equipment repeatability is a major issue with time-lapse surveys, and although it has been discussed for some time, only recently have systematic studies been employed to quantify errors (e.g. Kommedal et al., 2007, Meunier et al., 1998, Houck, 2007, Naess, 2007, and Zamorouev et al., 2006).

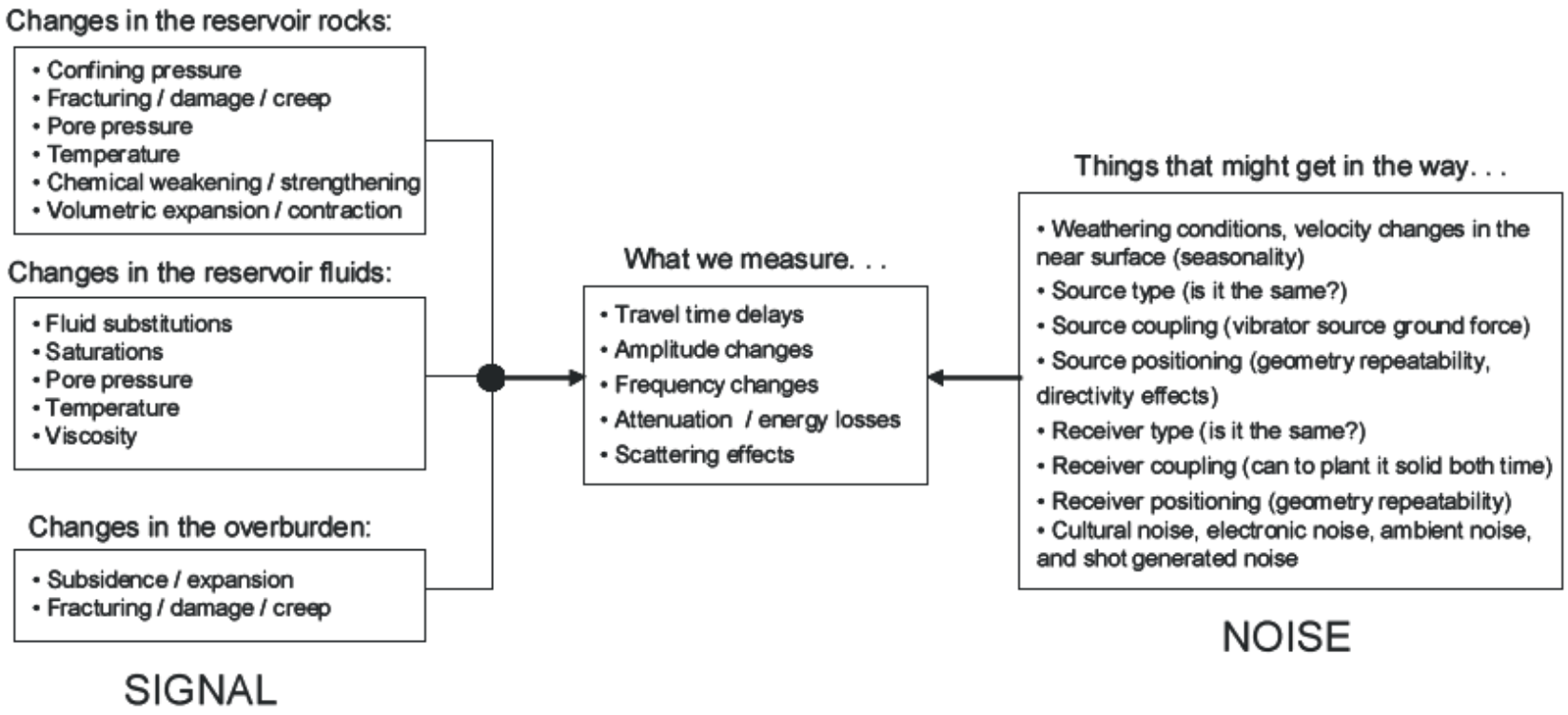

FIG 1.4. Many parameters and properties change both inside and outside of the reservoir when fluids are produced. Seismic monitoring is faced with the challenge of ensuring useful information (signal) can be distinguishable and extracted in the midst of 'noise'.

1.1.4 References

El-Emam, A. H., Hughes, J. K., and Bunaian, H. A., 1998, Repeatability of land seismic surveys: A case study from Kuwait: *68th Ann. Internat. Mtg., Soc. Expl. Geophys., Expanded Abstracts*, 5–8.

Greaves, R. J., and Fulp, T. J., 1987, Three-dimensional seismic monitoring of an enhanced oil recovery process: *Geophysics*, 52, 1175–1187.

Harris P E and Adler F 1999, Seismic resolution and uncertainty in time-lapse studies *68th Ann. Intl. Mtg., Soc. Expl. Geophys., Expanded Abstracts* pp 1671–1674.

Houck, R. T., 2007, Time-lapse seismic repeatability – How much is enough? *The Leading Edge*, 26, 828.

Kommedal, J. H., Barkyed, O. I., van Gestel, J.P., and Pettersen, R., Processing strategies for multiple repeat 4D seismic. *SEG Expanded Abstracts* **26**, 2908 (2007).

Lumley, D., 2001, Time-lapse seismic reservoir monitoring, Geophysics, 66(1), 50-53.

Meunier, J., and Huguet, F., 1998, Cere-la-Ronde: A laboratory for time-lapse seismic monitoring in the Paris Basin: *The Leading Edge*, 17, 1388, 1390, 1392–1394.

Naess, O. E., Measurements, predictions and results of geometrical repeatability in 4D acquisition, *SEG Expanded Abstracts* **26**, 2964 (2007).

Porter-Hirsche, J. L., and Hirsche, K. W., 1998, Repeatability study of land data acquisition and processing for time lapse seismic: *68th Ann. Internat. Mtg., Soc. Expl. Geophys., Expanded Abstracts*, 9–11.

Pullin, N., Matthews, L., and Hirsche, K., 1987, Techniques applied to obtain very high resolution three-dimensional seismic imaging at an Athabasca tar sands thermal pilot: *The Leading Edge*, 6(12), 10–15.

Tertzakian, P., 2006, A Thousand Barrels a Second. McGraw-Hill.

Zamorouev, A., Whitcombe, D., Dyce, M., Hodgson, 2006, A simple methodology for 4D noise reduction and repeatability improvement, *SEG Expanded Abstracts*, 25, 3155.

1.2 Rock physics basics for seismic monitoring

1.2.1 Introduction

The sensitivity of seismic waves to critical reservoir parameters such as lithology, porosity, pore pressure, pore-fluid composition, and saturation has been recognized for many years. However, the necessity to quantify seismic-to-rock-property transforms and their uncertainties has become more apparent in the last decade, with enormous improvements in digital data storage capacities, seismic acquisition technologies, and processing methods used for mapping hydrocarbons, and carrying out reservoir characterization and production monitoring. Discovering and understanding key seismic-to-reservoir relations has been the focus of rock physics research. The next section will review the basics of seismic wave propagation in terms of the intrinsic elastic constants that comprise the subsurface.

1.2.2. Review of effective elastic moduli that define seismic wave propagation

The speed at which various types of seismic waves travel in homogeneous, isotropic, elastic media are given by,

$$V_P = \sqrt{\frac{K_{eff} + (4/3)\mu_{eff}}{\rho_{eff}}} = \sqrt{\frac{\lambda + (2/3)\mu_{eff}}{\rho_{eff}}} = \sqrt{\frac{M}{\rho_{eff}}}, \qquad (1.1), (1.2), (1.3)$$

$$V_S = \sqrt{\frac{\mu_{eff}}{\rho_{eff}}}$$

where,

V_p = P-wave velocity (compressional velocity)

V_s = S-wave velocity (shear velocity),

K_{eff} = effective bulk modulus,

μ_{eff} = effective shear modulus,

λ = "Lamé" parameter ,

ρ_{eff} = effective or "bulk" density, and

M = P-wave modulus.

In terms of Poisson's ratio v (the relative extensive strain, normal to an applied uniaxial load, divided by the relative contractive strain, parallel to the direction of the applied load), one can also write,

$$\frac{V_P^{\,2}}{V_S^{\,2}} = \frac{2(1-\nu)}{(1-2\nu)}. \qquad (1.2)$$

The parameters K_{eff}, μ_{eff}, λ, ρ_{eff}, and v are called elastic constants and they describe how materials will behave under the application of stress and reversible strain. v is called the Poisson's ratio. Seismic wave characteristics such as wave speed, amplitude, and phase can be accurately predicted if the elastic properties are known. Seismic waves are dependant on elastic properties, and elastic properties can be extracted from measurements of density and P-and S-wave velocities. For example,

$$\begin{aligned} K_{eff} &= \rho_{eff}(V_P^{\,2} - (4/3)V_S^{\,2}) \\ \mu_{eff} &= \rho_{eff} V_S^{\,2} \qquad , \qquad (1.3), (1.4), (1.5) \\ \nu &= \frac{(V_P^{\,2} - 2V_S^{\,2})}{2(V_P^{\,2} - V_S^{\,2})}. \end{aligned}$$

Due to the complexity and extreme variability of earth materials, the variables on the left hand side of equations 1.3-1.5 are seldom comprised of simple expressions of, say, mineralogy alone. Homogeneous isotropic linear elastic materials have their elastic properties uniquely defined by any two elastic constants, thus, given any two, any other

elastic properties can be calculated according to the formulas shown in table 1.2. The following section gives a brief description of each elastic property and how it relates to seismic rock physics characterization.

	(λ, μ)	(E, μ)	(K, λ)	(K, μ)	(λ, ν)	(μ, ν)	(E, ν)	(K, ν)	(K, E)	(M, μ)
$K =$	$\lambda + \frac{2\mu}{3}$	$\frac{E\mu}{3(3\mu - E)}$			$\lambda\frac{1+\nu}{3\nu}$	$\frac{2\mu(1+\nu)}{3(1-2\nu)}$	$\frac{E}{3(1-2\nu)}$			$M - \frac{8\mu}{3}$
$E =$	$\mu\frac{3\lambda+2\mu}{\lambda+\mu}$		$9K\frac{K-\lambda}{3K-\lambda}$	$\frac{9K\mu}{3K+\mu}$	$\frac{\lambda(1+\nu)(1-2\nu)}{\nu}$	$2\mu(1+\nu)$		$3K(1-2\nu)$		$\mu\frac{3M-4\mu}{M-\mu}$
$\lambda =$		$\mu\frac{E-2\mu}{3\mu-E}$		$K - \frac{2\mu}{3}$		$\frac{2\mu\nu}{1-2\nu}$	$\frac{E\nu}{(1+\nu)(1-2\nu)}$	$\frac{3K\nu}{1+\nu}$	$\frac{3K(3K-E)}{9K-E}$	$M - 2\mu$
$\mu =$			$3\frac{K-\lambda}{2}$		$\lambda\frac{1-2\nu}{2\nu}$		$\frac{E}{2+2\nu}$	$3K\frac{1-2\nu}{2+2\nu}$	$\frac{3KE}{9K-E}$	
$\nu =$	$\frac{\lambda}{2(\lambda+\mu)}$	$\frac{E}{2\mu} - 1$	$\frac{\lambda}{3K-\lambda}$	$\frac{3K-2\mu}{2(3K+\mu)}$					$\frac{3K-E}{6K}$	$\frac{M-2\mu}{2M-3\mu}$
$M =$	$\lambda + 2\mu$	$\mu\frac{4\mu-E}{3\mu-E}$	$3K - 2\lambda$	$K + \frac{4\mu}{3}$	$\lambda\frac{1-\nu}{\nu}$	$\mu\frac{2-2\nu}{1-2\nu}$	$E\frac{1-\nu}{(1+\nu)(1-2\nu)}$	$3K\frac{1-\nu}{1+\nu}$	$3K\frac{3K+E}{9K-E}$	

Table 1.2. Conversion formulas between elastic parameters. E is Young's modulus, and M is the P-wave modulus. Table modified from: http://en.wikipedia.org/wiki/Bulk_modulus.

Effective bulk modulus, K_{eff}, and Gassmann's equation

The bulk modulus of a material is a measure of the material's resistance to uniform (hydrostatic) compression. It is defined as the pressure needed to effect a given change in volume; i.e.

$$K_{eff} = -\frac{\partial P}{(\partial V / V)} = -V\frac{\partial P}{\partial V} \ , \tag{1.6}$$

where V is the volume of the material and P is pressure.

If a rock matrix behaves elastically, and the fluid inside the rock is viscous, then it can be studied using poroelasticity theory, first developed by Gassman (1951) and then later by Biot (1956). Poroelasticity is thus often referred to as Biot-Gassmann theory or casually as Gassman's theory, and the equations are derived from the equations of linear elasticity, the Navier-Stokes equation, and Darcy's law for fluid flow through a porous medium (e.g Biot, 1956, 1957, Berryman, 1999, Brown and Korringa, 1975, Carcione et al., 2006).

A key finding of Biot-Gassmann theory of elasticity was the development of the fluid substitution problem. One of the most important problems in rock physics analysis and seismology is the prediction of elastic properties and subsequently, the seismic velocities in a rock saturated with one fluid from the same rock saturated with a different fluid. This is the fluid substitution problem. Generally when a rock is loaded with an increment of compression, such as the disturbance of a passing seismic wave, an increment in pore pressure change is induced, which acts against the compression, therefore stiffening the rock. The low frequency Gassmann (1951)-Biot (1956) theory predicts the resulting increase in effective bulk modulus of a poro-elastic material due to the presence of a saturating fluid and in the zero frequency limit the 'effective' bulk modulus of the saturated rock will be

$$K_{eff} = K_d + \frac{\left(1 - K_d / K_s\right)^2}{\dfrac{1 - K_d / K_s - \phi}{K_s} + \dfrac{\phi}{K_f}}. \tag{1.7}$$

This well known equation is commonly referred to as Gassman's equation, where K_d is the *dry frame* or *drained* modulus of the material, K_s is the bulk modulus of the *solid* minerals making up the matrix, K_f is the bulk modulus of the pore *fluid*, and φ is the porosity.

Gassmann's equation assumes a homogeneous mineral modulus and a homogeneous distribution of pore space but is free from assumptions about pore geometry. Most importantly, it is valid only at 'static' conditions and hence sufficiently low frequencies. Deformations induced on the material must occur on a time scale such that pore pressures are allowed to equilibrate throughout the pore space. This limitation means that Gassmann's prediction may perform less well as frequencies increase toward

typical sonic logging (~10 kHz) and ultrasonic laboratory (~1 MHz) measurements. Additionally, Gassmann's equation is cast in terms of predicting saturated rock moduli from dry rock moduli, but the most common problem in the earth is to predict effective changes from one fluid to another.

The simplest way to estimate the fluid bulk modulus is to assume a homogenous distribution and take the harmonic average of the constituents:

$$\frac{1}{\mathrm{K_f}(P,T)} = \sum_i \frac{\mathrm{S_i}}{\mathrm{K_i}(P,T)}, \tag{1.8}$$

where S_i is the fraction of i-th fluid compared to the total volume of fluid, and K_i is the pressure and temperature dependant fluid bulk modulus. A large amount of literature discusses the effects of mixed fluid and fluid distributions in porous rocks (e.g. Endres and Knight, 1989, Patterson, 1984). Where there is heterogeneous rocks and fluid distributions, there will be local differences in compression, fluid pressure responses, and resulting fluid motion. This induced motion and associated viscous friction represent energy lost from the seismic wave, and will be observed as scale- or frequency-dependant absorption and dispersion, as described by Biot (1956).

Patchy-saturation responses are often invoked in fluid substitution problems to give a larger calculated change in effective moduli than compared with the Gassmann prediction. That may make time-lapse monitoring seem better than it is and mask the need for increased sensitivity. The correct estimation of the effective elastic constants will never be available from a simple plot of impedance versus fluid saturation. The correct response of the fluids alone (never mind the complexities of the rocks that house them), will be comprised of initial and final saturation distributions, which will never be known entirely. Describing the intricate permeability tortuosities or complex patchy fluid

distributions might not be all that important. At our current seismic scale of resolution, spatial and time-averaging across a quarter wavelength cycle of a seismic wave will occur (e.g. Widess, 1973). A response will be detected even if the zones that are changed are below seismic resolution.

Fluid effects

If a reservoir made up of sand and clay is flooded, the water may react with the clay and change K_d. If a hydrocarbon-saturated carbonate reservoir is flooded with untreated saline water, it will interact with the rock matrix and make it acidic. If CO_2 is injected, it will form carbonic acid that may react with the reservoir and affect the seals. If we inject steam that is hotter or water that is colder than the reservoir, there will certainly be thermal effects that will change the properties of the native fluid and possibly the rock frame as well. These chemical and thermal effects might result in secondary changes in a drained region or may spoil attempts to delineate additional saturation changes in already flushed zones.

A note about the dry frame modulus

Of the variables that comprise Gassmann's equation, the drained bulk modulus K_d, is the most poorly understood and most difficult to measure. It is a measure of the frame properties of the rock, independent of a saturating fluid. The static or zero frequency *dry rock* or *dry frame* modulus refers to the incremental bulk deformation resulting from applied hydrostatic confining pressure with the pore pressure held constant. This corresponds to a case where pore fluids can flow freely in or out of the rock to maintain constant pore pressure. This is approximately the case for an air filled sample at standard temperature and pressure because the compressibility of the gas is far

higher than the compressibility of the solid or the frame; however at higher pore pressures and temperatures (as found within the earth) gas (e.g. methane) takes on a non-negligible bulk modulus and must be treated as a saturating fluid (e.g. McCain, 1990).

In the laboratory, it is unlikely that one would be able to completely remove the fluid from a rock without damaging or altering the frame. Additionally, rocks that are extremely dry and prepared in a heated vacuum are sometimes altered as a result of disruptive surface forces acting on the pore space walls or by release of water from the constituent clay minerals. A very dry rock that has been subject to a small amount of moisture can be chemically weakened due to the softening of cements, to clay swelling, and to surface effects (Mavko et. al, 1998). Several authors (Cadoret, 1993, Murphy et al., 1991) have shown that classical Biot-Gassmann predictions fail when very dry rock values are used for K_d, but they can be fairly accurate if extrapolated "damp" rock modulus values are used instead (e.g. Yang and King, 1986). An rearrangement of Gassmann's equation solves for K_d:

$$K_d = \frac{1 + K_{eff}\left((\phi - 1)/K_s - \phi/K_f\right)}{\dfrac{1 - K_{eff}/K_s + \phi}{K_s} - \dfrac{\phi}{K_f}}. \tag{1.9}$$

Effective shear modulus, μ_{eff}

The shear modulus μ_{eff}, of a material is a measure the material's resistance to shearing strains. It is defined as the ratio of shear stress to shear strain for small angles:

$$\mu_{eff} = \frac{\sigma}{\tau} = \frac{F/A}{\Delta x/h}, \tag{1.10}$$

where $\sigma = F/A$ is shear stress and τ is the volume of the material and F is pressure (figure 1.5).

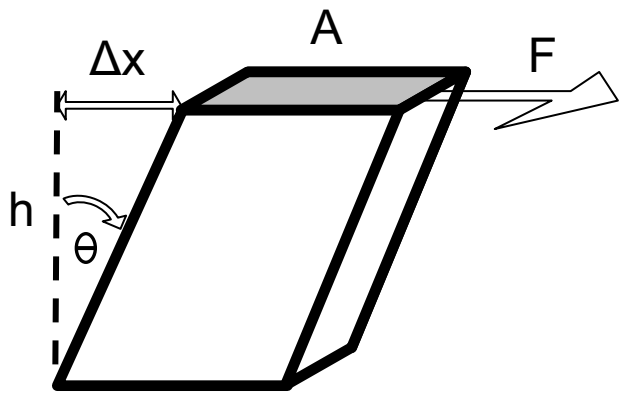

FIG. 1.5. Geometry used in the definition of the shear modulus (rigidity).

Gassmann's equation requires that the pore filling fluid has a negligible shear modulus (inviscid), i.e.:

$$\mu_{eff} = \mu_d \,. \tag{1.11}$$

For many heavy oil and bituminous oils, this is certainly not the case. In fact, Batzle (2006) shows that, at temperatures below 40ºC, Athabasca bitumen actually supports shear deformation. This type of material has been described as a semi-solid; a visco-elastic substance that behaves a fluid or a solid depending on the rate of strain deformation.

Effective density, ρ_{eff}

The effective density, ρ_{eff} of a porous material is given by:

$$\rho_{\text{eff}} = (1-\phi)\rho_s + \phi\rho_f \,, \tag{1.12}$$

where ρ_s, ρ_f, are the densities of the solid and fluid components, respectively. Under the assumption of immiscibility of the fluids, the density of a 3-phase (oil-water-steam) fluid mixture is given by:

$$\rho_f = S_O\rho_O + S_W\rho_W + S_S\rho_S \,, \tag{1.13}$$

where ρ_O, ρ_W, and ρ_S are the densities of oil, water and steam, respectively, with saturations of oil, water and steam denoted by S_O, S_w, and S_S respectively (note: $S_O + S_W + S_S = 1$).

Reflectivity, AVO, and Elastic Impedance

A seismic wave experiences partial transmittance and partial reflectance when it encounters a discontinuity. For the case of a plane wave hitting a boundary at normal incidence, the reflected and transmitted pulses have essentially the same shape and breadth but are different in amplitude. The ratio of the amplitude of the reflected wave relative to the incident wave is called the reflection coefficient, R_i;

$$R_i = \frac{\rho_{(i+1)} V_{P(i+1)} - \rho_{(i)} V_{P(i)}}{\rho_{(i+1)} V_{P(i+1)} + \rho_{(i)} V_{P(i)}}, \tag{1.14}$$

where $\rho_{(i)} V_{P(i)}$ is called the 'acoustic impedance' of the i-th layer. Thus it is said that, "the reflection of seismic waves results from variations in acoustic impedance of the wave medium in which the wave travels" (Peterson, 1955).

The logarithmic approximation

Peterson (1955) simplified eqn. 1.14 above by introducing an approximate expression for the reflection coefficient, namely;

$$R_i = \frac{A_{iR}}{A_{iI}} = \frac{\rho_{(i+1)} V_{P(i+1)} - \rho_{(i)} V_{P(i)}}{\rho_{(i+1)} V_{P(i+1)} + \rho_{(i)} V_{P(i)}}, \tag{1.15}$$

$$A_{iR} \cong \left[\frac{\Delta(\rho V_P)}{2 \rho V_P} \right] A_{iI}, \tag{1.16}$$

$$A_{iR} \cong \left[\frac{1}{2} \Delta \log(\rho V_P) \right] A_{iI}, \tag{1.17}$$

where A_{iR} is the reflected amplitude at the i-th layer and A_{iI} is the incident amplitude at the i-th layer. Therefore, eqn 1.17 can be interpreted as stating that "the amplitude of the reflected wave incremental or "step" change in acoustic impedance is proportional to the corresponding incremental change in the value of the logarithm of acoustic impedance" (Peterson, 1995). Travel-time or sonic logging within wellbores indicate that acoustic impedance varies almost continuously with depth in the earth, in direct relation to the type of rock. In practice, each small step can be regarded as giving rise to a small pulse of appropriate amplitude and polarity and the reflected energy recorded at the surface is the superposition of all of these individual events. This process of summation is used in creating "synthetic seismograms" by which the reflectivity character of the earth is modeled.

The mathematics of plane waves incident on a planar boundary become more complicated when considering non-normal angles of incidence. Notably, oblique particle displacements across a boundary results in mode conversion, resulting in the generation of reflected and transmitted shear waves (not encountered in the case above). Ostrander (1984) described how one can, in principle, use angle of incidence variations to constrain the mechanical properties of materials. Observations of the amplitude-variation-with-offset (AVO) behavior of surface seismic reflection data can lead to successful discrimination of pore fluid types and 'litho-facies' (figure 1.6). Using AVO as a successful reservoir description technology does not just depend on data quality but also on the correctness of the geologic model, and the understanding of both the reflection and propagation characteristics of seismic waves.

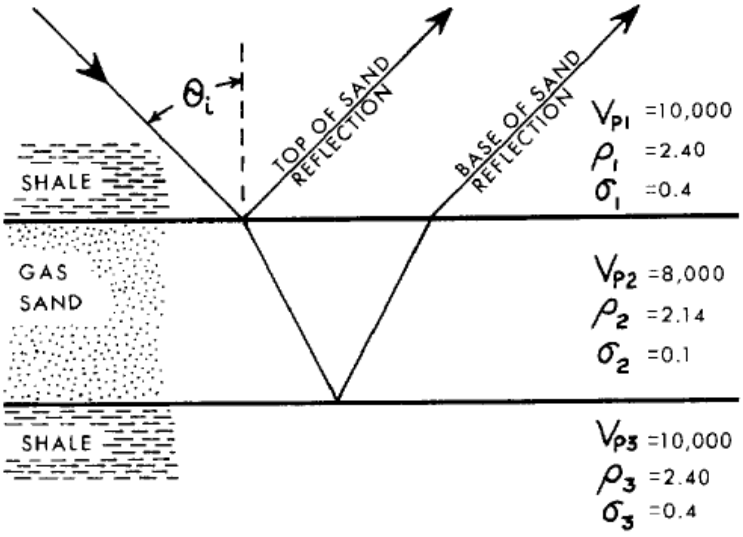

FIG. 5. Three-layer hypothetical gas sand model.

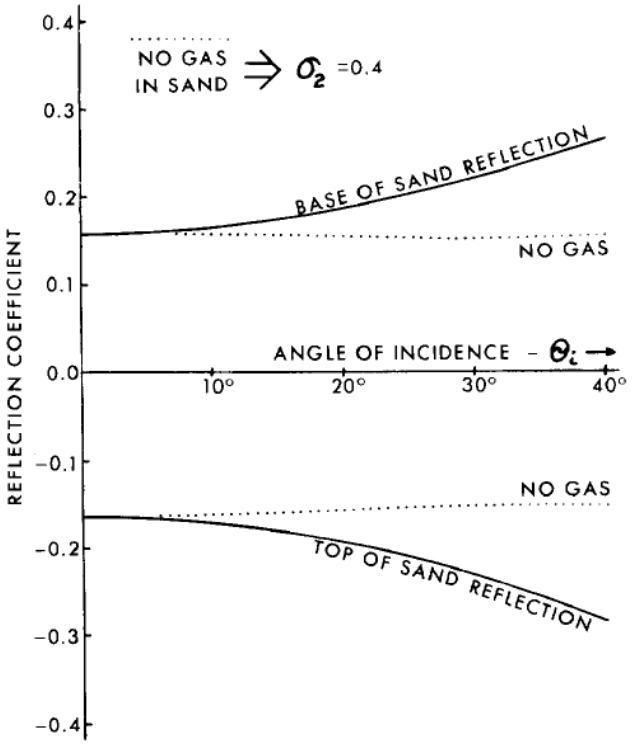

FIG. 6. Plot of *P*-wave reflection coefficients versus angle of incidence for three-layer gas sand model.

FIG. 1.6. Ostrander's (1984) original gas sand model illustrating the effect of gaseous pore fluid on seismic reflection character. The low Poisson's ratio (here denoted by the greek letter σ) of gas-filled sandstone is responsible for the reflection coefficient increasing at large angles of incidence.

An oblique incident P-wave

A planar P-wave hitting the boundary between two layers will produce both P and SV reflected and transmitted waves. This is called mode conversion (figure 1.7).

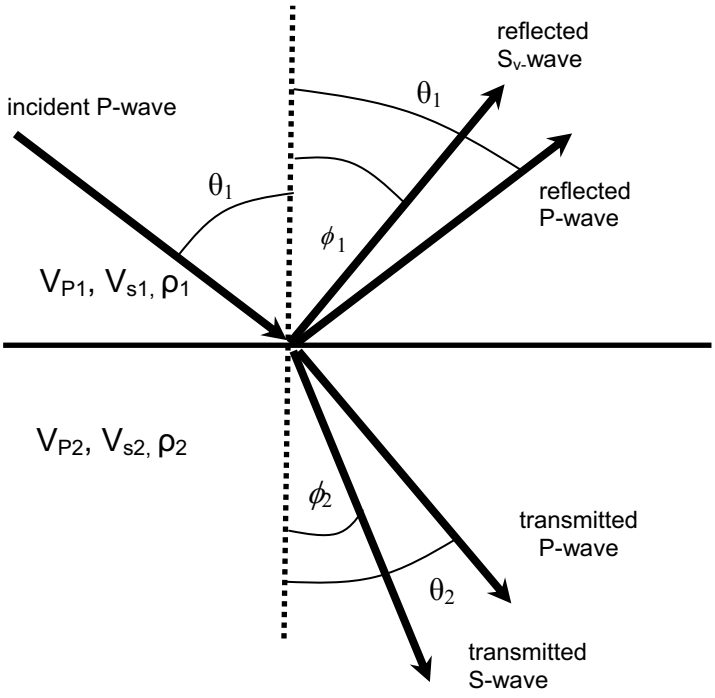

FIG. 1.7. Mode conversion of an incident P-wave hitting a horizontal interface.

The angles of the incident, reflected and transmitted rays are related by Snell's law as follows:

$$p = \frac{\sin\theta_1}{V_{P1}} = \frac{\sin\theta_2}{V_{P2}} = \frac{\sin\phi_1}{V_{s1}} = \frac{\sin\phi_2}{V_{s2}}, \tag{1.18}$$

where p is called the ray parameter.

Zoeppritz (1919) derived the particle motion amplitudes of the reflected and transmitted waves using the conservation of stress and displacement across the layer interface, which gives four equations with four unknowns:

$$\begin{bmatrix} R_p \\ R_s \\ T_p \\ T_s \end{bmatrix} = \begin{bmatrix} -\sin\theta_1 & -\cos\theta_1 & \sin\theta_2 & \cos\phi_2 \\ \cos\theta_1 & -\sin\phi_1 & \cos\theta_2 & -\sin\phi_2 \\ \sin 2\theta & \frac{V_{P1}}{V_{S1}}\cos 2\phi_1 & \frac{\rho_2 V_{S2}^2 V_{P1}}{\rho_1 V_{S1}^2 V_{P2}}\cos 2\phi_1 & \frac{\rho_2 V_{S2} V_{P1}}{\rho_1 V_{S1}^2}\cos 2\phi_2 \\ -\cos 2\phi_1 & \frac{V_{S1}}{V_{P1}}\sin 2\phi_1 & \frac{\rho_2 V_{P2}}{\rho_1 V_{P1}}\cos 2\phi_2 & \frac{\rho_2 V_{S2}}{\rho_1 V_{P1}}\sin 2\phi_2 \end{bmatrix}^{-1} \begin{bmatrix} \sin\theta_1 \\ \cos\theta_1 \\ \sin 2\theta_1 \\ \cos 2\phi_1 \end{bmatrix}. \quad (1.19)$$

R_P, R_S, T_P, and T_S, are the reflected P-, reflected S-, transmitted P-, and transmitted S-wave amplitude co-efficients, respectively. Inverting the matrix form of the Zoeppritz equations give the coefficients as a function of angle. Although the Zoeppritz equations are exact, the equations do not lead to an intuitive understanding of the AVO process. Modeling is typically done with the Zoeppritz equations but most AVO methods for analyzing real seismic data are based on linearized approximations to the Zoeppritz equations (e.g. Bortfeld, 1961, Richards and Frasier, 1976, Aki and Richards, 1980).

The commonly used Aki-Richards equation (Aki and Richards, 1980) is:

$$R_P(\theta_1) = A + B\sin^2\theta_1 + C\sin^2\theta_1\tan^2\theta_1, \quad (1.20)$$

where: $A = \frac{1}{2}\left[\frac{\Delta V_p}{\overline{V}_p} + \frac{\Delta\rho}{\overline{\rho}}\right]$ $B = \frac{1}{2}\frac{\Delta V_P}{\overline{V}_P} - 4\left[\frac{V_S}{\overline{V}_P}\right]^2\frac{\Delta V_S}{\overline{V}_S} - 2\left[\frac{V_S}{\overline{V}_P}\right]^2\frac{\Delta\rho}{\overline{\rho}}$, and $C = \frac{1}{2}\frac{\Delta V_P}{\overline{V}_P}$.

Here, the delta (e.g. ΔV_P) denotes the difference across the interface;

$$\Delta V_P = V_{P(i+1)} - V_{P(i)}, \quad (1.21)$$

and the bar (e.g. $\overline{V}_P$) denotes the average value across the i-th interface;

$$\overline{V}_P = \frac{V_{P(i+1)} + V_{P(i)}}{2}. \quad (1.22)$$

This equation is commonly referred to as the "intercept-gradient-curvature" equation, because the A-term defines the intercept, the B-term defines the gradient, and the C-term defines the curvature of the reflected p-wave amplitudes as a function of angle.

From this equation, Connolly (1999) proposed that, analogously to acoustic impedance approximation in eqn. 1.17, a term known as elastic impedance (EI) could be defined as:

$$R_P(\theta_1) \approx \frac{\Delta EI(\theta_1)}{2EI(\theta_1)} \approx \frac{1}{2}\Delta \ln(EI(\theta_1)). \tag{1.23}$$

This stems from the notion that reflectivity (as a function of angle) is approximately proportional to the incremental change in the logarithm of elastic impedance. If we let $K = [V_s/V_p]^2$ and note that $\sin^2\theta \tan^2\theta = \tan^2\theta - \sin^2\theta$, the Aki-Richards equation (eqn. 1.18) can be re-arranged to obtain:

$$\Delta \ln(EI(\theta_1)) = \frac{1}{2}\left[\frac{\Delta V_P}{V_P}(1+\tan^2\theta_1) - \frac{\Delta V_S}{V_S}8K\sin^2\theta_1 + \frac{\Delta\rho}{\rho}(1-4K\sin^2\theta_1)\right], \tag{1.24}$$

which can be written as:

$$\Delta \ln(EI(\theta_1)) = \Delta \ln\left(V_P{}^{(1+\tan^2\theta_1)}\right) - \Delta \ln\left(V_s{}^{(8K\sin^2\theta_1)}\right) + \Delta \ln\left(\rho^{(1-4K\sin^2\theta_1)}\right), \tag{1.25}$$

$$\Delta \ln(EI(\theta)) = \Delta \ln\left(V_P{}^{(1+\tan^2\theta)} - V_s{}^{(8K\sin^2\theta)} + \rho^{(1-4K\sin^2\theta)}\right). \tag{1.26}$$

After integrating and taking the exponent of both sides we get the following expression for elastic impedance:

$$EI(\theta) = V_P{}^{(1+\tan^2\theta)} V_s{}^{(-8K\sin^2\theta)} \rho^{(1-4K\sin^2\theta)}. \tag{1.27}$$

Note that if $\theta = 0^o$, EI reduces to acoustic impedance (AI), where

$$EI(0°) = \rho V_P. \tag{1.28}$$

Elastic impedance is derived from the Aki-Richards form of interface reflectivity as a function of angle. It must be reiterated that elastic impedance is not a physical property (such as, for instance, mass, density, velocity, compressibility, conductivity, color, temperature, etc.); it is only a computed attribute from measured physical properties (namely V_P, V_S, and ρ). Just as acoustic impedance describes the earth that a vertically propagating wave will see, elastic impedance describes the earth, as seen by the wave, at all incidence angles.

1.3 Description of the SAGD process

A fundamental understanding of the mechanics of Steam Assisted Gravity Drainage (SAGD) is imperative in order to study the interaction between reservoir processes and rock physical relationships.

1.3.1 The SAGD process

Prior to the invention of horizontal drilling technology, heavy-oil could be produced only by injecting steam down one vertical well, letting the reservoir heat up and drain, then pumping the recovered oil to the surface through another vertical well. This method of injecting heat into a reservoir was never successful at producing economic quantities of the extremely viscous bitumen found within the Athabasca oil sands. This was because the heated oil trickling through unconsolidated sand under the influence of gravity would fall in an ever-narrowing convergent cone (Chow and Butler, 1996). An offset vertical producing well would be out of reach from this heated zone, and sand from the depleted zone would plug up the cone used to pump the oil to the surface. The first attempt at solving this problem was to drill a horizontal producing well low in the reservoir. Instead of one vertical well that drains into a single cone, numerous drainage points along the entire length of the production well could capture the heated oil. In 1978, Roger Butler designed the world first horizontal production well paired with a vertical steam injection well. The next improvement came shortly after, which was to place a horizontal injection-producer well pair into the reservoir. Now instead of a single drainage cone, a drainage prism, or "steam chamber" could be established along the entire length of the injector-producer well pair (figure 1.8).

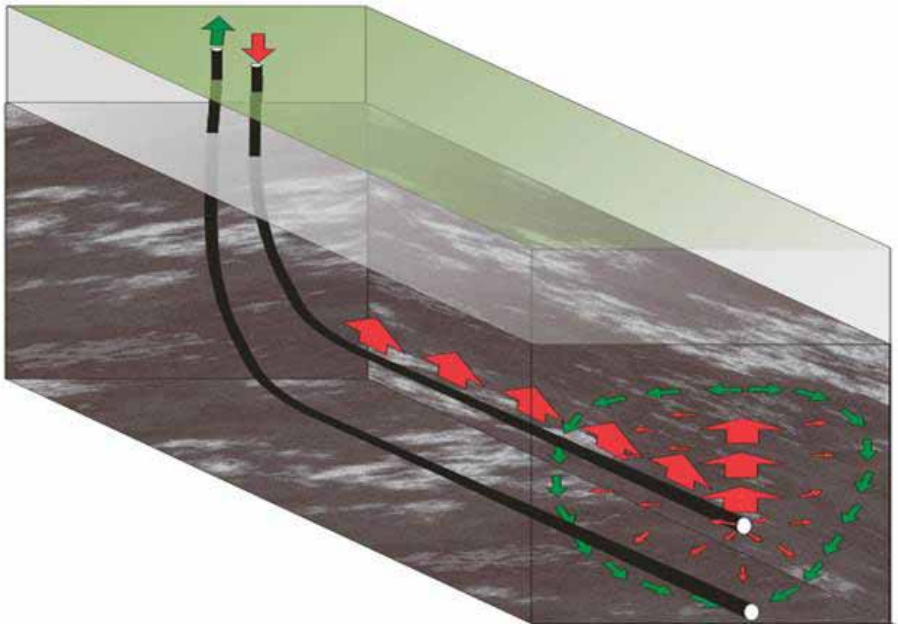

FIG. 1.8. Schematic of the SAGD method. Artwork by E. Bianco.

The steam-assisted gravity drainage process was invented by Roger Butler in the early 1980's and the main mechanism driving the production of fluids has changed very little since that time. A horizontal injector-producer pair is placed very close to the bottom of the reservoir, usually spaced 4-6 m apart. When steam is injected, reservoir temperatures and pressures are raised. These elevated temperatures and pressures reduce the bitumen's viscosity and change the rock stresses enough to cause shear failure within and beyond the growing steam chamber. Once individual sand grains are shifted and rotated, there is an increase in bulk volume caused by an increase in porosity. The associated increase in absolute permeability can be a factor of 10 (Collins, 2007). The term absolute permeability is actually a misnomer because the "absolute" permeability of an oil sand is bound to increase with shearing and disturbance of the grains. What is

important is not the original permeability that exists, but how much permeability is required, and how much pressure and temperature is required to obtain it.

The dislocation of sand grains and mechanical enhancement of permeability is desired for the SAGD process given that the rate of production is proportional to the square root of permeability (Butler, 1997). Therefore, increasing permeability by a factor of 10 should increase production rate by a factor of 3. Typically, however, the optimal injection pressure for maximizing permeability is higher than pressures being currently implemented by many operators (Collins, 2007). Low-pressure SAGD (LPSAGD) has been preferred because higher injection pressures and temperatures invoke additional costs and challenges (for example, over-pressuring of the reservoir). The supporting argument for LPSAGD is that a low pressure steam carries a larger percentage of latent heat than high pressure steam (figure 1.9 and figure 1.10); however, LPSAGD misses all the advantageous geomechanical disturbances that high pressures induce. Latent heat is the amount of energy absorbed by water undergoing the phase change from liquid to vapor. The proportion of latent heat is larger at low pressures. Since latent heat is the primary form of heat transfer to the reservoir, one can see the appeal of injecting steam at low pressures. Low pressures steam does not work to increase permeability by shearing and dislocating the sands grains.

During SAGD, most of the heat transferred to the undepleted portions of the reservoir is by the condensation of steam onto the periphery of the steam chamber. The latent heat released from the steam is transferred to the cold oil sand by conduction. The predominant flow of condensed steam (hot water) and heated bitumen is perpendicular to the direction of conductive heat flow (figure 1.11a.).

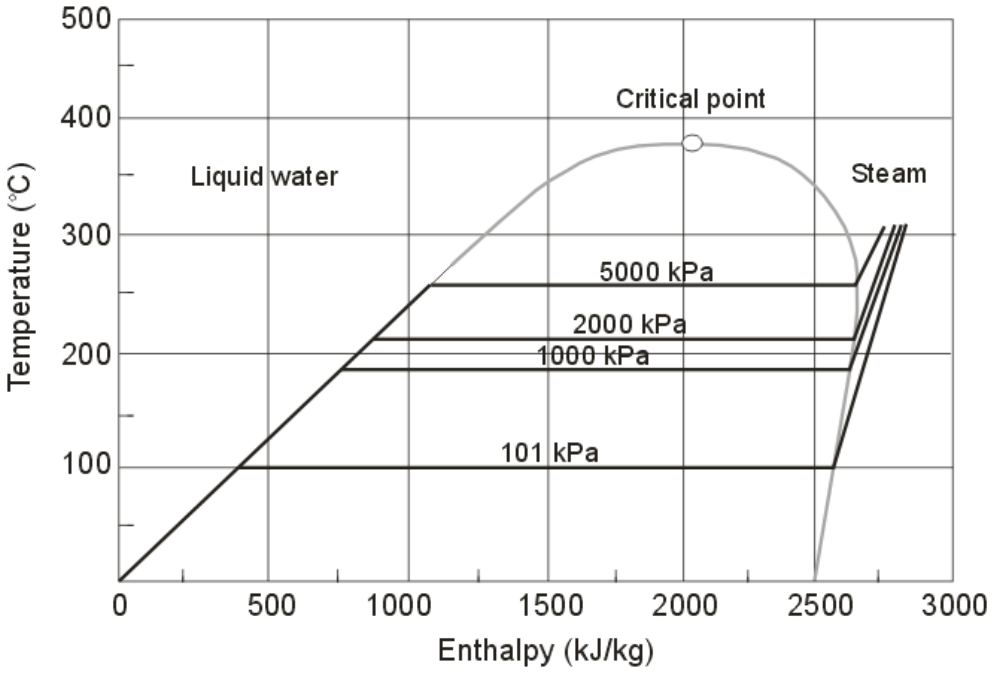

FIG. 1.9. Temperature-enthalpy schematic for steam. Image modified from Collins, 2007.

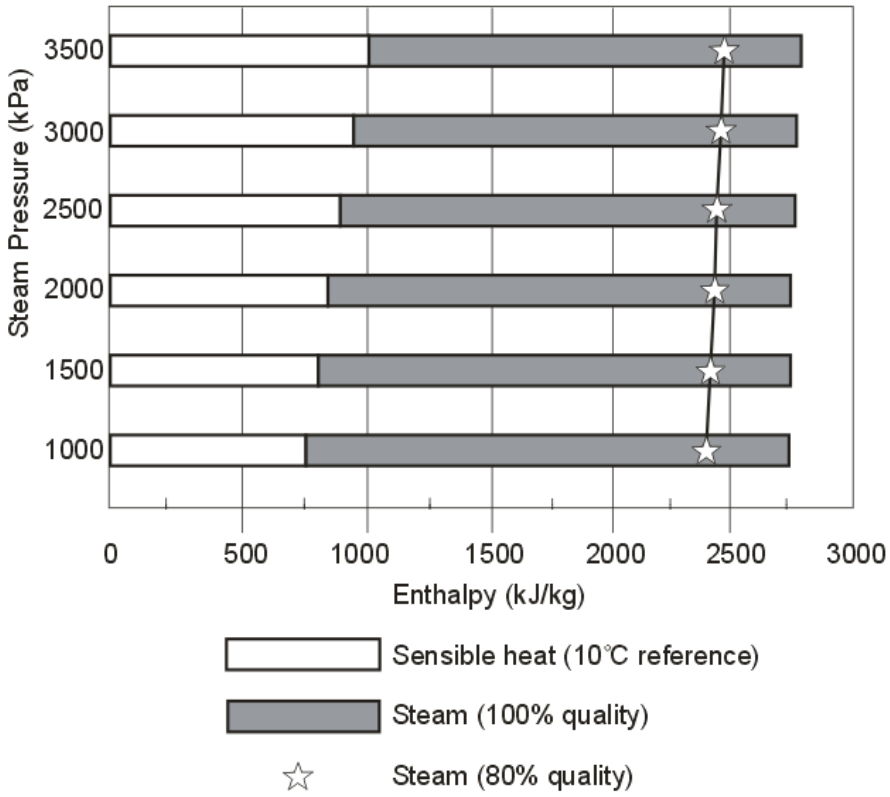

FIG. 1.10. Steam pressure-enthalpy schematic. While the enthalpy of steam over 1000-3500 kPa is relatively constant, the proportion of latent heat (gray bars) is higher at lower pressures. Since latent heat is the primary form of heat transfer to the reservoir, one can see the appeal of injecting steam at low pressures. Image modified from Collins, 2007.

It was first thought that steam grew upward initially (e.g. Shin and Polikar, 2007) to the top of the reservoir (or until it meets a permeability barrier) and then expands outward along the top of the reservoir (figure 1.11b). Ito et al. (2004) have noted that this is not the case. Instead, steam expands outward from a horizontal well pair in a "lozenge" shape. They also note that the maximum bulge in the middle of the chamber is where the largest increases in pore pressures are induced beyond the chamber and where lateral strains are the greatest.

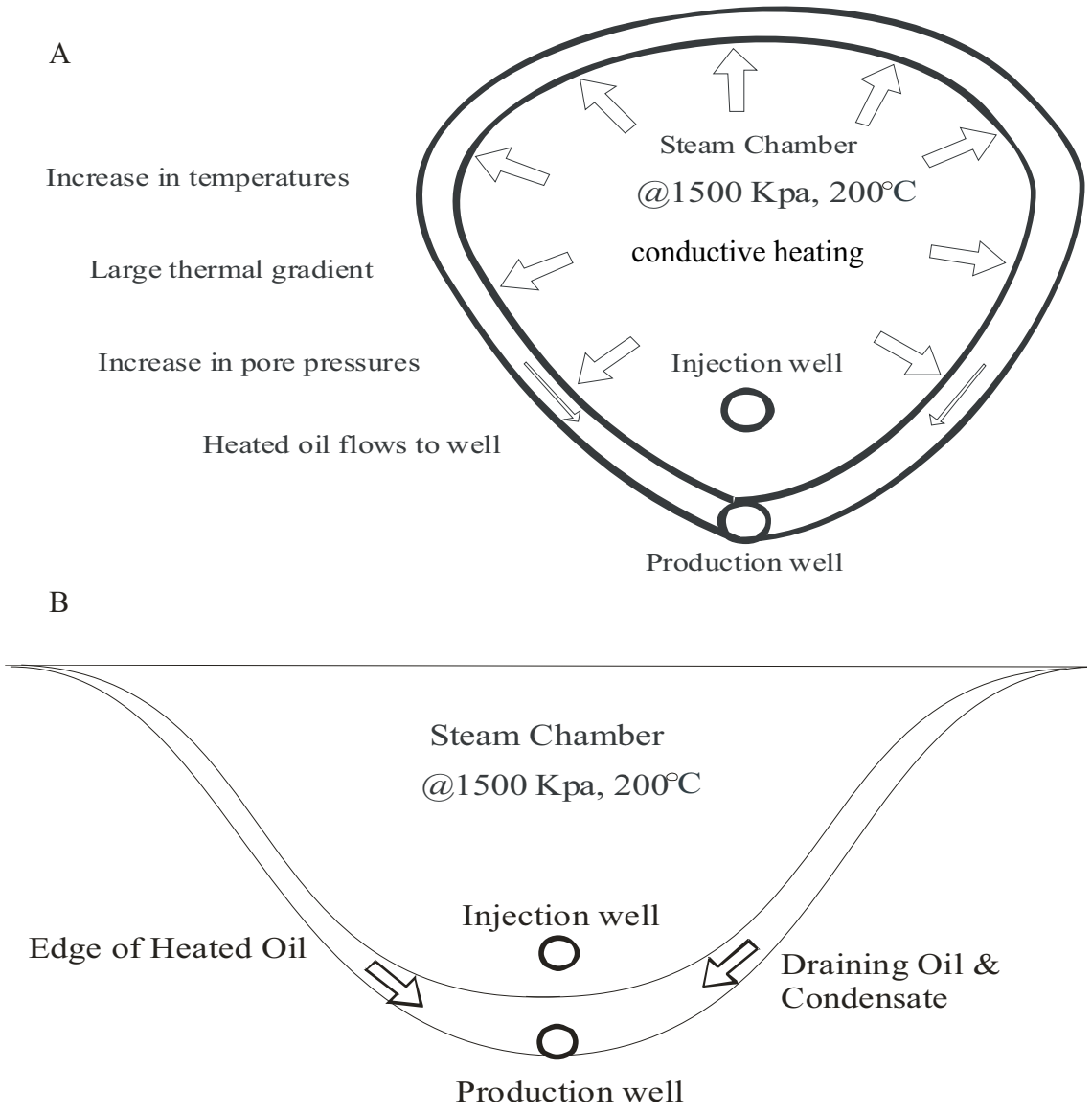

FIG. 1.11. Steam assisted gravity drainage concept, after Chow and Butler, 1996. a) Rising chamber, b) spreading chamber.

1.3.2 UTF Phase B facilities

In June 1984, the crown corporation called the Alberta Oil Sand Technology and Research Authority (AOSTRA) began construction of an underground test facility (UTF) which would permit the assessment of horizontal well in-situ thermal recovery processes

from bituminous reservoirs. In 1986, six companies: Chevron Canada Resources Limited, Texaco Canada Resources Limited, Mobil Oil Canada Limited, Petro-Canada Inc., Shell Canada Limited, Canada Petroleum Company Limited, and CANMET joined AOSTRA as participants in a PhaseA program (Chalaturnyk, 1996). The Phase A program was a pre-pilot program established for preliminary investigation of the steam assisted gravity drainage process and was approximately one-tenth of pilot scale.

Phase A started in 1987 and it sought to validate only the physical processes. Three horizontal well pairs, horizontally separated by 25 m and 60 m in length, were drilled for this phase. The test was highly instrumented and deemed a successful. The second phase, Phase B, which commenced production in 1993 aimed to prove the SAGD process on a commercial scale. For this phase, three horizontal well pairs 600 m in length, horizontally and vertically separated by 70 m and 4 m, respectively, were drilled from the underground into the base of the oil sands pay zone. These wells were successfully operated for approximately 10 years at better than predicted production outputs (Birrel, 2003).

Phase B consists of two vertical shafts 3.3 m in diameter penetrating 140 m of overburden, 20 m of oil sands and 15 m of carbonate. Within the carbonate formation, a horseshoe-shaped horizontal tunnel 5 m wide and 4 m high was excavated. From these tunnel walls, horizontal wells were drilled upward through the carbonate sequence then horizontal through the lower pay zone of the oil sands. Figure 1.12 illustrates the setup.

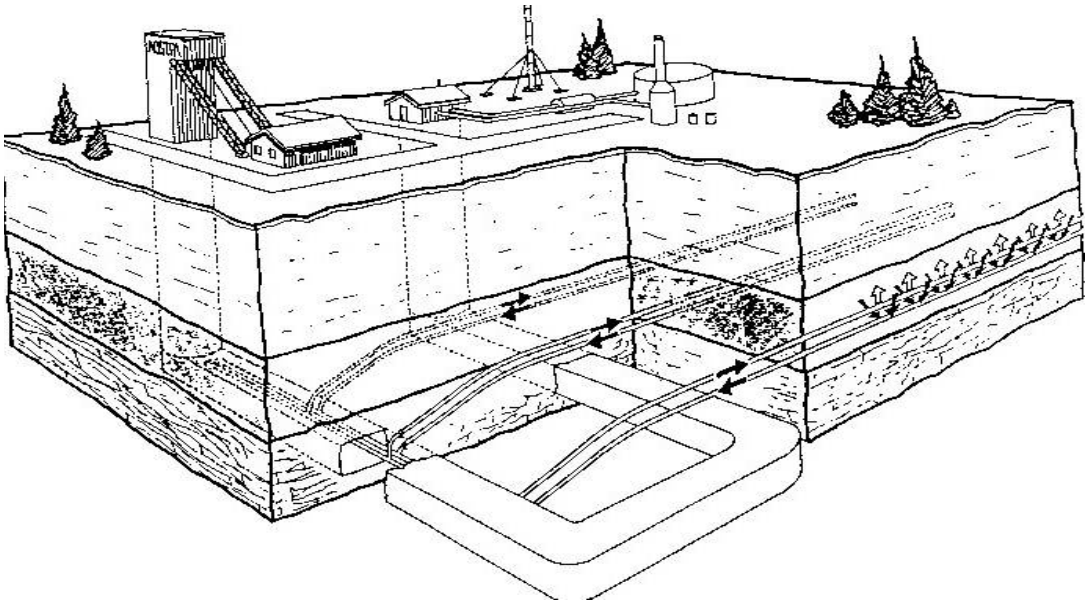

FIG. 1.12. Shaft and Tunnel Access Concept (SATAC), modified from Collins (1994).

The Phase B facility at UTF covers an area of approximately 12 acres (or 0.5 km^2) and is highly instrumented with 29 vertical temperature observation wells, 5 wells with piezometers, and a host of supplementary geotechnical equipment. Each vertical well typically has 20 thermocouples spaced throughout the reservoir succession with spacing ranging from 0.5 m to several meters. 5 wells were drilled along the length of each well pair, 6 wells were drilled between the well pairs and the remaining wells were drilled at the periphery of the pattern (figure 1.13).

Throughout normal operation, production pressures were high enough to raise fluid to the surface without the aid of artificial lift. Steam injection pressures were about 2.5 MPa whereas normal hydrostatic pressure at the bottom of the reservoir was 1.8 MPa. The produced fluids were cooled at the surface. Steam was always injected approximately 0.5 MPa below the fracture pressure of the rock mass; this ensured that

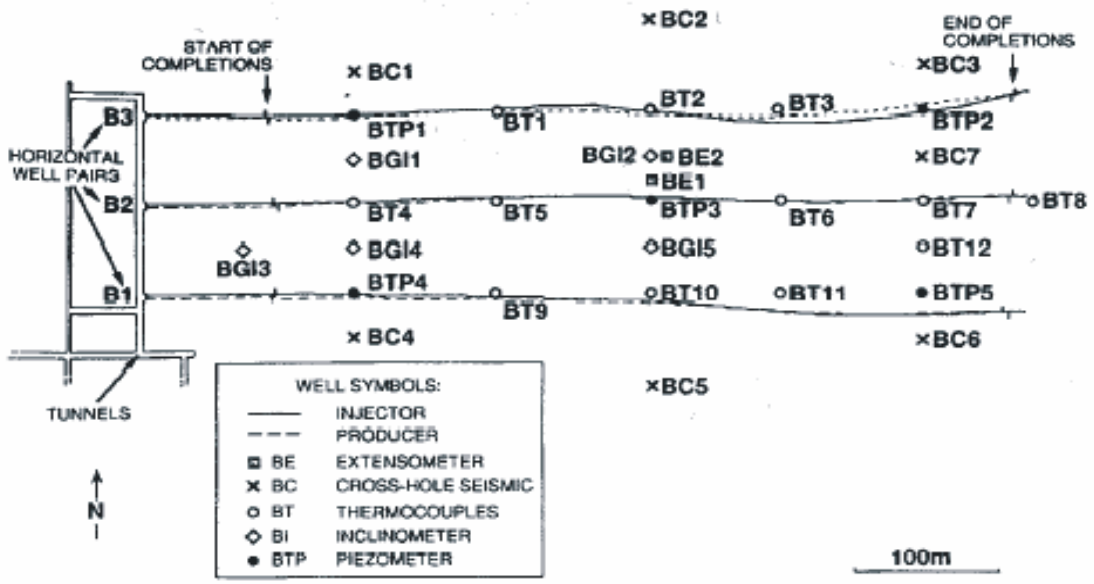

FIG 1.13. Plan view of the UTF Phase B site. 3 horizontal injector / producer well pairs (B1, B2, and B3) extend for approximately 600 m through the base of the reservoir. The 12 acre pattern is highly instrumented with monitoring equipment and geotechnical devices from 29 vertical observation wells as shown (from Collins, 1994).

geomechanical shearing and dislocation continued. Additionally, the production well was throttled to maintain the temperature of the streaming bitumen just below steam saturation conditions. This prevents steam from entering the well bore and diluting the produced fluids. This process is known as the SAGD steam trap mechanism. There are many other engineering considerations for the SAGD process such as recovery rate, thermal efficiency, the costs and challenges associated with drilling truly horizontal wells, steam quality, steam injection rate, steam injection pressure, minimizing sand production, reservoir pressure maintenance, avoiding bottom water intrusion, and avoiding steam contact with potential thief zones.

The early piloting of the SAGD process at the UTF has proven that this process can deliver good rates and reserves from the reservoir at UTF, which is considered to have marginal vertical pay (Edmunds, 1999) compared to others areas of the Athabasca

deposit, as it is only 20 m thick in this location. One advantage of this location, however, is that the reservoir exists relatively untouched by major mud-plug facies that could act as permeability barriers and baffles to steam permeating through the reservoir (Strobl et al 1997). Success or failure of a SAGD program may lie in the ability to predict and avoid distributions of mud plug facies and shale stringers. Chapter 2 is devoted to characterizing and classifying top-quality oil-sands-reservoir facies so that they can be distinguished from non-reservoir facies using rock physics.

Although the bitumen deposit at UTF is good and high recovery was achieved, it should not be considered average conditions for the entire Athabasca region. In 1992 UTF Phase B began its initial steam and 8 years later is turned into its wind down stages. Unfortunately, much of the production related information remains proprietary currently and as such much of the interpretations shown in later chapters are, by necessity, incomplete. We anticipate that these data will become available at some time in the future at which time the analyses and predictions of the following chapters will need to be revisited.

1.3.4. Value of time lapse geophysics in the oil sands

Because the oil sands are widespread across the entire Athabasca deposit and are relatively easily found, the geophysical technologies currently applied are either for, 1) reservoir characterization and mapping, or 2) time-lapse imaging of reservoir production. The technical challenges in the former lie in finding the best quality vertically and laterally continuous reservoir. The technical challenges in the latter lie in correctly predicting the effective changes on the reservoir material, and designing an appropriate monitoring program that will be sensitive to such changes. Time-lapse monitoring is

ideal for oil sands because, as discussed, the combined influences of temperature, pore pressure, fluid saturations, and material damage directly and remarkably alter the reservoir rock properties, and hence the corresponding geophysical response.

Another advantage for time-lapse is that the Late Cretaceous McMurray Formation directly overlies Paleozoic carbonate rocks; and a pronounced impedance contrast is found at this interface. This strong seismic marker is helpful in mapping the static base depth of the reservoir, but it is also helpful in mapping the dynamic delay in seismic two-way travel time through the reservoir in response to the presence of steam. This geologic unconformity however, can also be a burden when mapping the lowermost McMurray formation. Due to the marked impedance contrast, the leading cycle of a band-limited pulse reflecting off of this interface can swamp the signal arriving earlier from within the shallower McMurray section; destroying important information from the lowermost region part of the reservoir.

References

Aheme, A., Maini, B., 2008, Fluid Movement in the SAGD process: A review of the Dover project, *Journal of Canadian Petroleum Technology*, Jan 41(1), 31-37.

Avseth, P., Mukerji, T., Mavko, G., 2005, Quantitative Seismic Interpretation: Applying rock physics tools to reduce interpretation risk, *Cambridge University Press*, 359pp.

Berryman, J., 1999, Origin of Gassmann's equations, *Geophysics*, 64, 1624-1627.

Biot, M. A., 1956, Theory of Propagation of Elastic Waves in a Fluid-Saturated Porous Solid: I Low Frequency Range, *Journal of the Acoustical Society of America*, 28, 179-191.

Biot M. A., 1956, Theory of Propagation of Elastic Waves in a Fluid-Saturated Porous Solid: II Higher Frequency Range, *Journal of the Acoustical Society of America* 28, (1956): 179-191.

Biot, M. A., and Willis, D. G., 1957, The elastic coefficients of the theory of consolidation, *Journal of Applied Mechanics*, 24, 594-601.

Birrel, G., Heat transfer ahead of a SAGD steam chamber: A study of thermocouple data from phase B of the UTF (Dover Project), *Journal of Canadian Petroleum Technology*, March V42 (3), 40-47, 2003.

Butler, R. M., 1997, Thermal Recovery of Oil and Bitumen, second printing, *Calgary: GravDrain.*

Brown, R., and Korringa, J., 1975, On the dependence of the elastic properties of porous rock on the compressibility of a pore fluid, *Geophysics*, 40, 608-614.

Calvert, R., 2005, Insights and Methods for 4D Reservoir Monitoring and Characterization, Society of Exploration Geophysicists, 2005 Distinguished Instructor Short Course.

Carcione, J., Picotti, S., Gei, G., Rossi, G., 2006, Physics and Seismic Modeling for monitoring CO_2 Storage, *Pure and Applied Geophysics*, 163(1), 175-207.

Chalaturnyk, R., J., 1996, Geomechanics of the Steam Assisted Gravity Drainage Process in Heavy Oil Reservoirs, Ph.D. thesis, University of Alberta.

Chow, L., and Butler, R.M., Numerical Simulation of the Steam-assisted Gravity Drainage Process (SAGD), *Journal of Canadian Petroleum Technology* June, V35 N6, 55-61, 1996

Collins, P.M., Design of the Monitoring Program for AOSTRA's Underground Test Facility, Phase B Pilot, *Journal of Canadian Petroleum Technology*, March, V22 N3, 46-53, 1994

Collins, P., 2007, Geomechanical effects on the SAGD process: *SPE Reservoir Evaluation and Engineering*, August, 2007, 367-375.

Collins, P., 2004, The False Lucre of Low-Pressure SAGD: Petroleum Society.

Edmunds, N., On the difficult birth of SAGD, *Journal of Canadian Petroleum Technology*, Jan. 1999

Enders, A. L., and R., Knight, 1989, The effect of microscopic fluid distribution on elastic wave velocities, *The Log Analyst*, 30, 437-444.

Gassmann, F., 1951, Über die Elastizität poroser Medien, *Vierteljahrsschrift der Naturforschenden Gesellschaft in Zurich*, 96, 1-23.

Ito, Y., Ichikawa, M., and Hirata, T., (2004), Effect of Operating Pressure on the Growth of Steam Chamber Detected at Hangingstone SAGD project", *Journal of Canadian Petroleum Technology*, V43 N5, May, 47-53.

Leal, J., Murria, J. and Pedroza, M., 1995, Recent developments in subsidence monitoring and prediction in the Costa Oriental oil fields, Venezuela: in Land subsidence, edited by F.B.J.Barends et al., A.A.Balkema, Rotterdam, pp. 179-186.

Mavko, G., Mukerji, T., Dvorkin, J., 1998, The Rock Physics Handbook, Tools for Seismic Analysis in Porous media, *Cambridge University Press*, 329pp.

McCain, W., 1990, Properties of Petroleum Fluids, *Penwell Books*, 596pp.

Mindlin, R. D., 1949, Compliance of elastic bodies in contact, *Journal of Applied Mechanics*, 16, 259-268.

Ostrander, W., 1984, Plane wave reflection coefficients for gas sands at non-normal angles of incidence, *Geophysic*s, 49(10), 1637-1648.

Patterson, L., 1984, Diffusion-limited aggregation and two-fluid displacements in porous media: *Physical Review Letters*, 52, 1621-1624.

Schmitt, D.R, Seismic attributes for monitoring a shallow heated heavy oil reservoir: a case study. *Geophysics*, 65, 368-377, 1999.

Shin, H., and Polikar, M., 2007, Review of reservoir parameters to optimize SAGD and fast-SAGD operating conditions, *Journal of Canadian Petroleum Technology*, Jan 46(1), 41-47.

Strobl, R.S., Muwais, W.K., Wightman, D.M., Cotterill, D., and Yuan, L.P., Application of outcrop analogues and detailed reservoir characterization to the AOSTRA underground test facility, McMurray Formation, North Eastern Alberta, Petroleum Geology of the Cretaceous Mannville Group, Western Canada, CSPG, Memoir 18, 1997.

Yang, H., King, M., 1986, A Study of Elastic Wave Velocities in Dry and Water Saturated, Regularly Jointed Rock Masses*, International Journal of Rock Mechanics and Mining Sciences*, 23(3), 277-280 .

Widess, M.B., 1973, *How thin is a thin bed?*, Geophysics, 38, 1176-1180.

Chapter 2

Description and characterization of McMurray oil-sands

2.1 Introduction

Properties of materials in the subsurface can be studied using a number of qualitative and quantitative tools tailored towards observations at a variety of scales and resolutions. In this chapter, we try to incorporate and integrate many different types of visual and numerical data sets in order to give a complete description of McMurray Formation within the Athabasca oil sands that is relevant for seismic rock physics applications. Scanning electron microscopy (SEM) and optical microscopy provide detailed images of the texture and distribution of the smallest components of the oil sands; the matrix, the pores, and the pore fluids. These pictures give evidence of the depositional and diagenetic controls on the sediments and illustrate the unique complexity of this material. They also permit the accurate, albeit extremely localized, determination of matrix composition, porosity, and pore fluid saturation. A review of several engineering tests performed on small oil sands samples provides a description of the static mechanical behavior of oil sands. Such tests were carried out mainly for

geotechnical, civil and environmental engineering applications, but there are some observations that are relevant for seismic rock physics applications.

Geologically speaking, the McMurray formation is notoriously complex. Even at a small scale, core photographs display detailed sedimentary structures, traces fossil assemblages and stratigraphic relationships that cast the McMurray Formation in a complicated an intertwined mix sediments stemming form point-bar fluvial, estuarine, and marginal-marine tide-dominated environments (Hein et al., 2007, Carrigy, 1959).

The McMurray formation has been well studied, and because it is close to the surface, it is easily found. The objective of integrating all of this information is to come up with rock physics relationships that might aid in delineating good reservoir zones from poor reservoir zones.

2.2 Description of oil sands material

Scanning Electron Microscopy:

Athabasca bitumen is found most commonly in the late Cretaceous McMurray formation unconsolidated sands. The sands have an absence of cohesion, highly quartzose mineralogy, high porosity, and a lack of interstitial cement (Dusseault and Morgenstern, 1979). For the purpose of this thesis, this material will be referred to as oil sands material.

The grain surface characteristics of the oil sands material were studied with a scanning electron microscope by Dean Rokosh (personal communication). The purpose of the microscope examination was to identify those physical characteristics responsible for the behavior of oil sands, and to obtain an understanding of the geological history responsible for shaping these materials. Figure 2.1 shows an SEM image of typical McMurray oil sand. Oil sand, by definition lacks or has very little cementation. As such its moduli (bulk and shear moduli) are entirely dependant upon grain-to-grain contacts. These contacts are held in place by confining pressure, and any reduction in effective pressure will result in a reduction in effective moduli. The micrograph displays a subtle interlocked texture characterized by relatively high incidences of long and interpenetrative grain contacts. Furthermore, because bitumen is highly viscous, it may actually support the sand grains in much of this material and act as partial cement.

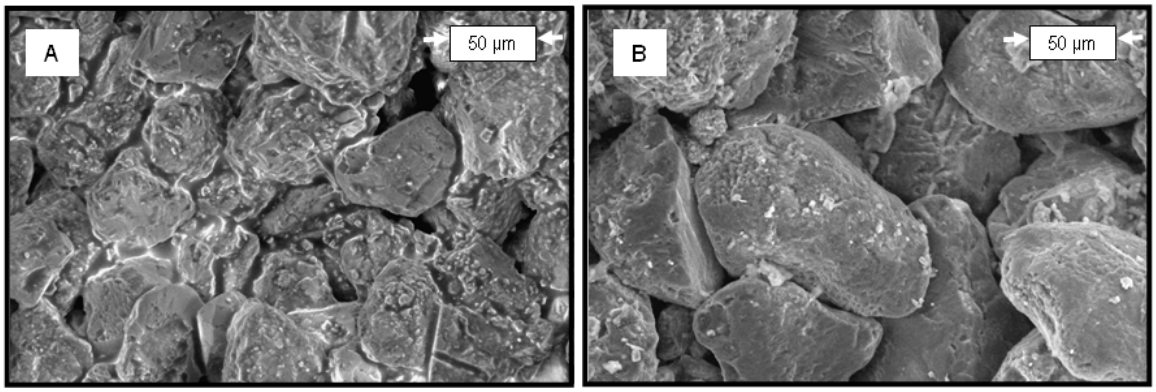

FIG. 2.1 SEM image of, A) un-cleaned oil sands material, and B) oil sands material with organic components removed (cleaned). The reflective and resinous material in cracks and pores of A is bitumen, and trace amounts of clay can be seen in both A and B.

Issler et al. (1999) has suggested that the McMurray formation within the Late Cretaceous was at one time buried much deeper than it sits today. This exaggerated

burial has accelerated or enhanced the impacts of a variety of diagenetic processes on these Quartz sands. For instance, solution and quartz overgrowths have formed on the periphery of the grains, which results in a densified, yet un-cemented aggregate with an interlocked structure. The aggregate is still cohesionless but now displays enhanced rigidity because of the additional diagenetic fabric. In geological engineering and soil mechanics communities this material has been given the name "locked sands" (Dusseault and Mortgenstern, 1977). As such, oil sands are unique natural materials for two reasons. First, the bitumen is essentially a solid at virgin reservoir conditions, and second, the sands grains themselves are not loosely packed sandstone. Instead, the grains have a dense, interlocked structure that has developed as a result of deep burial subjecting the material to higher temperatures and meteoric groundwater, but they have not undergone sufficient diagenesis to become fully lithified.

Static Engineering Tests

Shear testing of locked sands demonstrates that only small strains are required to fail the rock. Failure is accompanied by extremely high rates of dilation. This behavior is the result of a preferential interpenetrative fabric that forms during diagenesis. A modest increase in interpenetration greatly enhances the dilatant characteristics at failure. As mentioned in section 1.3, failure of these materials greatly enhances permeability and the SAGD process takes advantage of this behavior by injecting high pressure fluids coincident with melting and mobilizing the highly viscous bitumen.

FIG. 2.2. Map of oil sands deposits in Western Canada. The Athabasca Oil Sands is found predominantly in the McMurray Formation which is shallowest in the northern part of the deposit (where it is mine-able from surface) to over 600 m depth in the south near Cold Lake. The white circles denote the location of the UTF facility where the oil sands lie about 150 m below the surface. Image modified from http://en.wikipedia.org/wiki/Image:Athabasca_Oil_ Sands_map.png.

Why rock physics cannot use engineering tests to describe and characterize oil sand

Dusseault and Mortgenstern (1977) performed a series of triaxial and shearbox strength tests on oil sands core obtained from a drill hole. They observed that dissolved gases came out of solution and disrupted the core when brought to the surface. This disturbance was lessened by using of down-hole freezing, cold storage (at -18^0C) and special trimming procedures. Tests were performed at the formation temperature of 4^0C, and also at room temperature. No differences in mechanical strength were observed, and the authors therefore concluded that bitumen viscosity did not contribute to the overall shear strength of the material. However, one potential problem with the samples they chose to analyze is that they did not have any oil saturation and they had been partially exposed and weathered at the surface.

They also noted that although oil sands material disintegrates readily when placed unsupported in water, it is strong in its intact state under some confining stress. Support of this statement is found on site at the UTF project (figure 2.2) where a vertical mine shaft has been driven vertically through the Athabasca oil sands reservoir, and the tunnel displayed excellent short term stability without structural support (Collins, 1997). This mechanical strength is also evident from the unusually high slopes along the Athabasca River. Steep natural slopes over 60 m high have been observed and open pit excavations have been as great as 50 m at inclinations of over 65º.

Oil sands have been studied extensively with an emphasis on strip mining operations, or road construction on top of oil sands exposed at surface, however many mechanical and rheological studies were tailored for engineering applications and are not

transferable to seismic rock physics. The mechanical behavior of a oil sands subjected to the dynamic and largely reversible strains from an impulsive passing seismic wave in-situ will be completely different than the quasi-static mechanical response imposed on oil sands by tunneling, strip mining or transporting heavy loads across its surface.

2.3 Geological data and geological setting

The Lower Cretaceous McMurray formation of the Athabasca oil sands sits on an angular unconformity that truncates Devonian strata (figure 2.3). Near the UTF site, Devonian strata comprise primarily limestone and calcareous shales of the Waterways

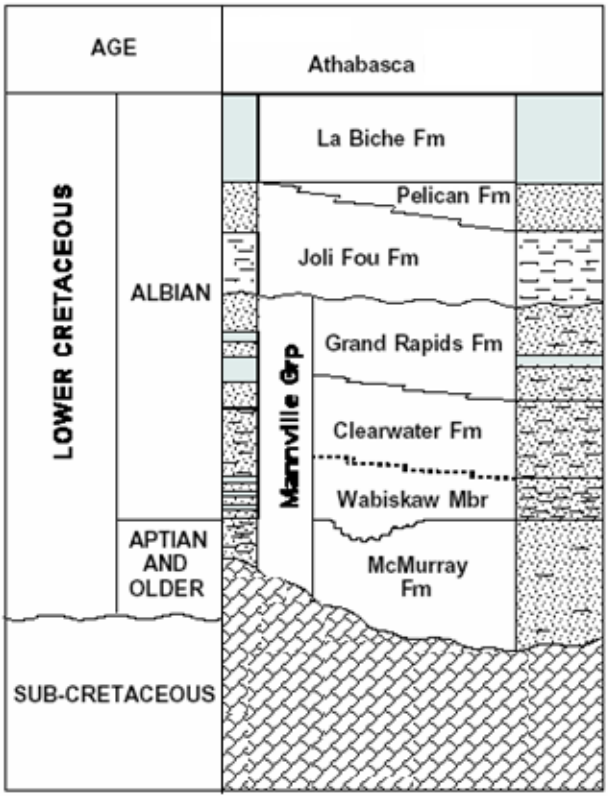

FIG. 2.3. Stratigraphic chart showing the geologic setting of the Athabasca oil sands (modified from Wightman, 1982).

Formation. In general, the McMurray formation was deposited in incised valleys and stacked channel complexes that were formed by fluvial processes and subsequently transgressed by marginal marine-environments during an early Cretaceous sea-level rise. Therefore, the McMurray displays a spectrum of depositional environments ranging from point-bar fluvial in the lower parts, to estuarine in the middle, to marginal marine and shoreface facies[2] near the top.

The McMurray Formation has been studied for more than 50 years and throughout that time the rocks have been interpreted and re-interpreted many times. The current general consensus is that the McMurray Formation can be subdivided into 3 major members: a lower member containing primarily point bar and estuarine sedimentary facies, a middle member containing higher proportions of estuarine and open water influences, and an upper member containing sedimentary facies from a predominantly estuarine and marginal marine setting. Dalrymple et al. (1992) defined an estuary as: the seaward portion of a drowned valley system which receives sediment from both fluvial and marine sources and which contains facies influenced by tide, wave and fluvial processes. Lettley et al., 2007, states that esturaries are commonly formed during transgression (rise in sea level), when the increase in accommodation space outpaces the flux of sediment being carried downstream from continental erosion. As such estuaries are geologically short lived features. "Estuaries act as depositional sinks, receiving sediment from both fluvial and marine sources. . . Taken in this context, it is apparent that estuarine deposits display great internal complexity, reflecting local variation in depositional setting and flucuations in sediment availability" (Lettley et al., 2007).

[2] In geology, facies refers to a body or bodies of rock with specified characteristics.

The variety of lithologies, trace fossils, and sedimentary structures seen within the McMurray formation suggest a number of depositional environments. River morphology types in the lower McMurray range from braided to meandering and are probably best seen represented in the lower McMurray formation, with meandering river types being dominant (figure 2.4). Fining upward sequences can be several metres thick and are characteristic of point bar lateral accretion in meandering river systems. These settings account for the spectrum of sand/mud laminated interbeds found within the lower and middle McMurray; locally refered to as inclined heterolithic stratification, often just referred to as IHS. (Thomas et al., 1987). Depending on the percentage of mud content, the thickness of the individual layers, and the connectivity of bitumen filled sand, IHS can range from high quality reservoir to poor reservoir. An IHS set is composed of inclined units, each of which contains a coarse-grained (typically sand), and fine-grained (clay, silt and / or sand) depositional fraction. Sediment deposited within an inclined unit can either be arranged as discrete coarse and fine laminations, or as a normally graded bed. IHS is generally attributed to point bar growth within a channelized setting, but may form on any large-scale inclined surface that undergoes accretionary translation (Thomas et al., 1987). Within the McMurray formation, IHS deposits have been attributed to lateral accretion within brackish-water (estuarine) channels (Lettley et al, 2007). Braided river deposits are most likely composed of randomly interbedded, cross-bedded and rippled units with no systematic upward change in grain size or mud content.

It is probably impossible to map all of the lateral and vertical spatial variations in facies within the McMurray Formation, because multiple fluvial channels and estuarine complexes have recursively shaped and re-shaped the landscape (figure 2.4). Though, an

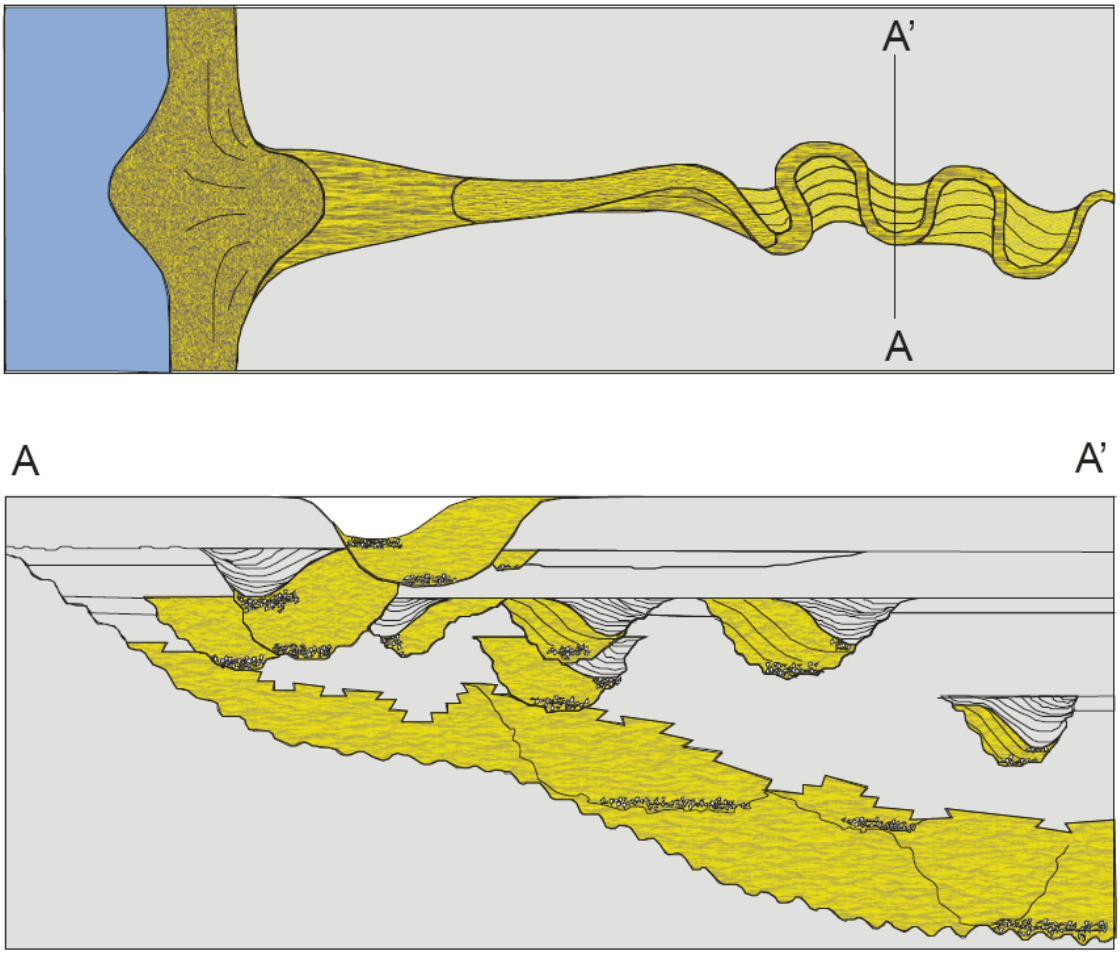

FIG. 2.4. Depositional model of the McMurray formation. Much of the McMurray formation was deposited in upper estuarine channel sand laterally accreting point bars. The distribution of reservoir facies (1-3) and non-reservoir facies (4-5) are indicated in yellow and grey respectively. These are referred to later in the text.

understanding of the primary spatial relationships of the different facies should be helpful to guide exploration more accurately.

It is probably impossible to correlate more than 5 or 6 facies within the McMurray if an interpreter is constrained to boreholes, but Flack, 1984, mentioned that Syncrude geologists have identified over 60 facies that are useful in delineating and tracking bitumen rich zones in their strip mining operations. All classification schemes

within the McMurray formation, no matter how detailed or how general, cast facies in terms of a spectrum of increasing mud content (figure 2.5). The best reservoir sand is on the left (facies 1), and the worst reservoir material is on the right (facies 5). For seismic rock physicists, a simpler classification scheme might be sufficient. Namely, if seismic rock physics can highlight or discriminate between reservoir facies (1-3) and non-reservoir facies (4-5), then it will be able to bring incredible value to the exploration and exploitation of the best parts of the McMurray reservoir. Of course, knowledge of the shale and mud plug distribution in the reservoir is valuable.

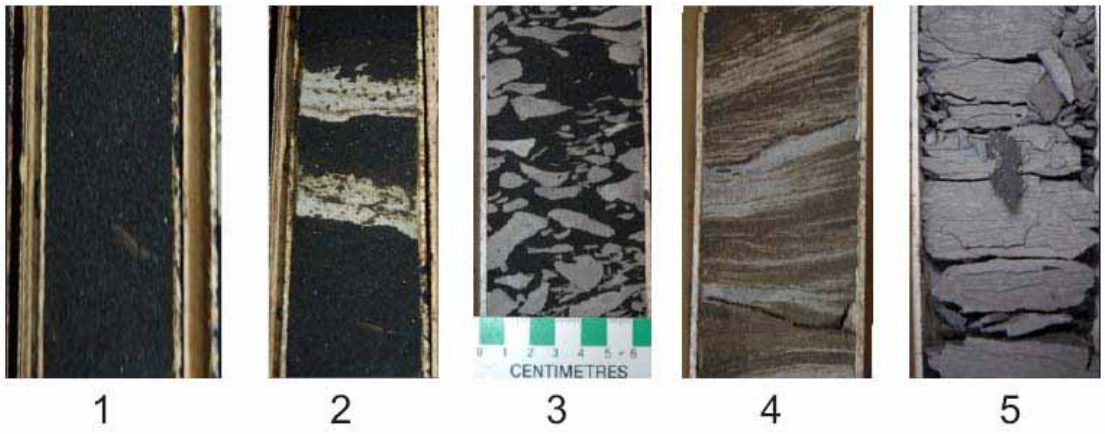

FIG. 2.5. Core photographs of the 5 major facies within the McMurray formation characteristic of a meandering river system with laterally accreting point bars: 1) oil sand (reservoir facies), 2) oil sand with intermittent inclined mud beds, 3) oil sand with mud clast breccia, 4) muddy dominated inclined heterolithic stratification, 5) mud plug.

Facies 1: Oil sand

The grain size of sands in the lower member is on average, coarser than that of the middle and upper members. The coarsest sediment is almost always found near the base of the formation and each member as a whole has a fining-upwards tendency. A relative

lack of fine-grained sediments in the lower member, compared to the overlying middle member deposits, suggest that less suspended load sediment was carried by these rivers. The lack of fines results in thick, continuous reservoirs with few shale breaks where channel sands are stacked (Flack, 1984). High-grade bitumen deposits are dominated by clean, well-sorted sand, and are likely to occur in thick and areally extensive channel deposits (Lettley et al., 2007). The clean cross-bedded Facies 1 sand bodies are thought to represent the deposits of subaqeous dune complexes developed seaward of the river channel system (top panel, figure 2.4). Furthermore, a contiguous section of pristine oil sands facies can be attained by the juxtaposition and stacking of several independent channel systems throughout geologic time (bottom panel, figure 2.4). This results in effectively increasing the total vertical thickness of the reservoir that can be exploited.

Facies 2: Oil sand with intermittent inclined mud beds (Sandy IHS)

Bedding with gently dipping decimeter to metre thick beds of fine grained sand and current rippled sand (dark brown in color from complete oil saturation), separate from thinner (1 cm to 10 cm) partings of shale and interlaminated sands and shale. Locally facies is often referred to as “sandy IHS”. IHS is called sand dominated if more than 50% of the laminations are bitumen saturated sand. Thin shale breaks increase in abundance stratigraphically upwards and the sands become more argillaceous and less heavily oil saturated. Although sandy IHS is generally thought to be an adequate reservoir rock, even the very thinnest mud beds (as small as a few centimeters as shown in figure 2.4) may act as barriers or abductors of spreading steam.

Facies 3: Oil sand with mud clast breccia

These breccias are thought to be formed by localized mass wasting events (cutbank "landslides") on the laterally accreting point bars. Although oil sand with mud clast breccia actually contains less sand per unit volume than facies 2, it is generally thought to be a better reservoir material for in-situ exploitation. The shale clasts in this facies do not act as continuous blockages and steam would easily move around the clasts and penetrate the surrounding oil sand.

Facies 4: Mud dominated inclined heterolithic strafication (IHS)

Usually found in the top portions of fining upward sequences, muddy dominated IHS. stems from a similar depositional setting as facies 2, but has more than 50% of its volume made up of dipping mud laminations. Because of the high mud content, the small scale permeability is shut off and the coarser grained beds typically have less than 100% bitumen saturation. This presents as a light brown staining (Figure 2.4) as opposed to dark brown to black. The fact that bitumen is only partially saturating the pore space of the coarse sand intervals is an indication that permeability was low at the time of oil migration and subsequent biodegradation. The sedimentary structures in this facies are easily observed in core, whereby the color contrast provided by the partial bitumen saturation gives a direct indication of grain size; if the beds are gray then it is composed of fine grains, if the beds are brown then it is composed of coarser sand and bitumen has moved in. Facies 4 is typically classified as having no-reservoir potential for in-situ operations, but perhaps may still have sufficiently high amounts of bitumen content to warrant strip mining extraction.

Facies 5: Mud plug or shale plug

Mud plugged flood plain or channel fill deposits are completely unsaturated with bitumen, hence their gray color, and are unwanted facies members that disconnect the McMurray reservoir system. These fine-grained non-reservoir facies types come from vertical accretion deposits on flood plains of meandering rivers (clay-dominated), or are marginal to open marine silt dominated channel fills (figure 2.6). Non-reservoir facies occur as commonly as good reservoir facies within the McMurray formation, and accurately identifying these facies is essential so that they can be avoided.

Surely because of the heterogeneity and extremely recurrent incised valley complexes involved, sedimentologists and geomorphologists will rightly argue that the McMurray Formation cannot be crudely grouped into only 5 facies catagories. In fact, due to the variable character of McMurray IHS. deposits, Lettely et al. (2007) classify IHS facies alone into five sub-categories. These classifications are based primarily on relative positioning within a conceptual estuary environment and permit more accurate deciphering of the stratigraphic architecture between wells. It will be shown in the next section however, that borehole derived rock physics parameters do not have the sensitivity to distinguish between, say, IHS with 60% sand with thick mud lamination sets versus IHS with 60% sand with thin mud lamination sets. Seismically these

materials may have similar expressions, but the former may actually be a barrier to steam growth, whereas the latter may be perfectly suitable reservoir. If a mud bed is less than a few centimeters thick, then it is likely that steam will be able to break through it. Integrating descriptions from drill core will help address uncertainties and challenges associated with predicting minor steam baffles and barriers. Well log based cross-plotting of various combinations of rock properties will allow for a clear discrimination between larger scale reservoir and non-reservoir zones.

The above categorization is intended to provide a descriptive label by which the

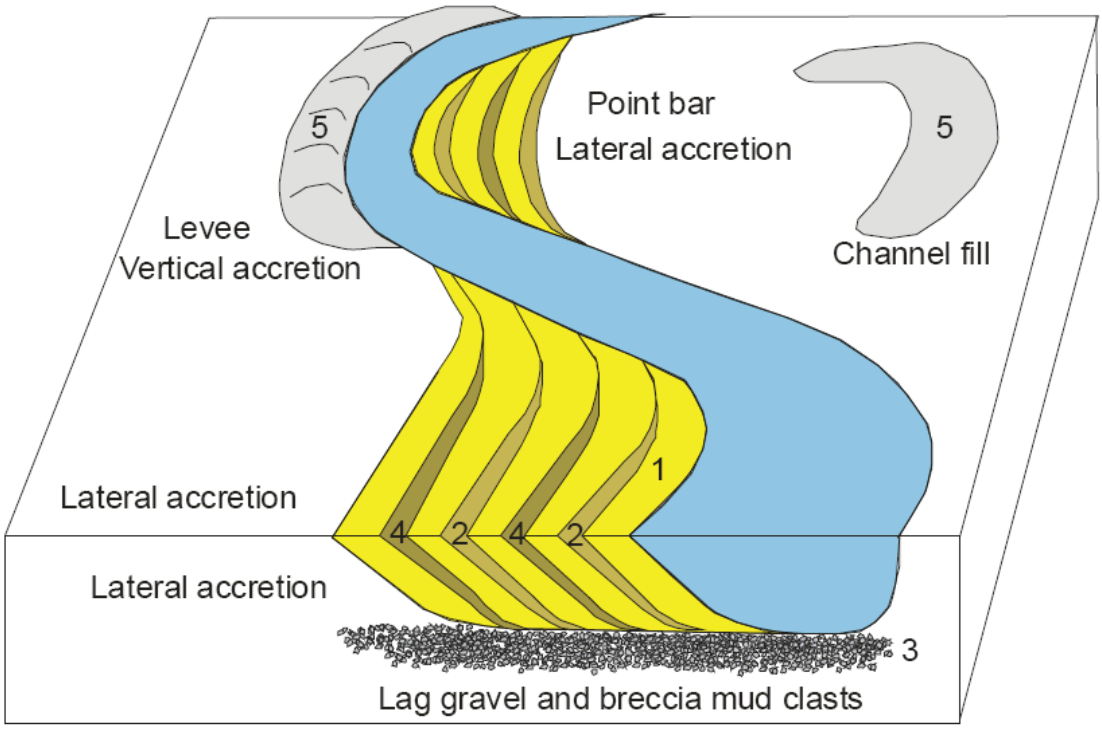

FIG. 2.6. Schematic of a point bar lateral accretionary complex morphology. The facies shown in figure 2.5 are shown in numbered here (1-5) in their likely position within this system.

physical properties of one facies unit may be differentiated from another facies unit. If it can be shown that the physical properties of reservoir (facies 1-3) are different from non-reservoir (facies 4-5), then reflection seismology (after implementing rock physics inversion) may have the capacity to spatially map bitumen distributions and permeability heterogeneities throughout a region of interest.

2.4 Rock property relationships from cross-plotting

A wealth of geological insight can be gained directly from drill core, and a remarkable amount of sedimentary features can be seen within a few metres of strata. However, geophysical remote imaging methods, such as seismic reflection surveying, will not be sensitive to all of the details contained within the core, but will sample the bulk physical properties of the material. If there is a substantial difference in the rock properties between, say, facies 1 and facies 5, then perhaps this information can be used to calibrate seismic measurements and characterize high probability pristine reservoir. In practice, if there are parameters of facies 1 that plot in a region of space that is independent from facies 5, then those parameters can be used to tell them apart. We are looking to see if facies units have any organization or clustering, so their rock properties can be used to identify them in the absence of drill core.

Data Set

There is an absence of complete and sufficient wireline logs in the immediate vicinity of the UTF to allow a rigorous borehole rock physics study on site. Dipole sonic

logs[3] are the most important log for rock physics analysis, because all elastic constants can be calculated if V_P, V_S, and density are known. Although there are hundreds of well logs within a few kilometer radius of the UTF, unfortunately few of these are publicly available dipole sonic logs that penetrate through the McMurray Formation and its surrounding rock packages. In this section, the rock physics relationships for two wells are presented in the following section. This should be regarded as a very local description of the reservoir parameters collected from borehole measurements. Because the McMurray Formation and Athabasca deposit are so widespread, it is not advised that these measurements be taken as representative values over the entire region or applied directly to other geographic locations. The two wells used in the analysis (named AB/16-05-093-12W4, and AA/09-10-093-12W4) penetrate similar strata as those encountered at UTF but are located at ~2 km and ~3 km to the southeast of the UTF project respectively. For brevity, AB/16-05-093-12W4 will be referred to as well 1 (figure 2.7), and AA/09-10-093-12W4 (not shown) will be referred to as well 2 in the following sections.

Cross-plots of V_P versus V_S

As discussed in section 1.2, borehole measurements of effective V_P, V_S, and ρ allow for the direct computation of any effective elastic property desired. Figure 2.8 shows cross-plots of V_P versus V_S through the McMurray and overlying Clearwater formations for well 1 (top row) and well 2 (bottom row). The gamma ray logging is a method of measuring the natural radioactivity of the rock to characterize a rock or sediment within a

[3] Dipole sonic logs are geophysical measurements within the borehole of the transit times of both P-waves and S-waves through a fixed interval (usually a few metres) in the formation. They provide a high frequency (>1000 Hz), highly sampled (~ every 0.1m) velocity structure within the immediate vicinity of the borehole.

borehole. Different materials emit different amounts and different spectra of gamma radiation. In particular, shales usually emit more radiation than other sedimentary rocks because radioactive potassium is a common component in their clay content, and because the cation exchange capacity of clay causes them to absorb uranium and thorium. Each lithology type (shown by the gamma ray color scale) plots in a characteristic region on a V_P versus V_S scatter-plot. Values of V_P and V_S for Clearwater marine mudstones and shales in 2.8(A) can be completely enclosed by a polygon so that it is isolated from the data points within the underlying McMurray Formation. The resistivity color-scale attached to the V_P-V_S cross-plots (Figures 2.8 (C) and (F)) shows a remarkable separation of reservoir versus non-reservoir facies based on this cross-plotting approach. High quality oil sands facies 1 (the bright yellow points in (E)) have slightly lower V_P and V_S values than sandy IHS. or muddy IHS (B); scatter points plot slightly closer to the origin without overlapping the space defined by the overlying Clearwater facies.

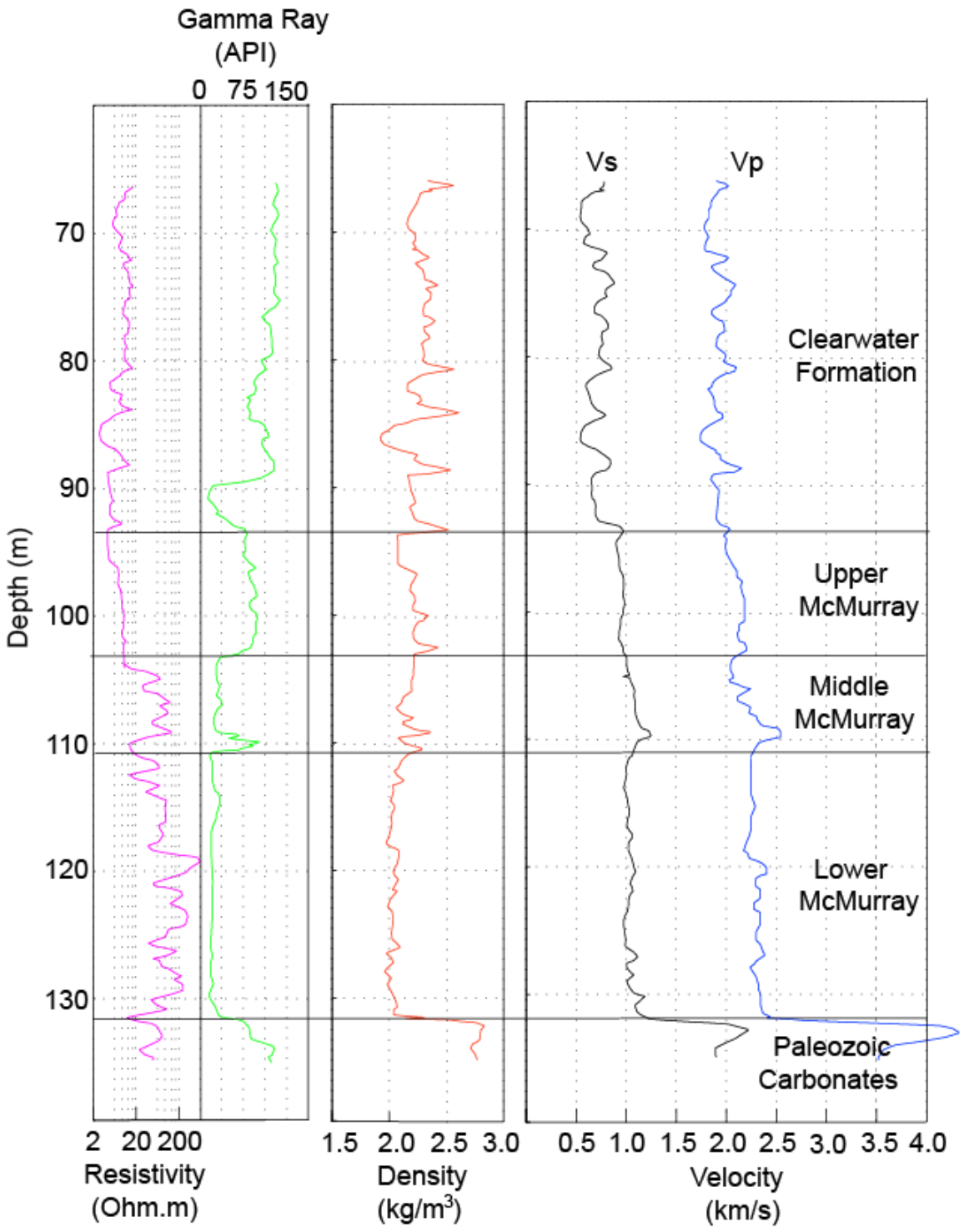

FIG. 2.7. Wireline logs for AB/16-05-093-12W4 (well 1).

It is apparent that the reservoir facies (facies 1-3) has a characteristic and restricted region in V_P and V_S space by which it can be distinguished from non-reservoir facies (facies 4-5). Note that the data points have more overlap vertically (V_P direction) than horizontally (V_S direction). This means that shear wave velocity is a better property to use to separate out these different facies types.

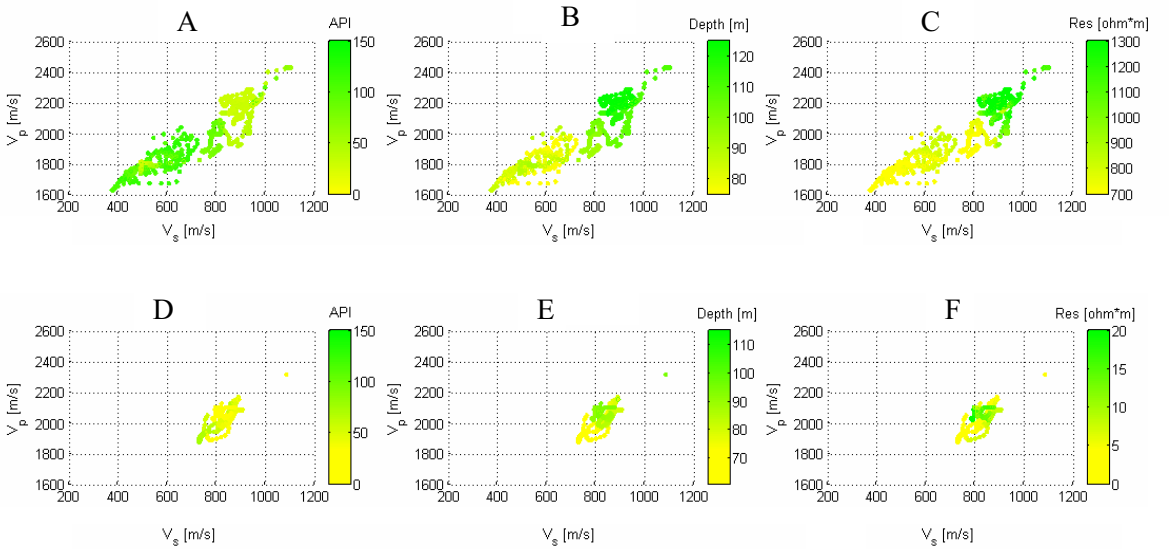

FIG. 2.8. Scatter-plot of *Vp* vs. *Vs* values for AB/16-05-093-12W4 (top row), and AA/09-10-093-12W4 (bottom row). The color-scales display values of gamma ray, depth and resistivity at each point sampled going left to right across the columns. The units "API" stand for American Petroleum Institute, and represent a standardized radioactivity reading useful in identifying different lithologies.

Cross-plots of different combinations of elastic constants

V_P and V_S alone may provide sufficient separation in cross-plot space in order to delineate lithologies, but with the addition of mass density they all can be used to compute any combination of elastic constants desired (see table 1.2). Goodway (1999) demonstrated that the Lamé constants are more useful for understanding lithologic variations, independent of fluid effects, by analyzing fundamental changes in rigidity μ, Lamé parameter λ, and density ρ, as opposed to a mixture of parameters contained within the expressions of seismic velocities or impedances. The main argument is founded on the observation that P-impedance and S-impedance (or similarly, P-velocity and S-velocity) are not mutually exclusive, in part because they both contain rigidity and density (eqns. 1.1 and 1.2), and as such, log curves tend to track each other and never cross over. Goodway showed that by contrast, $\lambda\rho$, and $\mu\rho$ curves are "orthogonal with regard to Lamé parameters or moduli, unlike P-impedance versus S-impedance, thereby making the cross plot more discriminating". This method of separating the effects of rigidity from incompressibility was first explored on gas reservoirs but can be applied in the oil sands. Figures 2.10 and 2.11 display scatter-plots of a variety of elastic constants for well 1 and well 2 respectively. Different graphical domains serve to either weakly or strongly separate out facies types in a number of ways. The following is a list of the nine combinations of elastic constants (A-I) shown in the figures below, along with a brief description and motivation for it:

A	K vs. μ	Compressibility vs. Frame rigidity
B	λ vs. μ	Lamé compressibility vs. Shear modulus
C	ρV_P vs. ρV_S	P-impedance vs. S-impedance
D	$K\rho$ vs. $\mu\rho$	Density is not easily de-coupled from $K\rho$ and $\mu\rho$ in seismic inversion schemes
E	$\lambda\rho$ vs. $\mu\rho$	Seismic data is easily inverted to obtain $\lambda\rho$ and $\mu\rho$ inversion volumes (Goodway, 1999)
F	V_P/V_S ratio vs. Resistivity	V_P/V_S ratio vs. oil saturation and less so clay content
G	V_P vs. ρ	P-velocity versus bulk density
H	V_S vs. ρ	S-velocity versus bulk density
I	V_P/V_S vs. ρ	V_P/V_S ratio versus density

Table 2.1: Rock property domains.

Beacause bulk density is a weakly constrained parameter in AVO inversion, it is more accurate to keep it tied to other elastic constants. As figure 2.10 and 2.11 show, $\lambda\rho$ vs. $\mu\rho$ crossplot displays the best discrimination between facies 1-5. Also of interest is sub-panel F, in each of these figures. It appears that the sand dominated facies (1-3) have distinguishably lower Vp/Vs ratio values than facies 4 and 5. For instance facies 1 (oil sand) and facies 2 and 3 are well constrained to 1.9 ± 0.1 and 2.5 ± 0.25 respectively. However mud dominated facies exist over a wide range from 2.75 to 4.5. Thus, Vp/Vs ratio may indeed be a suitable attribute for mapping reservoir versus non-reservoir zones across seismic profiles.

Since it is commonly practiced in the petroleum industry, a summary of the facies distributions is presented specifically for $\lambda\rho$ vs. $\mu\rho$ to coincide with Goodway's methodology and workflow for AVO analysis and interpretation. Here, in $\lambda\rho$ vs. $\mu\rho$ cross-plot space, we see a gradational trend in facies distribution based on increasing mud-content. The ultimate goal of this cross-plotting method is to assign tangible geologic units to seismic rock property values computed from seismic inversion.

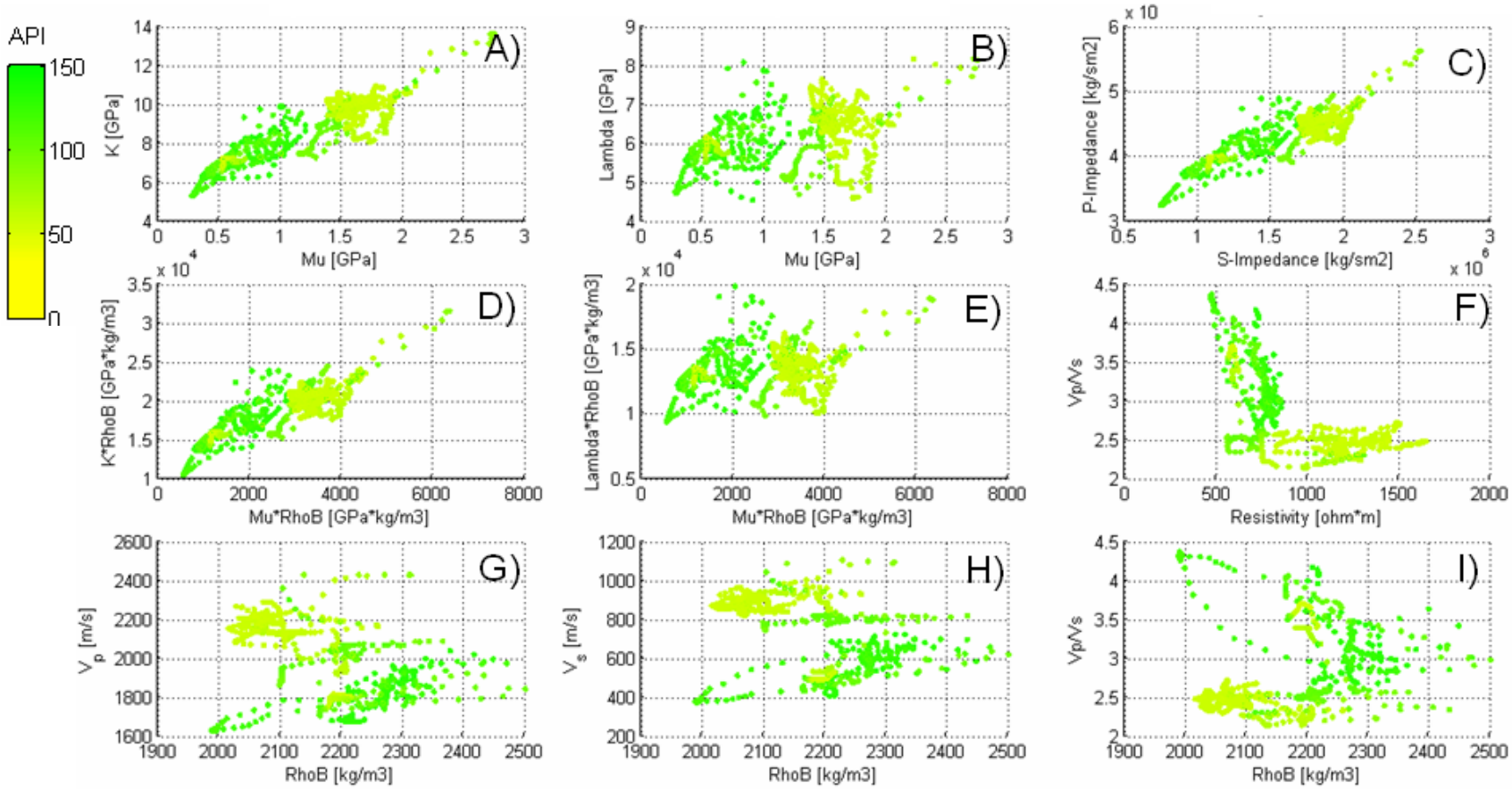

FIG. 2.10. Cross-plot relationships for a number of different elastic parameters for well 1. Each depth sample is colored according to its Gamma-ray value, low values are yellow, high values are green.

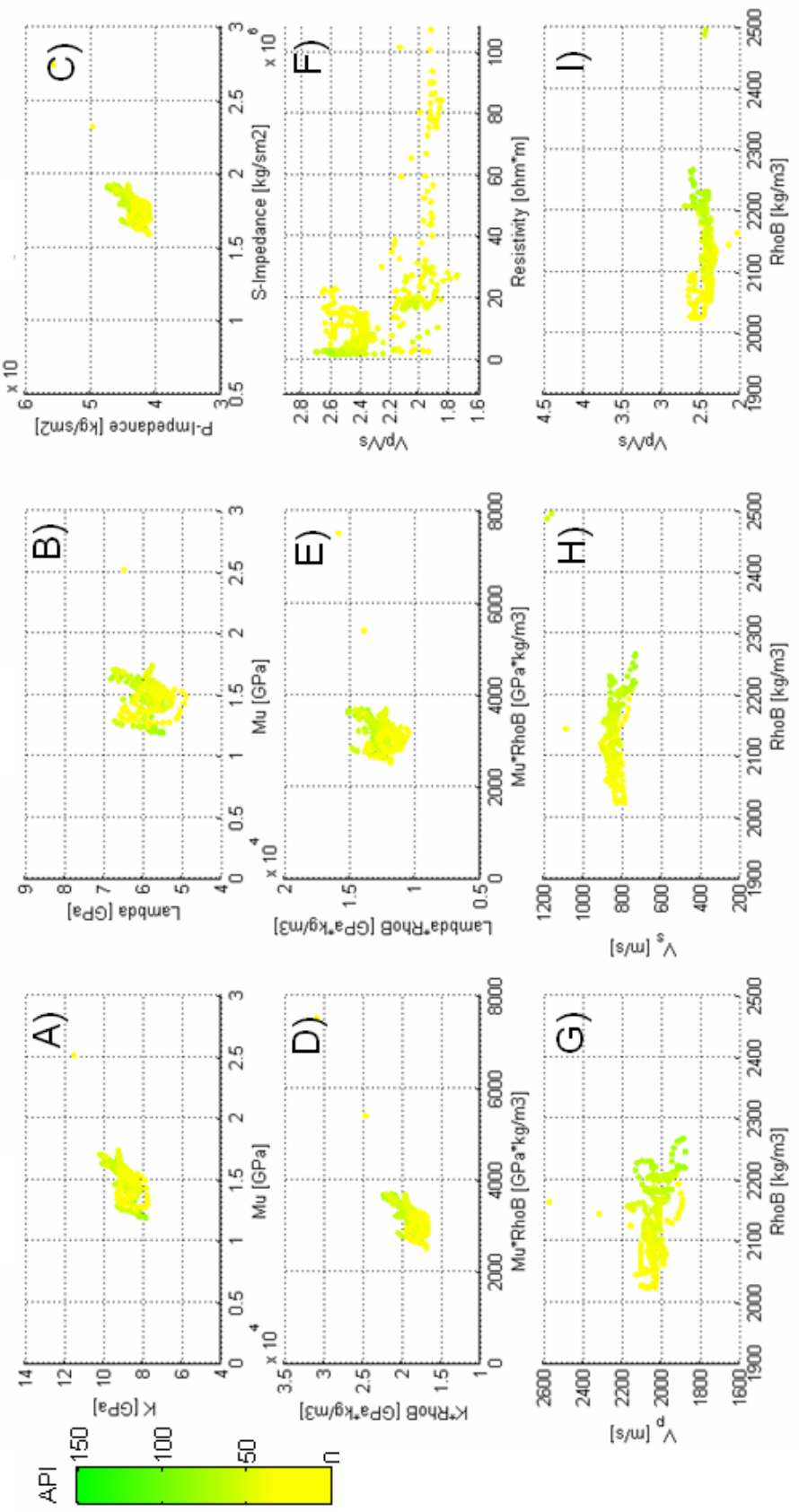

FIG. 2.11. Cross-plot relationships for a number of different elastic parameters for well 2. Each depth sample is colored according to its Gamma-ray value, low values are yellow, high values are green.

2.5 Investigation of elastic impedance and P-to-S converted wave elastic impedance for reservoir characterization

This section is composed as a standalone subset of Chapter 2 with the intention to be read as an independent paper in and of itself. It may include some redundancy from previous sections.

Motivation

It was shown in the previous section that if acoustic impedance (ρV_P) and a parameter related to shear-wave velocity can be estimated from borehole data (or seismic data), the ability to discriminate between different lithologies will increase. This section is motivated by the notion that independent post-stack[4] inversions on partial offset seismic data (i.e. near and far offset stacks, or single offset stacks) may have greater sensitivity to lithology and fluid substitutions than high redundancy, full-fold stacked seismic data. The input to the inversion of range-limited seismic data cannot be acoustic impedance, but must be some non-zero angle equivalent expression.

Doing pre-stack inversion of individual CDP gathers and inverting directly for V_P, V_S, and density have been tested in several ways, but the estimated parameters are often poorly determined. One, more robust approach is to apply post-stack inversion on partial stacks or constant offset gathers. To invert a vertical-offset seismic trace, acoustic impedance can be calculated directly from the well logs. However, for far-offset traces

[4] The term 'stack' in geophysics is used to describe the summation of information from different shot records together for the purpose of reducing noise and increasing the signal and overall data quality. The number of traces that have been added together to produce a stacked trace is called the 'fold'. Adjacent stacked traces are often plotted next to each other so that coherent waveform events can be used to give a continuous appearance of the reflecting interfaces or layering. The word 'stack' is also used, somewhat ambiguously, to refer to an entire 2D line or 3D volume where trace stacking has occurred. 'Post-stack' refers to the resulting output of the trace summation process usually used to produce an image of the subsurface.

or stacked traces, an equivalent of the acoustic impedance can be used to calibrate the non-zero-offset seismic reflectivity. Connolly (1999) developed a pseudo-property or seismic attribute that was sensitive to this variation that he called the elastic impedance (EI) as was already discussed in section 1.2. He demonstrated how, by using elastic impedance logs he was able to perform inversions of far-offset seismic data.

An extension of this technology describes another function in the same fashion – P-to-S converted wave elastic impedance (PSEI) – for linking converted-wave seismic to wells. PSEI is similar to EI but it is adapted to accommodate the conversion of P-waves to S-waves collected from 3-component geophones. Analogously to EI, it too can be computed from acoustic log data (P-wave and S-wave velocities and density) and can be used for well calibration, wavelet estimation, and inversion of P-S reflectivity data leading to improved interpretability and utility of converted wave seismic records.

Theory

As shown in section 1.2, elastic impedance, defined by Connolly (1998), is a generalization of acoustic impedance for non-normal angles of incidence:

$$EI(\theta_P) = \alpha^a \beta^b \rho^c \,, \tag{2.1}$$

$$\begin{aligned} a &= 1 + \tan^2 \theta_P \\ b &= -8K \sin^2 \theta_P \\ c &= (1 - 4K \sin^2 \theta_P), \end{aligned}$$

where K is usually set to the average value of $(\beta / \alpha)^2$ over the log interval of interest and θ_P is the incidence angle of the P-wave (note: $\beta = V_s$, $\alpha = V_p$).

Elastic impedance aids in the inversion of non-zero offset data because it provides a log trace derived from a set of P-wave velocity, S-wave velocity, and density logs,

consistent with the reflectivity of a far-offset-angle stack data in the same way that acoustic impedance logs are used to calibrate zero-offset seismic data.

An undesirable feature of the EI function is that its dimensionality varies with incidence angle thus providing numerical values that change significantly with θ_P. These problems have been overcome by Whitcombe (2002), who modified the EI function with reference constants α_o, β_o, and ρ_o, which remove the variable dimensionality of equation 2.1. This delivers an EI function which returns normalized impedance values (with units of impedance; $kgm^{-2}s^{-1}$) for all angles θ_P.

If the values of these constants are chosen to be averages of the α, β, and ρ, logs then $EI(\theta)$ will vary around unity. This modification removes the dimensionality dependence and stabilizes the function. If we further scale this function by a factor $\alpha_o\rho_o$, the dimensionality of EI becomes the same as AI and we find that $EI(\theta_P)$ predicts the correct values of acoustic impedance $\alpha\rho$, at $\theta_P = 0$:

$$NEI(\theta_P) = \alpha_0 \rho_0 \left(\frac{\alpha}{\alpha_0}\right)^a \left(\frac{\beta}{\beta_0}\right)^e \left(\frac{\rho}{\rho_0}\right)^d \quad . \tag{2.2}$$

To achieve this new normalized form of $EI(\theta_P)$, we have effectively scaled the original definition by $\alpha_o^{1-a}\beta_o^{-b}\rho_o^{1-c}$.

These modifications allow for direct comparison between elastic impedance values across a range of angles in a manner that was not possible with the previous formulation. The modification neither improves nor degrades the accuracy of reflectivity that can be derived from the EI function. It provides a quick and easy way to condition log data for input to a post-stack-type inversion on partial- or single-angle-stack seismic data.

In a similar way to Connolly, P-to-S converted wave elastic impedance PSEI (or shear impedance, for short), was defined by Mavko and Gonzalez (2003) as,

$$PSEI(\theta_p) = \beta^e \rho^d,$$
$$e = \frac{K \sin\theta_p}{\sqrt{1/K^2 - \sin^2\theta_p}}\left(2\sin^2\theta_p - 1/K^2 - 2\cos\theta_p\sqrt{1/K^2 - \sin^2\theta_p}\right), \quad (2.3)$$
$$d = \frac{4K \sin\theta_p}{\sqrt{1/K^2 - \sin^2\theta_p}}\left(\sin^2\theta_p - \cos\theta_p\sqrt{1/K^2 - \sin^2\theta_p}\right),$$

where $K = V_S / V_P$. Here, at a critically defined angle θ_P', the density term becomes insignificant, and the PSEI value is governed solely by the V_s term. This particular angle alone can be diagnostically applied to discriminate lithology and or reservoir parameters. An investigation of the "drop-out" of this density term for the McMurray reservoir can shed light on reservoir characterization, lithology identification, and optimal seismic acquisition and imaging geometries (e.g. K. Wolf, personal communication). Similar to Whitcombe (2002), the dimensionality problem can be overcome by scaling $PSEI(\theta_P)$ by a factor $\beta_0^{1-e}\rho_0^{1-d}$:

$$NPSEI(\theta_P) = \beta_0\rho_0\left(\frac{\beta}{\beta_0}\right)^e\left(\frac{\rho}{\rho_0}\right)^d. \quad (2.4)$$

Methodology

The objective of this study is to simulate and ultimately use the $NEI(\theta_P)$ and $NPSEI(\theta_P)$ log data for partial angle stack inversions of the McMurray reservoir. Non-zero offset seismic data is not available in this study, but the curves can still be calculated for insights on characterization and lithology discrimination. The intention is not to perform AVO analyses, but to identify key angles (either in *NEI* or *NPSEI* formulations) that are most useful for partial-offset stack inversions. Upon analysis, it is suspected that

particular angles of incidence will better highlight reservoir and non reservoir zones, or that indicate the onset of the fluid substitution and production related changes in a time-lapse sense. V_p, V_s, and density logs were taken from well AB/16-05-93-12W4/0 in the Western Canadian Sedimentary Basin which is located approximately 3 km south of the from the UTF site. This was the only data available relatively close to the site, as dipole sonic logs (presenting shear wave information) have not been routinely run in this area. A more comprehensive study could be carried out to generalize or calibrate the effects over the whole of the McMurray area,

Results

The major facies of interests are; 1) the Clearwater marine mudstones and shales that overlie the McMurray formation, 2) the non-reservoir terrestrial mudstones and siltstones within the McMurray, 3) the unconsolidated bitumen saturated oil sand with the McMurray, and 4) the underlying Paleozoic carbonates upon which the McMurray reservoir sits. Figure 2.13 shows calculated elastic impedance and shear impedance variations as a function of incidence angle (θ_P) for these 4 major facies types. McMurray oil sand (solid line) completely differs from the McMurray mudstones ('+' symbols), and from the Clearwater mudstones (triangles), in both its *EI* response and *PSEI* response. Significant deflection from the acoustic impedance value ($EI(0^o)$) occurs only at angles greater than 35º.

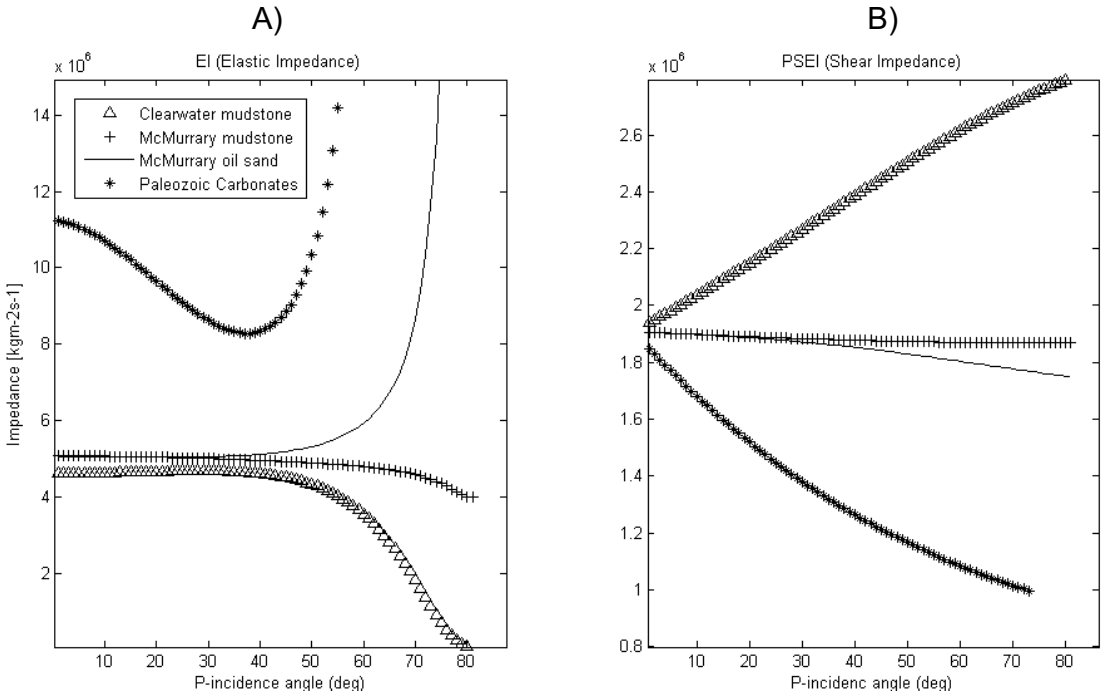

FIG. 2.13. Elastic impedance (A) and Shear impedance (B) as a function of P-wave incidence angle.

This analysis can be extended along the entire length of a log interval of interest. Many authors (e.g. Connolly, 1999, Duffaut et al., 2000, and Gonzalez, 2004) have recognized an enhanced sensitivity to fluid saturations and lithology simply by placing an elastic impedance log (calculated at a fixed non-zero angle) next to the zero-angle elastic impedance (i.e. acoustic impedance) log. Although, this procedure is sufficient for the well calibration and inversion at a single non-zero angle, the natural extension of this method is to plot the curves for all possible angles. The best way to display this log is as a colored 2-D matrix, as opposed to many 1D log traces placed side by side. Such color displays are aligned next to other curves (such as gamma-ray) for correlation purposes. Figure 2.14 displays a detailed log calculation of the normalized EI and PSEI for all incidence angles. EI and PSEI image logs have been created by computing $NEI(\theta_P)$ and $NPSEI(\theta_P)$ for $0^o \leq \theta_P \leq 85^o$. The impedance values are scaled by a color bar, and plotted

as a function of angle (horizontal axis) and depth (vertical axis). Panel A is a log track showing the 3 input parameters for the calculated NEI log (panel B) and NPSEI log (panel C). Panel D is a log track of the so-called facies indicators (gamma-ray and resistivity).

Figure 2.15 shows NEI and NPSEI values scaled by the zero-angle trace. This form highlights the deviation of impedance away from unity as angles increase from vertical incidence. This illustration clearly shows that the 4 facies units penetrated each have a distinctive EI and PSEI character. For instance, in figure 2.5.3 we see that the Clearwater mudstones go from white to yellow to dark blue, from left (0º) to right (85º). This corresponds to a slight increase from a base acoustic impedance of ~4.5x10^6 kgm^{-2}s^{-1} to a maximum of ~4.8x10^6 kgm^{-2}s^{-1} at 30º, before plummeting towards 0 kgm^{-2}s^{-1} as θ_P approaches 85º (this shown graphically by the triangles in figure 2.5.1.A). In contrast, the oil sands behave just the opposite. They decrease slightly from a base acoustic impedance of ~5.0x10^6 kgm^{-2}s^{-1} to a minimum of ~4.8x10^6 kgm^{-2}s^{-1} at 30º and then dramatically increase to very large values. At angles greater than 65º, the values for oil sands are clipped by the color scale. Table 2.2 summarizes the analysis qualitatively, by identifying the shape of the curve, (whether the colors increase or decrease) from the baseline value of acoustic impedance (*NEI(0º)*). Oil sand is the only facies whose EI increases and PSEI decreases at larges angles.

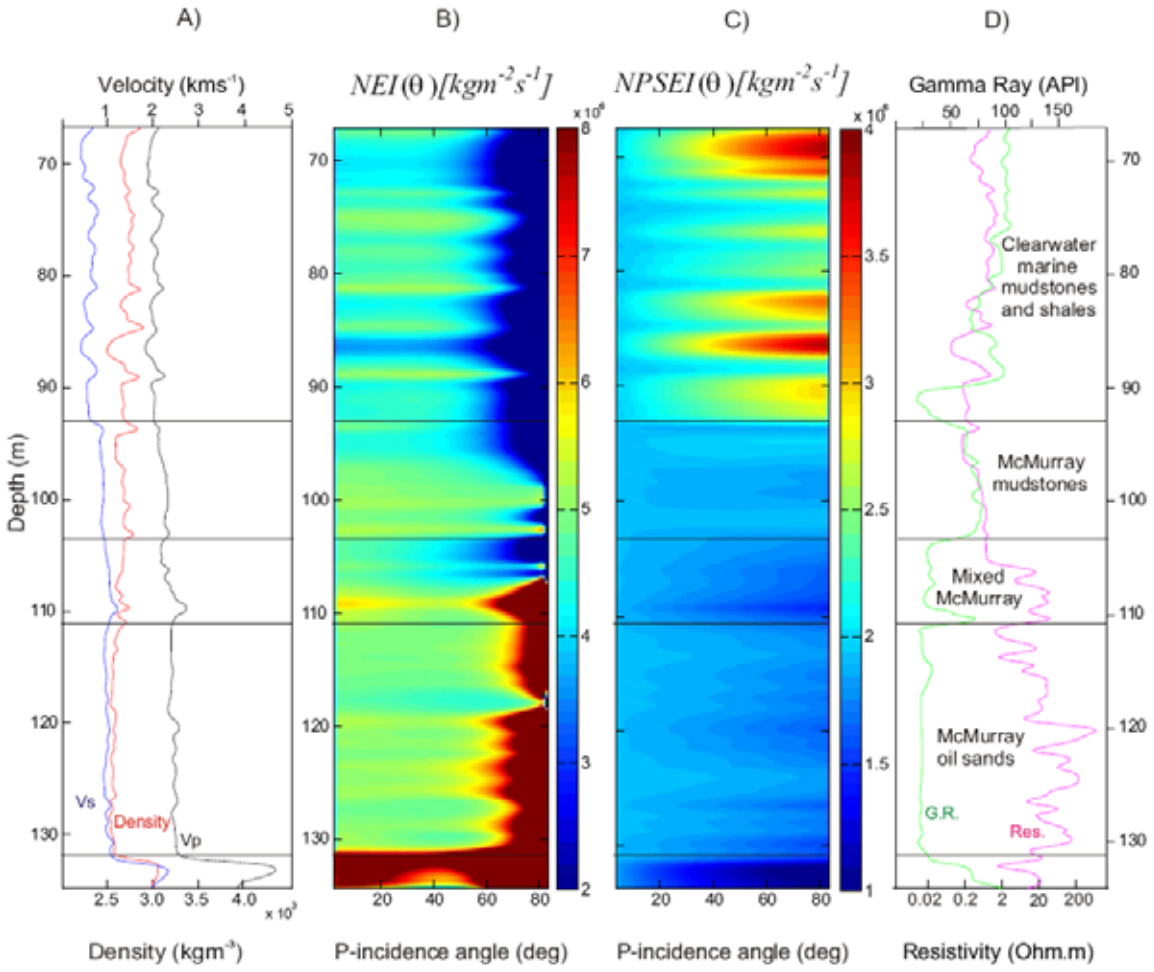

FIG. 2.14. Computation of absolute *NEI* and *NPSEI* values for all possible incidence angles *(0-90°)*. This is a typical well log through the McMurray formation. Log tracks of A) V_p, V_s, and density (the input parameters to equations 2.2 and 2.4), B) normalized elastic impedance as a function of angle, and C) normalized P-to S-converted wave elastic impedance as a function of angle, and D) Gamma-ray and resistivity logs (the facies indicators).

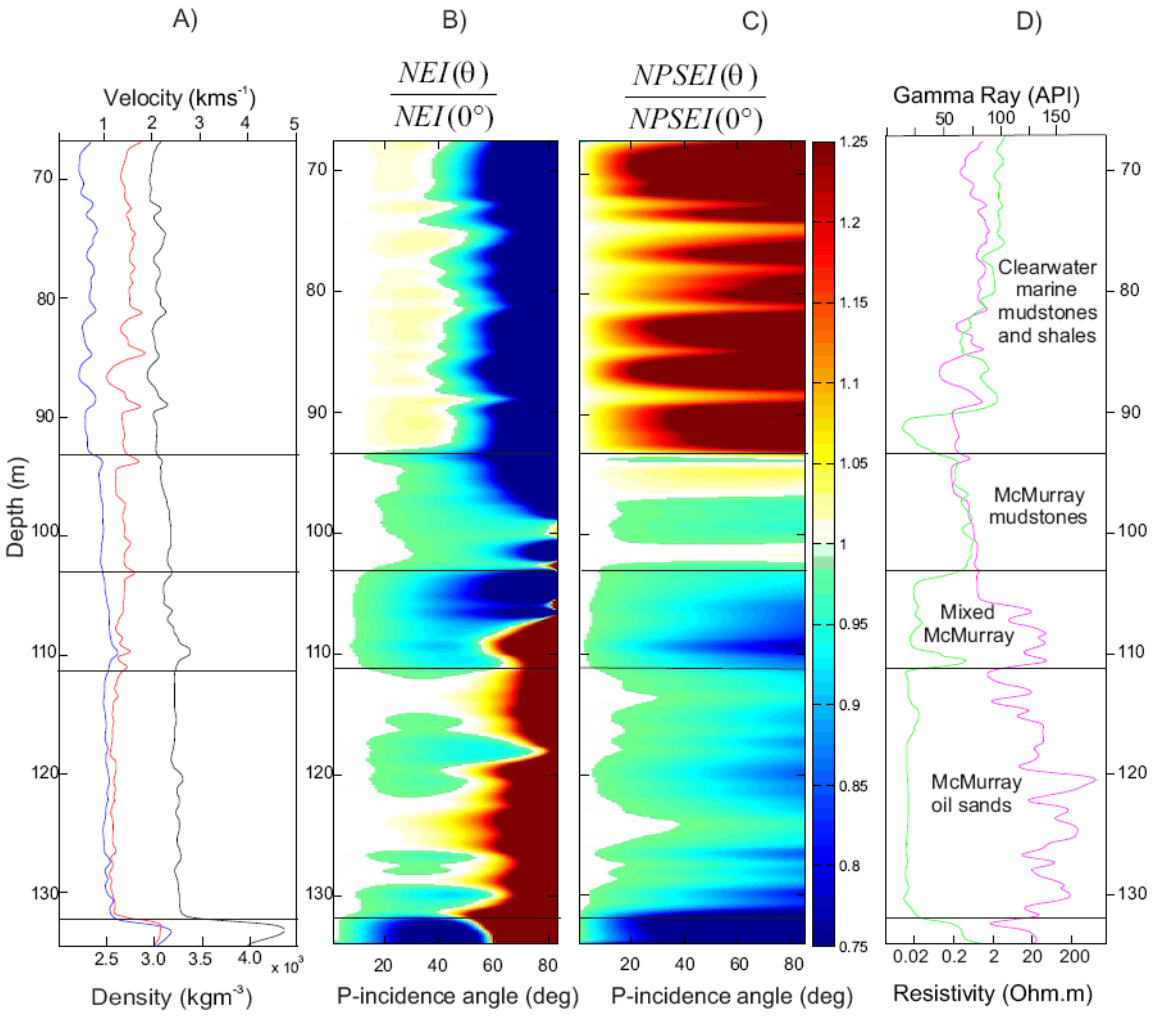

FIG. 2.15. Computation of scaled *NEI* and *NPSEI* values for all possible incidence angles *(0-90°)*. Typical well log through the McMurray formation. Log tracks of A) V_p, V_s, and density (the input parameters to equations 2.2 and 2.4), B) normalized elastic impedance (*NEI(θ°)*) divided by vertical incidence elastic impedance (*NEI(0°)*) value. C) P-to S-converted wave elastic impedance (*NPSEI(θ°)*) divided by vertical incidence elastic impedance (note $EI(0^o) = PSEI(0^o) = AI = \rho V_p$) , and D) Gamma-ray and resistivity logs (the facies indicators).

	Scaled EI	Scaled PSEI
Clearwater (marine mudstones and shales)	↑ then ↓	↑
McMurray mudstones	↓	↓
Mixed McMurray (interbedded silts and oil sands)	↓ or	↓
	↓ then ↑	
McMurray oil sands (bitumen saturated reservoir)	↓ then ↑	↓

Table 2.2 Facies classification based on curve shape for the scaled EI, and scaled PSEI log calculations.

Discussion

Hydrocarbon detection and mapping with AVO has been used within the oil and gas industry, and some companies use AVO routinely to attempt to reduce risk associated with potential drilling locations. An increasing number of practitioners insist on quantitative agreement between synthetic models and real data before using this technique. Current research in synthetic modeling addresses a wide range of topics. Synthetic models are only as good as the data that goes into them. The fundamental question, "How should logs, sampled every 15 centimeters, be averaged or blocked in order to produce layered earth models more akin to what surface seismic methods encounter?" Or, "What is the effect of layer thickness on AVO response?" Or, "Can seismic waves be approximated as rays or is it better to use seismic wave theory?"

Geological taxonomy uses parameters such as thickness, grain-size, composition, density, saturation, porosity, permeability, color, etc., each of which are *intrinsic layer* properties of earth materials. Geophysicists speak in terms of velocities and densities; however the data recorded in seismology is really an expression of reflectivity; an interface or discontinuity property. The EI and PSEI calculations in this section are direct attributes of a single rock sample, not a boundary between two rock types (refer to eqns. 1.14 and 1.18)

EI and PSEI are attributes that depend on incidence angle, therefore, seismic inversion has to be done with an angle limited approach to utilize these data. Ray tracing limitations in creating a reliable offset-to-angle transform, as well as wavelet variability, place restriction on the ultimate utility of such inversions. In order to compute an inversion of, say $EI(30^o)$, a single trace hitting the location of interest at 30º must be collected. However, in order to improve the signal to noise ratio, the input to the inversion could be a partial angle stack covering an angle range of say, 20º – 40º. Performing synthetic tests, specific to the study area, is required to analyze the impacts of these practical considerations on computed EI and PSEI log values.

Future work in studying the EI and PSEI response in oil sands regions is to incorporate fluid substitution models to build synthetic $EI(\theta_p)$ and $PSEI(\theta_p)$ synthetic log curves. Such efforts would strive to highlight the angle dependant sensitivity of the SAGD process (changes in pressures, densities, bulk modulus, etc) on the seismic response. The angle sensitivity of different fluid substitutions might be apparent. For example, and the numbers chosen here are completely arbitrary for illustrative purposes, perhaps the bubble point (the point at which gas exsolves from the bitumen) can be most

strongly detected at say, 48º, whereas perhaps the replacement of bitumen with hot water can be seen most clearly at say, 22º.

As with the development of AVO class anomalies (e.g. Ostrander, 1984) the offset-dependant characteristics of impedance probably fall into a number of general classes, not yet defined. Future work is required to establish an equivalent class of impedance anomalies for a number of geologic and rock physics environments.

References:

Aki, K. I., and Richards, P. G., Quantitative seismology, W. H. Freeman & Co.: 1980.

Carrigy, M., 1959, Geology of the McMurray Formation, Pt. III General Geology of the McMurrary Area, *Research Council of Alberta, Memoir 1*, (available from the Alberta Geological Survey).

Castagna, J.P., Batzle, M.L., and Eastwood, R.L., 1985, Relationships between compressional-wave and shear-wave velocities in clastic silicate rocks: *Geophysics*, 50, 571-581.

Connolly, P., 1998, Calibration and inversion of non-zero offset seismic: 68th SEG meeting, New Orleans, USA, Expanded Abstracts, 182–184.

Connolly, P., 1999, Elastic Impedance: *The Leading Edge*, 18, N. 4, 438-452

Dalrymple, R.W., Zaitlin, B.A., and Boyd, R., 1992, Estuarine facies models: Conceptual basis and stratigraphic implications: *Journal of Sedimentary Petrology*, 62, 1130-1146.

Duffaut, K., Alsos, T, Rogno, H., Al-Najjar, N. F., Landro, M., Shear-wave elastic impedance: *The Leading Edge,* November 2000, 19(11), 1222-1229.

Dusseault, M.B. 1977, Stress state and hydraulic fracturing in the Athabasca oil sands, *in* D.A. Redford and A.G. Winestock, (eds.): The oil sands of Canada-Venezuela; Special Volume 17; The Canadian Institute of Mining and Metallurgy, pp. 27-35.

Dusseault, M. B., Morgenstern, N. R., 1979, Locked sands, *Journal of Engineering Geology*, 12, 117-131.

Flach, P.D. (1977), A lithofacies analysis of the McMurray Formation, Lower Steepbank River, Alberta; unpublished University of Alberta M.Sc. thesis 139pp.

Flack, P.D., 1984, Oil sands geology – Athabasca deposit north, Geological Survey Department, Alberta Research Council, Edmonton, Alberta, Canada.

Gonzalez, E. F., Mukerji, T., Mavko, G., and Michelena, R.J., 2003, Near and far offset P-to-S elastic impedance for discriminating fizz water from commercial gas: *The Leading Edge*, 22, no. 10, 1012-1015.

Goodway W., Chen T., and Downton J., 1997 *"Improved AVO fluid detection and lithology discrimination using Lamé parameters; lr, mr and l/m fluid stack from P and S inversions"*, CSEG National Convention Expanded Abstracts 148-151.

Hein, H., Cotterill, D., Berhane, H., 2000, An Atlas of Lithofacies of the McMurray Formation , Athabasca Oil Sands Deposit, Northeastern Alberta, Surface and Subsurface, *Alberta Energy and Utilities Board*, 217pp.

Issler, D., Willett, S., Beaumont, C., et al., 1999, Paleotemperature history of two transects across the Western Canada Sedimentary Basin: Constraints from apatite fission track analysis, *Bulletin of Canadian Petroleum Geology,* 47(4), 475-486.

Ivory, J., De Rocco, M., Scott, K., Schmidt, L., 1990, Effect of Temperature and Initial Oil Saturation on the Steam-Air Injection Process, Alberta Oil Sands Technology and Research Authority – Internal Report.

Leblanc, R.J., 1972, Geometry of sandstone reservoir bodies: Memoir 18, American Association of Petroleum Geologists, p. 133-190.

Lennox, T.R., 1982, The impact of geology on the design and performance of in-situ projects, Proceedings of the Second International Conference on heavy crude and tar sand, Caracus Venezuela, pp. 979-984.

Leopold, L.B. and Wolman, M.G., 1960, River meanders, *American Association of Petroleum Geologists Bulletin*, v.25, pp.305-313

Lettley, C. D., Pemberton, G. S., Gingras, M. K., Ranger, M. J., and Blakney, B.J., 2007, Integrating Sedimentology and ichnology to shed light on the system dynamics and paleogeography of an ancient riverine estuary, in MacEachern, J. A., Bann, K. L., Gingras, M. K., and Pemberton, G.S. (eds.), Applied Ichnology, Society for Sedimentary Geology.

Miall, A.D., 1977, A review of the braided river depositional environment, *Earth Science Reviews*, v.13, pp. 1-62.

Mossop, G.D., 1980, Facies control on bitumen saturation in the Athabasca Oil Sands, in Miall, A.D. (ed.), Facts and principles of world petroleum occurrence, Memoir 6, Canadian Society of Petroleum Geologists, pp.609-632.

Mossop, G.D. and Flach, P.D., 1983, Deep channel sedimentation in the Lower Cretaceous McMurrary Formation, Athabasca Oil Sands, Alberta, *Sedimentology*, v.30, pp.493-509.

Nelson, H.W., and Glaister, R.P., 1978, Subsurface environmental facies and reservoir relationships of the McMurray Oil Sands, northwestern Alberta, *Bulletin of Canadian Petroleum Geology*, v.26, pp.177-207.

Ostrander, W., J., 1984, Plane-wave reflection coefficients for gas sands at non-normal angels of incidence: *Geophysics*, 49, 1637-1648

Pemberton, S.G., Flach, P.D., and Mossop G.D., 1982, Trace fossils from the Athabasca Oil Sands, Alberta, Canada, *Science*, v.217, pp.825-827

Thomas, R.D., Smith, D.G., Wood, J. M., Visser, J., Calverly-Range, E. A., and Koster, E. H., 1987, Inclined heterolithic stratification: Terminology, description, interpretation and significance: *Sedimentary Geology*, v.53, 123-179.

Whitcombe, D., Elastic impedance normalization: *Geophysics*, 67(1), 60-62.

Wightman, D., 1982, Sedimentology and Stratigraphy of the Upper Mannville in parts of East-Central Alberta, *AAPG Bulletin*, 66(5), 642-643.

Zoeppritz K. 1919. Erdbebenwellen VIIIB; On the reflection and propagation of seismic waves: *Gottinger Nachrichten* I, 66–84.

Chapter 3

Seismic rock physics of steam injection in heavy-oil reservoirs

3.1 Abstract

This chapter reports results of modeling the rock physics properties of heavy oil reservoirs subject to the Steam Assisted Gravity Drainage (SAGD) thermal enhanced recovery process. Previously published measurements of the temperature dependant properties of heavy oil saturated sands are extended by fluid substitutional modeling in order to assess the effects of pore fluid composition, pressure and temperature changes on the seismic velocities of unconsolidated sands. Rock physics modeling is applied to a shallow reservoir (135-160 m depth) within the bituminous Athabasca oil sands deposits in Western Canada in order to construct a rock physics velocity model of the SAGD process. Ternary diagrams quantify the nuances of multiphase fluid properties on the effective compressional wave velocities of the reservoir material and summarize this information for a range of pressure and rock moduli scenarios. Although the injected steam pressure and temperature controls the fluid bulk moduli within the pore space, the stress dependant elastic frame modulus is the most important factor governing the

changes of seismic properties during this recovery operation. The results of the fluid substitution are then used to construct a simple 1-D synthetic seismic model and a 2-D synthetic seismic section in order to establish seismic attributes for analysis and interpretation of the physical SAGD process.

3.2 Introduction

The world's heavy and bituminous oil sand accumulations containing hydrocarbons with densities larger than 900 kg/m^3 (equivalent to API specific gravity $\leq$ 21) are becoming an increasingly important resource. A fundamental challenge in reservoir evaluation and production is the lack of understanding of the inherent geological complexity of most reservoirs, which leads to large uncertainties in estimates of total recovery, and recovery rates. Seismic methods are playing a larger role in solving production problems and reducing ambiguities of fluids within the subsurface. The desire has been, by using seismic waves, to know where the reservoir fluids are moving to and from during the enhanced oil recovery processes. In order for this to be done effectively, the seismic and mechanical properties of various reservoir fluids as well as the rocks that house them must be well understood. Then attempts can be made to quantify seismic measurements of changing reservoir conditions caused by recovery processes.

Modern thermal recovery techniques, particularly the Steam Assisted Gravity Drainage method (SAGD, Butler, 1994) and its various modifications, now allow for the exploitation of heavy oil reservoirs. During a SAGD program, high quality steam, typically in a temperature range between 150 ºC and 300 ºC, is injected into the reservoir from horizontal well bores (figure 3.1). Ideally, a steam chamber is established in the

reservoir after an initial soaking phase, which grows upward and then out laterally. The steam chamber grows by lowering the oil's viscosity at its edges allowing the oil to drain downward for removal through the production well. Within the central part of the steam chamber the oil has largely been removed and the pore space is replaced by high quality steam. The periphery of the steam chamber is in contact with a zone of undepleted reservoir that is heated through conduction. The engineering models (e.g. Butler, 1996) assume that oil melts at the ceiling and lateral edges of the steam chamber and then flows along its sides to the bottom via gravity drainage, where it is produced through a second horizontal well.

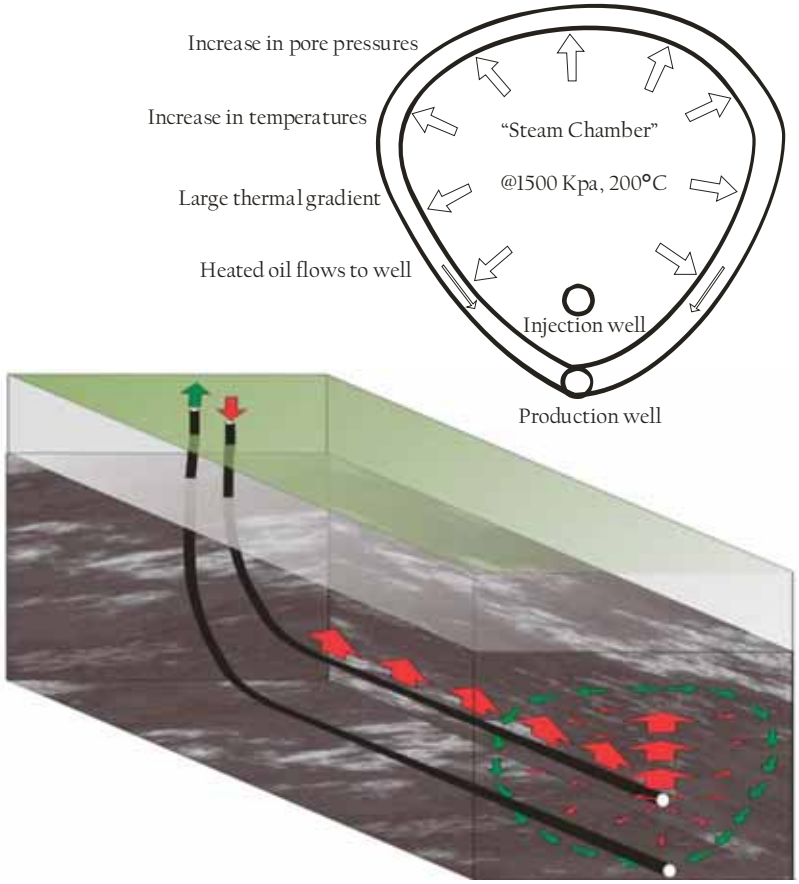

FIG. 3.1. Schematic of the SAGD process.

Hot steam continues to displace the heavy oil, causing the steam chamber to grow laterally into the virgin reservoir as long as there is a sufficient heat input to overcome conductive thermal losses.

Such oil recovery processes are complicated and expensive, particularly if portions of the reservoir are bypassed or if steam leaks outside of the reservoir; this latter situation has potential environmental and even human safety concerns. Indeed, pressurized steam has already escaped to the surface in one such blowout at the Total E&P site near Fort McMurray in 2006. An impermeable layer of shale sits between the bitumen and large freshwater aquifers in this region, and if the steam chambers blew out, the water could be large groundwater resources could be contaminated. Therefore remote surveillance of the reservoir should be increasingly important to assist in engineering and operational decision making. Because SAGD is still in its early stages, most companies only do rigorous testing and monitoring during the early stages of production and fail to consider the long term behavior of the process. Continuous conformance and gradual steam growth along the axis of the well bores allow for the most efficient and economic expenditure of steam, which adds value to the process. By-passed sections within the reservoir, either due to pressure driven steam break-through, or geologically controlled permeability heterogeneities, can dramatically reduce the success of an exploitation program. The importance of seismic monitoring programs for heavy oil reservoirs in Western Canada is reflected by the studies of Pullin et al. (1987), Eastwood (1994), Schmitt (1999), Li et al. (2001), Watson et al. (2002), and Zhang and Schmitt (2003), to name only a few.

The suggestion that the seismic monitoring of thermal enhanced oil recovery processes is possible was initially based on laboratory observations of a significant decrease in the compressional velocity with temperatures in heavy oil saturated materials. For example, Wang et al. (1990), Wang and Nur (1990), Wang and Nur (1988), and Eastwood (1993) all report reductions of the P-wave velocity of approximately 11% with heating of a heavy oil saturated sample from 20ºC to 120ºC at constant effective pressure. While this change certainly is considerable, such measurements do not take into account the fact that, in the field the actual zone of heated oil is small (e.g. Birrell, 2003) relative to the zone in which steam replaces some fraction of the heavy oil in the pore space.

Reservoirs in which SAGD is applied typically have from 10 m to 30 m of continuous vertical pay. Such thin reservoirs may make imaging fluid contacts or delineating steam zones with seismic methods difficult, particularly if the changes are subtle. For instance, Schmitt, (1999) identified bright seismic amplitudes, waveform interference and tuning that corresponded to a triplet of SAGD well pairs over a shallow bituminous Athabasca reservoir (figure 3.2).

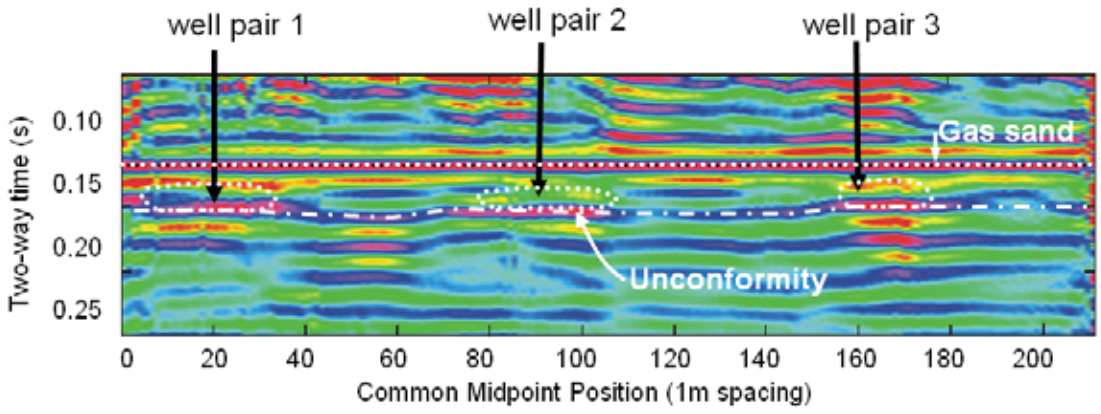

FIG. 3.2. Processed seismic section showing amplitude variation along 3 well pairs actively steaming in an Athabasca reservoir. Well pairs are coming in and out of the page (from Schmitt, 1999).

Typically during operation, the ambient pore pressure in the reservoir first controls the minimum injection temperature of the steam. In order to maintain the steam phase during and after injection, the temperature is chosen such that it matches or is greater than the thermodynamic steam saturation conditions for the in-situ pore pressure. The pressure is maintained just below the fracture pressure of the reservoir at the top of the steam chamber, which must be lowered as the steam chamber rises over time. Elevated pore pressures have been observed in advance of the steam chamber (e.g. Chalaturnyk, 1996), and because oil sand is unconsolidated, this actually facilitates shearing and dislocation to occur. This shearing likely aids in the evolution of the steam chamber and in the drainage of oil as permeabilities have been reported to increase by a factor of 10 (e.g. Collins, 2007). Also, injection pressures must be taken into consideration so as not to fracture the reservoir beyond the steam chamber.

Figure 3.3 displays the pressure-temperature phase diagram for water. The two phases, liquid and vapor, are separated by a steam saturation curve that defines the conditions at which liquid water and steam co-exist (Theune, 2004) . Furthermore, steam quality refers to the degree of mixed water in liquid and vapor phases co-existing at the boiling point for a given pressure. This co-existence is a latent heat effect. Water at the boiling point and pure steam refer to the endpoints of 0% and 100% steam quality, respectively.

The pressure and temperature dependent values for the density and bulk modulus of steam and water were taken from Keenan et al. (1969) and Lemmon et al. (2003). As expected, these properties differ significantly in each phase (figure 3.3). The liquid phase

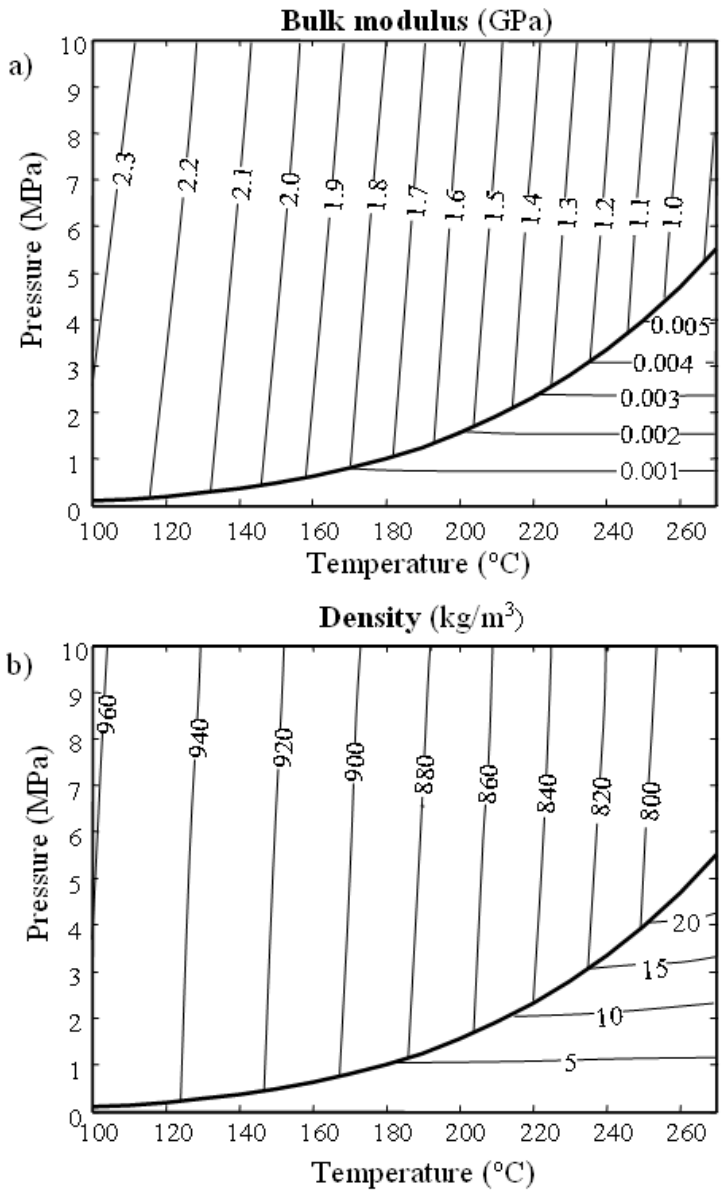

FIG. 3.3. Contour plots of the bulk modulus (top) and density (bottom) of water and steam as a function of pressure and temperature (figure from Theune, 2004).

depends strongly on temperature with only a small dependence on the pressure. Variations in the steam phase are dominantly governed by changes in pore pressure.

Fluids affect seismic velocities in several ways. Increasing the effective fluid bulk modulus increases the bulk modulus of the whole-rock system. At the same time

however, this increase is usually also associated with an increased density. Fluid bulk moduli and density both increase with pressure, but decrease with temperature. Changes in pore pressure can also cause additional complications, particularly in near surface formations. If a change in pressure is enough to cause a phase change in the fluid, then the seismic response can be large. Additionally, at a constant confining (overburden and tectonic stresses) pressure, increasing the pore pressure within a rock- fluid system decreases the effective pressure on the rock frame and lowers its frame moduli, tending to consequently lower P-wave and S-wave velocities.

If the temperature of the reservoir is increased, this will tend to lower P- and S-wave velocities of the fluids and there may a small amount be thermal expansion and/or weakening of the rock frame. Additionally, injected fluids may alter the cement within the rock framework, which may chemically weaken or strengthen the matrix. The total change in the mechanical properties of a reservoir material incorporates these competing effects.

In this paper, the change in seismic response of a reservoir subjected to different effective stress, temperature, and fluid saturation conditions is studied using Gassmann's fluid substitution (Gassmann, 1951). Relevant elastic moduli are extracted from dipole sonic and density logs, theoretical relationships (e.g. Lemmon, 2007) and empirical measurements (Mochinaga et al., 2006, Batzle and Wang, 1992, Eastwood, 1993, Wang and Nur, 1988, and Domenico, 1977).

3.3 Geology and reservoir character

The reservoir under investigation accumulated in incised valley and stacked channel complexes of an early Cretaceous age. Locally this is referred to as the

McMurray formation. The reservoir sands appear quite uniform as indicated by their well log signatures (Figure 3.4), but core analysis and other studies indicate that some portions of the reservoir can be riddled with shale stringers that are too small in thickness to be detected even by the logs. This structure is locally referred to as IHS. These are heterogeneities with low permeability, essentially invisible to typical seismic wavelengths, and they pose serious threats to the successful exploitation of large areas with SAGD.

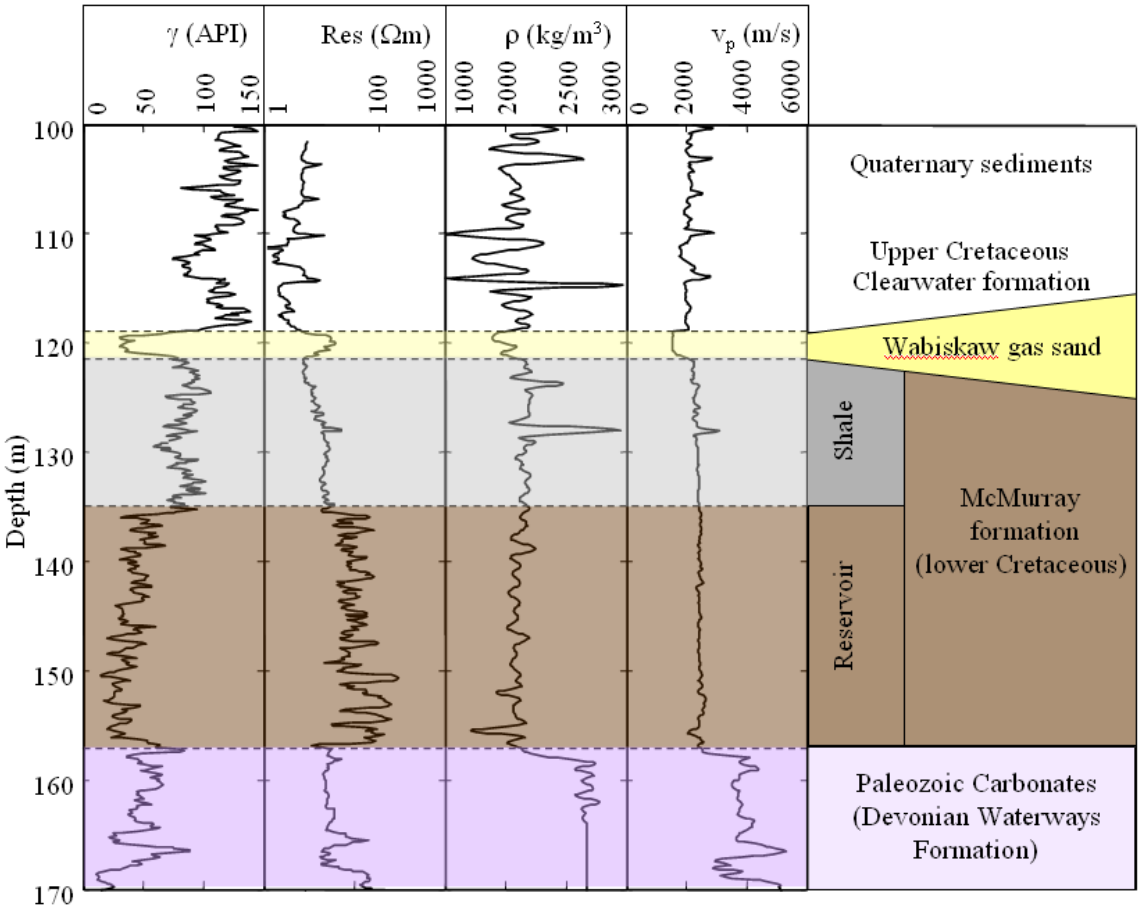

FIG. 3.4. Typical well log from the shallow part of the Athabasca reservoir.

The reservoir sands are built from mostly loose grains with only local patches being cemented by clay minerals or silica dissolution (figure 3.5). These cemented patches do not seem to be interconnected throughout the samples analyzed (personal communication, D. Rokosh). The average grain size diameter is about 0.25 mm, angular and well sorted, with an average porosity of 32%. It is commonly thought that highly viscous bitumen actually supports the sand grains in much of the material, acting as partial cement. The reservoir sands are water wet, meaning a thin film of water coats each grain and this naturally aids in the extraction and refining the oil sands.

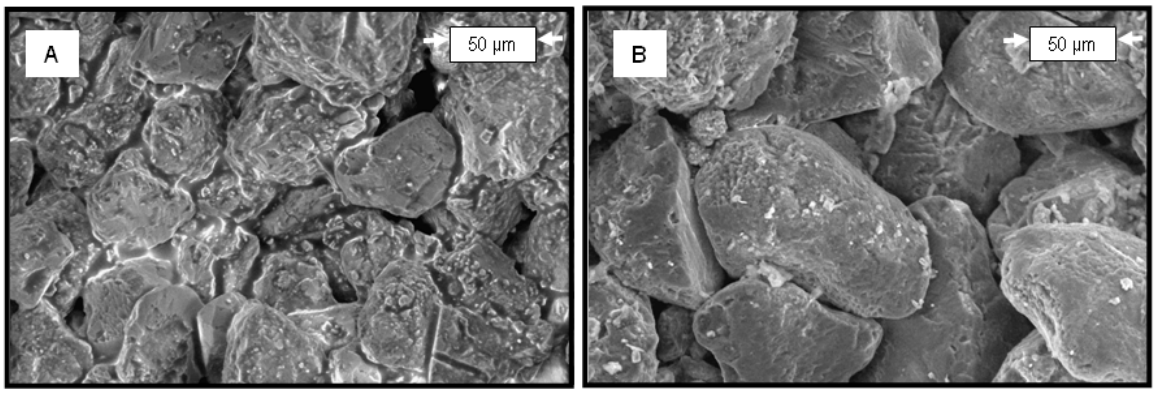

FIG. 3.5. SEM image of A) oil sands material (un-cleaned), and B) oil sands material with organic components removed (cleaned).

The reservoir sands lie immediately above a sequence of high velocity carbonates and below a thin, low velocity gas saturated sand and a shale layer. The bitumen saturation is 89%, and the viscosity of the bitumen at the natural reservoir temperature of 8ºC is ~ 7,000,000 cP (Chalaturnyk, 1996)

There is evidence that at in-situ virgin temperatures the viscous bitumen from the Athabasca oil sands will support a detectable shear wave at ultrasonic frequencies (e.g. Hornby and Murphy, 1987, and Batzle, 2006). Consequently Gassmann's formulation cannot be used to determine the elastic frame properties from the untouched zones in the

reservoir saturated with heavy oil (undepleted regions), as this theory assumes that the fluid does not exhibit resistance against shear forces (discussed below). For these regions we use pre-steam values measured from sonic logs. However, at the elevated temperatures that we consider within a typical steam chamber, the viscosity of the oils, which now flow more readily (figure 3.6), are sufficiently low that any low temperature shear effects may be ignored. In fact the substantial decrease of P-velocity up to approximately 60 ºC (Mochinaga, 2006) may indicate the partial melting of components within the bitumen at these intermediate heated regions.

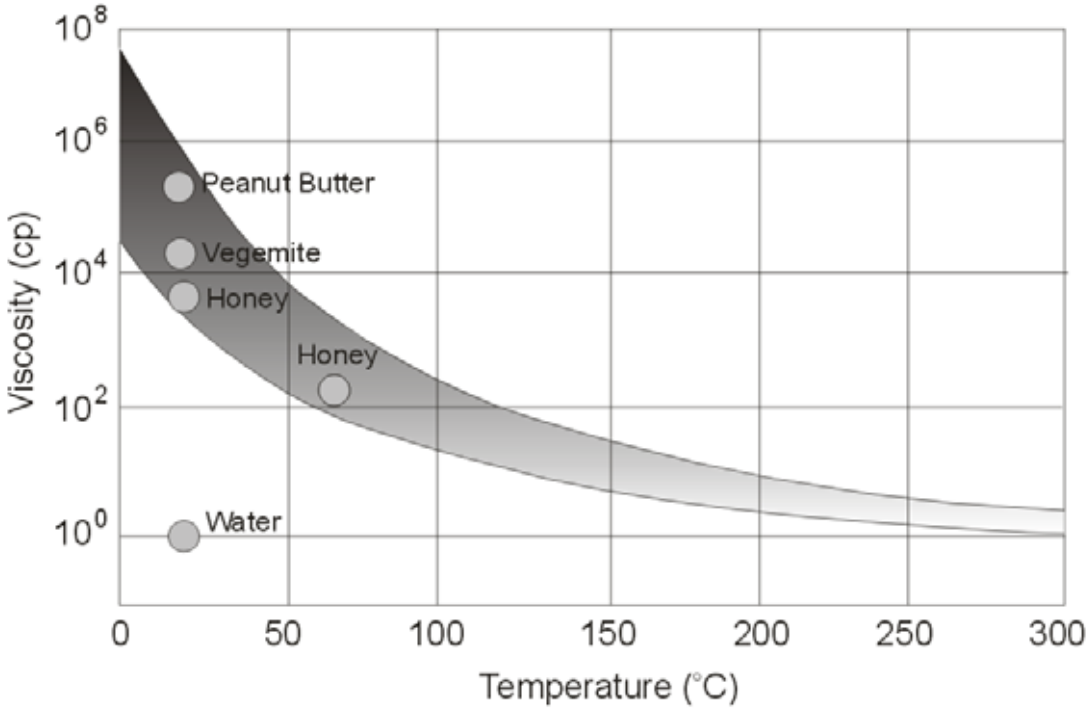

FIG. 3.6. Viscosity dependence of Alberta heavy oils and bitumens versus temperature. Ranges of viscosity values fall within the gray zone. The lower bound and upper bounds are typical of Lloydminster heavy oils and Athabasca bitumen, respectively. For comparison, the viscosities of a number of food products shown by the gray filled circles, most are given at 20ºC. Figure modified from D. Schmitt, personal documentation, 2005.

3.4 Effective pressure trends

Only the effects of temperature on the seismic properties of oil sands have been considered in much of the literature. However, pore pressure and confining stress effects are significant in such unconsolidated materials. Although engineers attempt to maintain elevated pore pressures during the SAGD processes, this is not always possible and consequently the effective pressure felt by the reservoir materials will change. It is important to understand the pressure path of a typical piece of oil sand material as it is subject to the SAGD process in order to properly characterize it. Generally, seismic velocities increase with differential effective pressure P_{eff}, which is defined as the difference between confining (or total) pressure P_c and pore pressures P_p (Terzaghi, K., and Peck, R.B., 1967, and Christensen and Wang, 1985):

$$P_{eff} = P_c - P_p . \tag{3.1}$$

Increasing effective pressure works to diminish pore cavity volumes, close crack-like porosity, and stiffen grain contacts. Within the framework of fluid substitution modeling this can be incorporated by assuming a dependence of the frame bulk modulus on the effective pressure. In order to estimate the influence of P_{eff} on the seismic velocity, we sample some of the available literature. Figure 3.7 contains a compilation of several $V_P (P_{eff})$ relationships described below:

- The curve after Eberhart-Phillips et al. (1989, whose statistical evaluations are based on the measurements by Han et al., 1986) represents an average dependence of the seismic velocity on effective pressure for a wide range of water saturated, but stiff sandstones. As the clay content is negligible in the reservoirs we used Eberhart-Phillips' et al. (1989) empirical equation to calculate the P-velocity for various pressures:

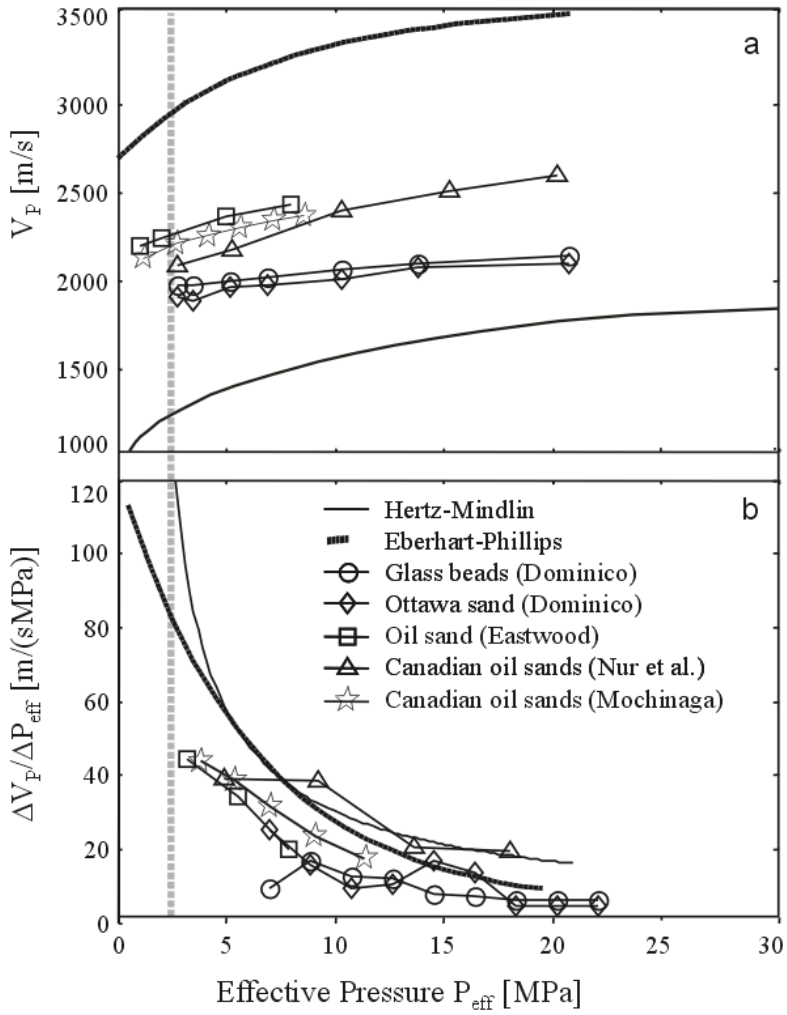

FIG. 3.7. a) Variation of the P-velocity with effective pressure. b) Velocity-Pressure gradients against effective pressure. The gray dotted line shows the pre-steam effective pressure for the Athabasca reservoir.

$$V_P = A + KP_e - Be^{-DP_e}. \tag{3.2}$$

- The empirical parameters A, K, B, and D were determined as the average value from only those samples in Eberhart-Phillips et al. (1989, their Table 1) where the porosity exceeds 27%. Thereby we eliminate the influence of the low porosity samples used by Eberhart-Phillips et al. (1989) to derive their equation 5 as such low porosity values are less representative for the reservoir we consider here. Then the average empirical values in equation (2) are as follows: A = 3.428, K = 0.407, B = 0.728, and D = 16.2. We do not consider this empirical curve as representative for our case, but it can be thought of qualitatively as an upper bound for the P-velocity of the reservoir sands for various pressures.

- Another data set is derived from the measurements by Eastwood (1993) who measured the P-wave velocity of a saturated Cold Lake oil sand for various effective pressures.
- The measurements by Domenico (1977) that compare brine-saturated glass beads with brine-saturated unconsolidated Ottawa Sands and these provide further experimental values. The average grain diameter of the Ottawa sand and glass bead specimens were 1.38×10^{-2} mm and 1.25×10^{-2} mm respectively. The measured porosity of the Ottawa sand and glass beads were identical (0.383 ± 0.005).
- The measurements of the P-velocity of heavy oil saturated sands at various pressures were taken from Nur et al. (1984) and Mochinaga et al. (2006).
- Also included in this figure is a curve representing recent modifications to the Hertz-Mindlin contact theory for dry sands after Makse et al. (1999) which is explained in detail in the next section. This theoretical curve provides a lower bound for the experimentally determined acoustic velocities in which there is no cementation between the quartz grains.

Depending on the sample used, the velocity curves in Figure 3.7a vary significantly with the curves after Eberhart-Phillips et al. (1989) and the modified Hertz-Mindlin model being used as upper and lower bounds, respectively, for the experimental data. However, more important is that all curves in Figure 3.7a show a similar dependence on the effective pressure.

The velocity-pressure gradients in Figure 3.7b have been calculated by a discrete finite difference operator. For relatively high effective pressures the changes of the measured P-velocity data and the theoretical models agree well within a relative narrow band. The different curves diverge only for lower effective pressures, thus making any predictions of the effect of pressure variations on the velocity more difficult.

The lithostatic pressure for the shallow Athabasca reservoir is estimated to be approximately 3 MPa with an effective pressure near 2.5 MPa. For such values, the change in velocity with effective pressure is much more pronounced with velocity gradients of the order of ~80 to ~300 $\mathrm{m/(s \cdot MPa)}$. Furthermore, an increase in pore pressure will cause an additional decrease in P-wave velocity effectively by jacking apart the unconsolidated grains, making seismic monitoring even more feasible for such cases.

3.5 Determination of elastic constants

The elastic properties of a composite material consisting of solid grains and a inviscid fluid is frequently described by Gassmann's (1951) equation; the bulk modulus of the effective medium, K_{eff}, is related to the bulk modulus of the solid material, K_s, the bulk modulus of the drained frame, K_d, the bulk modulus of the fluid, K_f, and the porosity φ, via

$$K_{eff} = K_d + \frac{\left(1 - K_d / K_s\right)^2}{\dfrac{1 - K_d / K_s - \phi}{K_s} + \dfrac{\phi}{K_f}} \ . \tag{3.3}$$

The frame bulk modulus K_d describes the rigidity of the interconnected matrix of mineral grains. Its value is relatively high for well consolidated, compacted, and cemented sediments, making the rock seismically fast. On the other hand, K_d can be smaller than the fluid bulk modulus, K_f, for unconsolidated, fragile sands, and as such, the seismic velocities are slow compared to more competent rocks.

Further, according to Gassmann's theory, the shear modulus of the effective medium, μ_{eff}, is solely determined by the shear properties of the frame, μ_d,

$$\mu_{eff} = \mu_d \ . \tag{3.4}$$

Several published measurements on unconsolidated sands report some measurements of the bulk to the shear frame modulus, and the ratio of these two moduli. Hornby and Murphy (1987) observed a wide scattering of this ratio for different porosities. Conversely, Murphy et al. (1993) derived an empirical relationship for this ratio suggesting that both frame moduli depend linearly on each other. Additionally, these researchers suggest that above a critical porosity the elastic frame properties also depend linearly on the mineral grain moduli. The static analysis of unconsolidated materials by Spencer et al. (1994) reveals that the frame properties vary significantly. They did not measure the bulk and shear frame modulus directly but determined the Young's modulus and Poisson's ratio of the samples, which depended only weakly on the properties of the solid mineral grains. Additionally, Bachrach et al. (2004) have shown that measured values of Poisson's ratio from an uncemented, dense, random pack of identical beads are constant for all effective pressures. They also show measurements of V_P and V_S that are both smaller than Hertz-Mindlin prediction for effective pressures less than 10 MPa. This literature survey shows that the experimental results of the frame properties are in a sense contradictory; at this time no simple rule can be applied to relate the frame properties to, for example, porosity and mineralogy. In unconsolidated materials the elastic frame properties most likely depend on the nature of the grain contacts (Murphy et al., 1986; Murphy et al., 1993). For example, the roughness of the grain surfaces and hence its friction against adjacent grains will certainly influence the stiffness of the frame. Since no clear basis for predicting the frame modulus in such unconsolidated materials exists, workers instead rely on direct laboratory or well-log measurements of effective moduli to obtain representative values.

Here we assume that Gassmann's equation applies in order to determine the elastic properties of the formation from V_P - sonic, V_s - sonic and density logs. Aside from the frame bulk modulus, K_d, all the other moduli are either relatively easily measured or are already available in the literature (e.g., Mavko et al., 1998). A value for the frame bulk modulus K_d can in principle be determined from well log data under that assumption that such data represents the low frequency limit by rearranging Gassmann's equation:

$$\mathrm{K_d} = \frac{1 + \mathrm{K_{eff}}\left((\phi - 1)/\mathrm{K_s} - \phi/\mathrm{K_f}\right)}{\dfrac{1 - \mathrm{K_{eff}}/\mathrm{K_s} + \phi}{\mathrm{K_s}} - \dfrac{\phi}{\mathrm{K_f}}}, \tag{3.5}$$

where the effective bulk modulus K_{eff} is calculated directly using sonic and density log data according to

$$\mathrm{K_{eff}} = \rho\left(\mathrm{V_P^2} - \frac{4}{3}\mathrm{V_S^2}\right). \tag{3.6}$$

We use a Reuss average to find an effective fluid bulk modulus K_f. This approach assumes a homogeneous distribution of the three phases within the pore space, with the pore volume fraction of oil, steam and water is indicated by S_o, S_s, S_w, respectively:

$$\frac{1}{\mathrm{K_f}(P,T)} = \frac{\mathrm{S_O}}{\mathrm{K_O}(P,T)} + \frac{\mathrm{S_S}}{\mathrm{K_S}(P,T)} + \frac{\mathrm{S_W}}{\mathrm{K_W}(P,T)}, \tag{3.7}$$

where $K_{O,}$ $K_{S,}$ and K_W are the pressure and temperature dependent bulk moduli of the oil, steam, and water phase, respectively. This equation can be used to calculate any number of saturation combinations of these three fluids. We extract empirical values presented by Batzle and Wang (1992) for the bulk moduli of oil, and we use figure 3 for the relevant moduli for water and steam. A table of all relevant values is located at the end of this section.

The shear modulus of the solid frame μ_d, is similarly calculated from the shear sonic and density logs:

$$\mu_d = \rho V_s^2 . \tag{3.8}$$

Figure 3.8 illustrates a color-contoured surface representing K_d as a function of K_{eff} and K_f only (i.e. porosity φ, is held constant at 32% and K_s is held constant at 36 GPa in equation 3.3). This graph is useful because it casts the unknown variable, K_d, in terms of two more accessible measurements. In order to constrain the acceptable values of K_d for the virgin reservoir conditions (undepleted case), we simply mark the region of the graph subject to the observed values of the K_{eff} and K_f. The fluid bulk modulus is

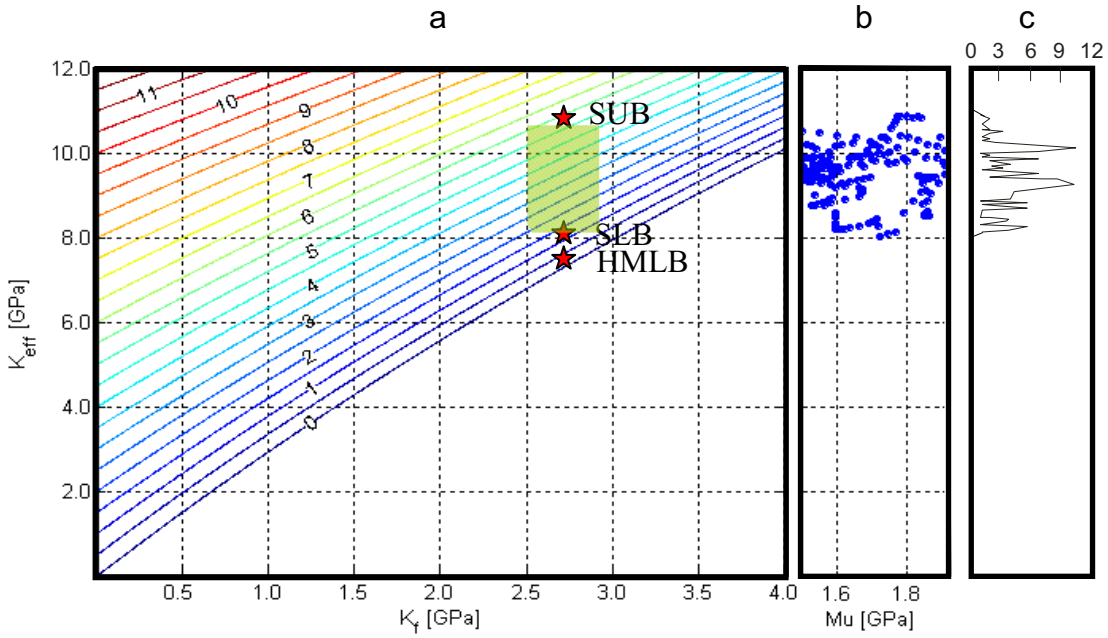

FIG. 3.8. a) Colored contoured surface of K_d expressed as a function of K_{eff} and K_f as described by equation 3.5. The sonic-log-derived upper bound 'SUB', and lower bound 'SLB', indicate the range of data points determined from borehole dipole sonic log measurements. The bounds come from the high and low V_P values. b) Scatter plot of K_{eff} vs. μ_{eff} for oil sands, and c) histogram depicting the spread of K_{eff} values found within the borehole. The Hertz-Mindlin lower bound (HMLB) was determined from equations 9 and 11. The curve $K_d = 0$ corresponds to Wood's formula; a fluid saturated suspension of grain particles.

constrained to 2.64 ± 0.23 GPa, (89% oil at 2.7 ± 0.1 GPa and 11% water at 2.28 ± 0.12 GPa) however the estimate for the effective bulk modulus has greater uncertainty due to significant scatter in the well logs. We find that pre-steam oil sand K_{eff} values lie in the range 8.0 -10.5 GPa. We note that acceptable values of K_{eff} may take on a range of values reflective of lithologic variability or it may be due to small errors in the log measurements. For instance, particularly low values of K_{eff} may have been recorded in positions of borehole washout or extreme mud-cake. The green box in figure 3.8 corresponds to K_d values in the range of 1.5 to 5.5 GPa. Note that if the measured values of K_{eff} were actually less than 7.7 GPa then the calculated dry frame moduli would become negative, which is physically nontenable. The lowest value of acceptable values of K_{eff} corresponds to the case where the sand is in complete suspension in fluid.

We can place a lower bound on acceptable values of K_d by considering a heuristic modification of Hertz-Mindlin contact theory for uncemented spherical grains. The uncemented sand model is used to calculate the bulk and shear moduli of dry sand in which cement is deposited away from grain contacts (Maske et al., 1999):

$$K_{HM} = \left[\frac{C^2 (1-\phi_0)^2 \mu_s{}^2}{18\pi^2 (1-v)^2} P_{eff} \right]^{1/3}, \tag{3.9}$$

$$\mu_{HM} = \frac{5-4v}{5(2-v)} \left[\frac{3C^2 (1-\phi_0)^2 \mu_s{}^2}{2\pi^2 (1-v)^2} P_{eff} \right]^{1/3}, \tag{3.10}$$

where C=9, is the average number of neighboring grain contacts per grain, v is Poission's ratio, μ_s is the mineral shear modulus, and φ_0 is a reference porosity equal to 36%. To find the effective moduli at a different porosity φ, the heuristically adapted Hashin-Strikman lower bound is used:

$$K'_{d\_lower} = \left[\frac{\phi/\phi_0}{K_{HM} + \frac{4}{3}\mu_{HM}} + \frac{1-\phi/\phi_0}{K_s + \frac{4}{3}\mu_{HM}} \right]^{-1} - \frac{4}{3}\mu_{HM}\,, \tag{3.11}$$

$$\mu'_{d\_lower} = \left[\frac{\phi/\phi_0}{\mu_{HM} + \frac{\mu_{HM}}{6}\left(\frac{9K_{HM} + 8\mu_{HM}}{K_{HM} + 2\mu_{HM}} \right)} + \frac{1-\phi/\phi_0}{\mu_{HM} + \frac{\mu_{HM}}{6}\left(\frac{9K_{HM} + 8\mu_{HM}}{K_{HM} + 2\mu_{HM}} \right)} \right]^{-1}$$
$$- \frac{\mu_{HM}}{6}\left(\frac{9K_{HM} + 8\mu_{HM}}{K_{HM} + 2\mu_{HM}} \right) \tag{3.12}$$

K_{eff}' and μ_{eff}' can be thought of as a theoretical lower bound for the frame bulk modulus and effective shear moduli of our reservoir material. Additionally, the cubic root dependency on effective pressure from equations (3.9) and (3.10) allow the pressure effect on oil sands moduli to be explored. Figure 3.9 shows the relationship between frame bulk modulus and effective pressure of uncemented spherical sediments for a range of porosities. The trend shows that pore pressure has a significant influence on the frame properties.

To finally calculate seismic velocities from the elastic constants we require the density μ_{eff}, which is obtained from volumetric averaging:

$$\rho_{\text{eff}} = (1-\phi)\rho_{\text{s}} + \phi\rho_{\text{f}}\ , \tag{3.13}$$

where the density of the fluid phase is given by

$$\rho_{\text{f}} = \text{S}_{\text{O}}\rho_{\text{O}} + \text{S}_{\text{W}}\rho_{\text{W}} + \text{S}_{\text{S}}\rho_{\text{S}}\,. \tag{3.14}$$

Mochinaga (2006) measured the density and bulk modulus of bitumen only over the temperature range between 0°C and 120°C, but extrapolations to 300°C can be made on the basis of Batzle and Wang's (1992) observation that, as long as the fluid's conditions are not near any phase boundaries, a linear relationship between density and bulk modulus with temperature works well. The properties of the Athabasca oil were

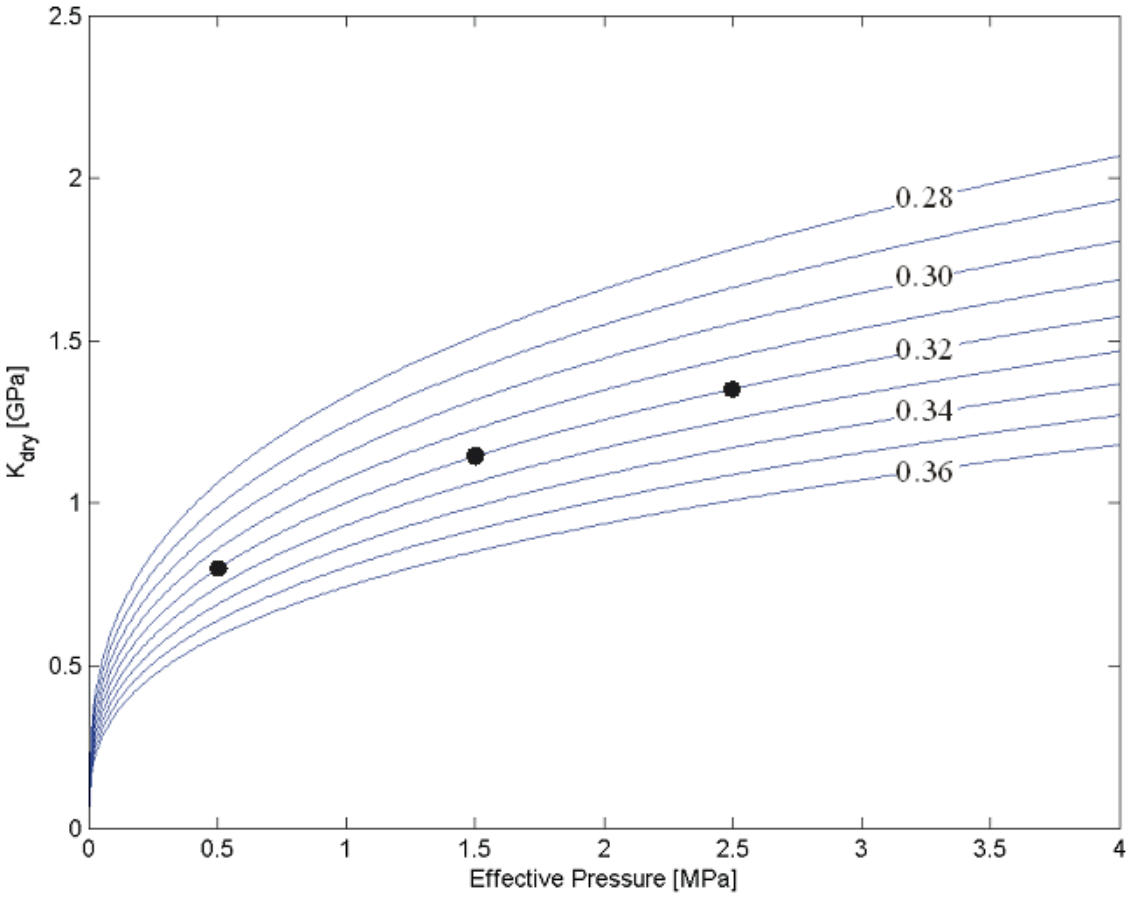

FIG. 3.9. Dry frame bulk modulus as a function of effective pressure for 9 values of porosity representing a range of unconsolidated sediments. The curves were calculated based on the heuristically modified Hashin-Strikman lower bound of the Hertz-Mindlin contact model for uncemented mineral grains (Dvorkin and Nur, 1996) as shown in equations 3.9-12. The dots indicate the effective pressure conditions that we explicitly evaluate for this reservoir.

calculated using Batzle and Wang's (1992) empirical equations 18, 19, and 20a with a value of 998 kg/m^3 for the reference density ρ_o. For the high temperatures considered here, these values fall within 5% of each other.

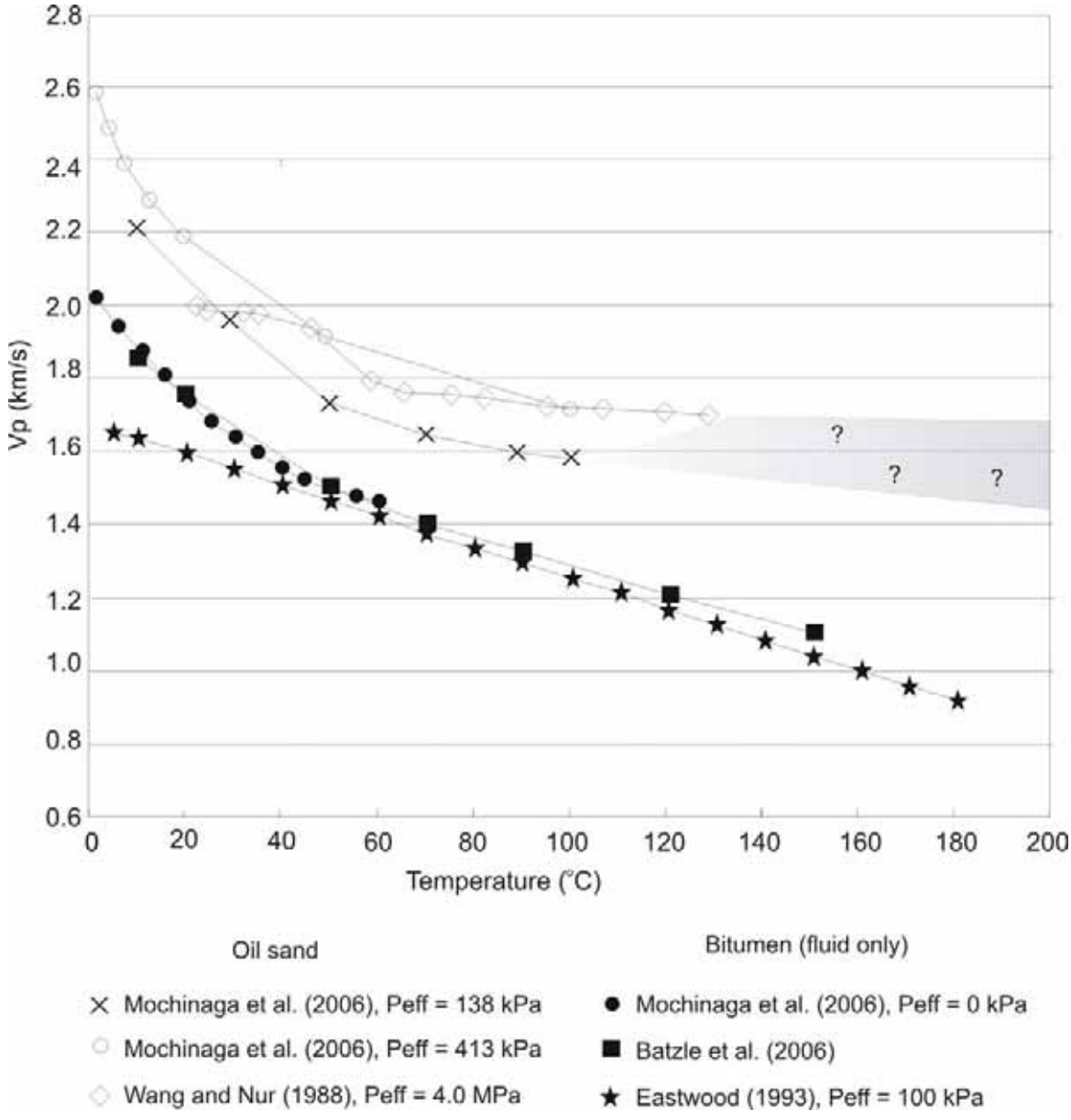

FIG. 3.10. Temperature dependence of V_P on bituminous oil and oil sands.

3.6 Fluid Substitution

Many studies have focused on velocity decreases due to heating of heavy oil saturated reservoirs, but the SAGD steam injection case considered here is substantially more complicated. The effective pore fluid after steam injection will surely be an immiscible mixture of high temperature residual hydrocarbons, water in liquid and gas phases, which may have a complicated distribution within the pore space of the rock. Various gases, most notably methane, may be present as well, as they will exsolve if the bubble point is reached at sufficiently high temperatures or if the reservoir pore pressure decreases.

The acoustic velocity for a two-phase single component mixture such as water and steam can yield extreme results. Kieffer (1977) calculated that the sound speed in a water-steam (i.e. liquid-gas) mixture is significantly lower than that of either phase alone. Furthermore, for such a single-component, two-phase system the velocity depends on whether or not the compression by a passing seismic wave allows for thermodynamic equilibrium between the two phases. For very low frequencies of the seismic wave there can be sufficient time to establish a thermal equilibrium of the two phases. In this case, the resulting isothermal velocity could be as low as 1 m/s. However, to our knowledge, a criterion for the upper limit of the frequency for this process to occur is not known. In our analysis we assume that the effective velocity is an adiabatic process as the frequencies used in seismic exploration are relatively high.

For the fluid substitution we assume a simple mixture of oil, water, and steam at elevated temperature, at such temperatures we assume that the heavy oil has lost any potential for finite shear rigidity; and therefore, Gassmann's theory can be applied for the

high temperature case. As we only poorly understand the distribution of the fluids in the pore space we assume simple homogeneous distribution of the three fluid components. A more advanced approach would assume a patchy saturation (Mavko and Mukerji, 1998), which allows for a heterogeneous distribution of three or more phases. This usually yields lower velocities relative to Gassmann's theory, but since we cannot predict saturation patterns distributions, we do not consider it here.

3.7 Ternary Diagrams

The properties of the 3 fluids under investigation vary with temperature and pressure. To study the influence of the steam injection on the seismic properties we calculated the effective velocity of a generalized reservoir with varying elastic frame properties and pore fluid composition. Figure 3.3 suggests that the temperature and pore pressure within a steam chamber is coupled along a saturation profile and we assume, in this environment, that temperature and pressure are not independent variables. For instance, if the temperature of the heated reservoir is 200°C then steam must necessarily be injected at (or above) 1.5 MPa of else it will immediately condense into liquid water. This ensures that the pore pressure within the depleted region of reservoir (the area that has been touched by steam) is also at 1.5 MPa.

In order to illustrate the calculated P-velocity as a function of saturation, ternary diagrams are used. Each point on a ternary diagram represents the partition of a 3-phase mixture. In our case, we plot the saturations of the three pore fluid constituents (oil, water, steam) on each axis of the ternary diagram. For example, the diamond in figure 3.11 indicates a fluid which has 50% oil, 20% steam, and 30% water. For subsequent

ternary diagrams, this axes setup will be used, and the annotation on the figures is omitted to avoid clutter.

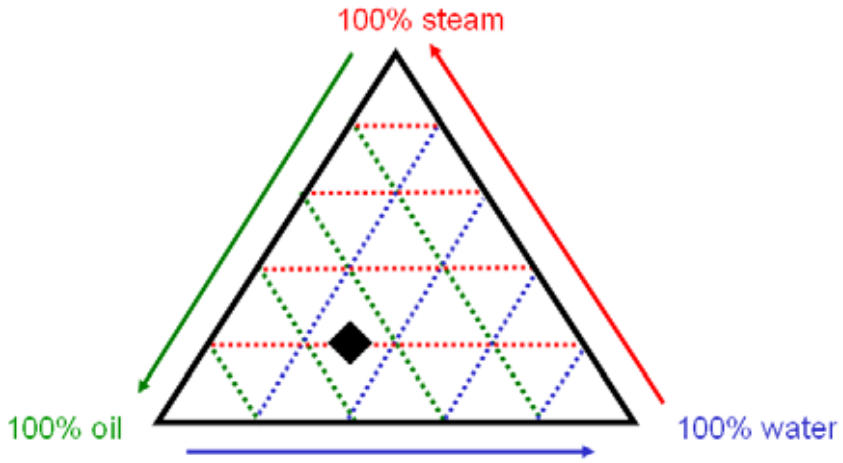

FIG. 3.11. Schematic of a ternary diagram which can be used to plot all possible combinations of a 3-component fluid mixture. The black diamond corresponds to a saturation of 30% water, 20% steam, 50% oil.

Ideally, injection creates a steam chamber filled with a high quality steam; however, a residual amount of oil will remain in the depleted reservoir. For the Athabasca reservoir, we assume the following conditions:

- The initial oil saturation is 89% and the remaining 11% of the pore space is filled with water. The temperature is 8 °C, pore pressure is 0.5 MPa, and porosity is 32% (Chalaturnyk, 1996).
- After steam injection, a mixture of 62% oil, 15% water, and 23% steam fills the pore space in the steam chamber. The increase in water saturation is because we assume 85% steam quality, and the reduction in oil saturation represents a recovery factor of 30% of the oil in place. The coupled temperature / pore pressure conditions within the steam chamber are varied for three different cases 150 °C / 0.5 MPa, 200 °C / 2.0

MPa, and 220 °C / 2.5 MPa, respectively. All the relevant information used in the fluid substitution is summarized in table 3.1.

The elastic frame properties are varied from 3.4 GPa ≤ K_d ≤ 3.6 GPa corresponding to the average value defined by the bounds in figure 3.7. Figure 3.12 and 3.13 cast the calculations into ternary diagrams in order to illustrate the sensitivity of pore fluid composition on P-velocity after fluid substitution. In figure 3.11, we assume that there is no pore pressure induced variations on the frame modulus K_d; velocity variations are a result of fluid substitution only. In figure 3.13, the velocity variations are a result of both fluid substitution and pore pressure induced rock frame 'softening' as described by the theoretical contact model in figure 3.9. Obviously, there has been no ternary diagram constructed for the undepleted reservoir as Gassman's equation cannot be used for low temperatures; where the pore filling materials have finite shear strength.

These ternary diagrams suggest several relationship and we can make many observations. The change in the P-velocity is found to vary from ~-200 m/s to over -1100 m/s (from an pre-steam sonic measured value of 2200 m/s) depending of the frame moduli of the reservoir and the temperature / pressure of the injected steam. The stiffer the elastic frame the smaller the decrease of the P-velocity. After injecting only a few percent of steam into the pore space the bulk modulus of the fluid mixture decreases substantially but increases only marginally with further steam saturation, especially for small values of the frame bulk modulus. This is representative of the harmonic sum of the fluid modulus (equation 3.6). Also can be seen is that the effects of fluid substitution alone (figure 3.12) are not as strong when fluids are injected at low high pore pressure / temperatures. Referring to the fluid bulk moduli in table 3.1, the difference in the changes of the

velocity for the low (150°C) and high (220°C) temperature case can be explained. by analyzing the effective fluid bulk modulus (equation 3.6). The bulk modulus of steam at 150°C is a factor 3 smaller than at 220°C along the phase transition line, and either value for steam is significantly smaller than both values for liquid water and oil. Conversely, the density of steam at 150°C is a factor of 4 smaller than at 220°C along the phase transition line, which is why, in the absence of a changing frame bulk modulus, the velocities increase actually increase slightly. As the steam density at low temperatures is much smaller, the changes in the velocity according to the Gassmann model are larger than at high temperatures.

In all models shown here, the effective fluid bulk modulus of the steam-water-oil mixture is substantially lower than that of the original oil-water saturation; and the effective bulk modulus approaches that of the dry frame. A patchy saturation model would estimate generally higher velocities, and choose not to incorporate it into these ternary diagrams. Regardless of the model employed, it suffices to say that the overall change due to fluid substitution in the Athabasca reservoir is large. The next section shows a 2D seismic model that assumes the steam is injected at 1.5 MPa / 200ºC and has a K_d = 2.97 GPa. This corresponds to effective velocity with the steam chamber that is

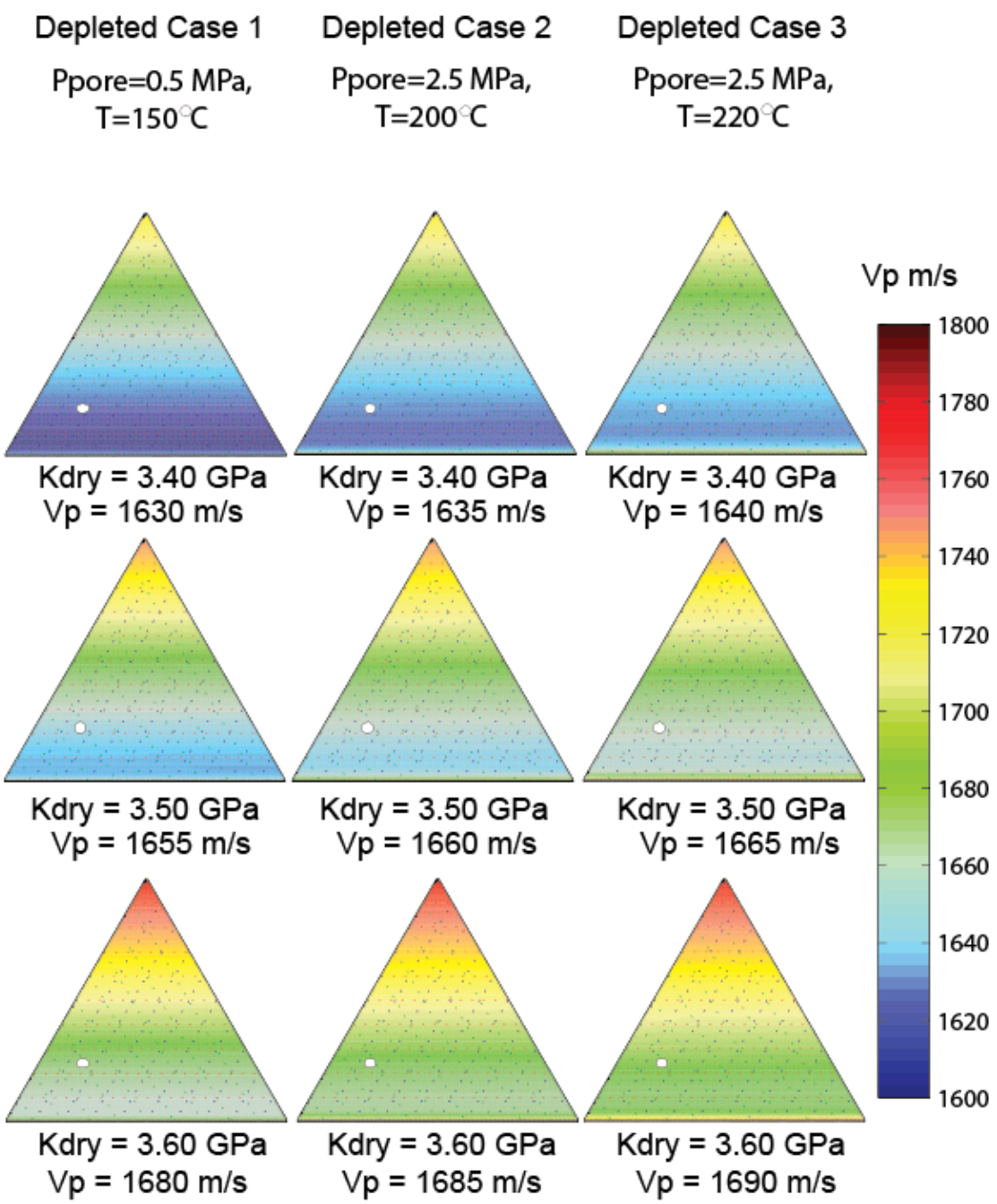

FIG. 3.12. Ternary diagrams for the oil-water-steam reservoir system with K_d = 3.40 GPa (first row), K_d = 3.50 GPa (second row), K_d = 3.60 GPa (third row), for three different reservoir depletion scenarios (columns). In these plots, we assume that there is no pore pressure induced variation on K_d; velocity variations are a result of fluid substitution only. The fluid saturation within typical a SAGD chamber (62% oil, 15% water, 23% steam) is indicated by the white circles.

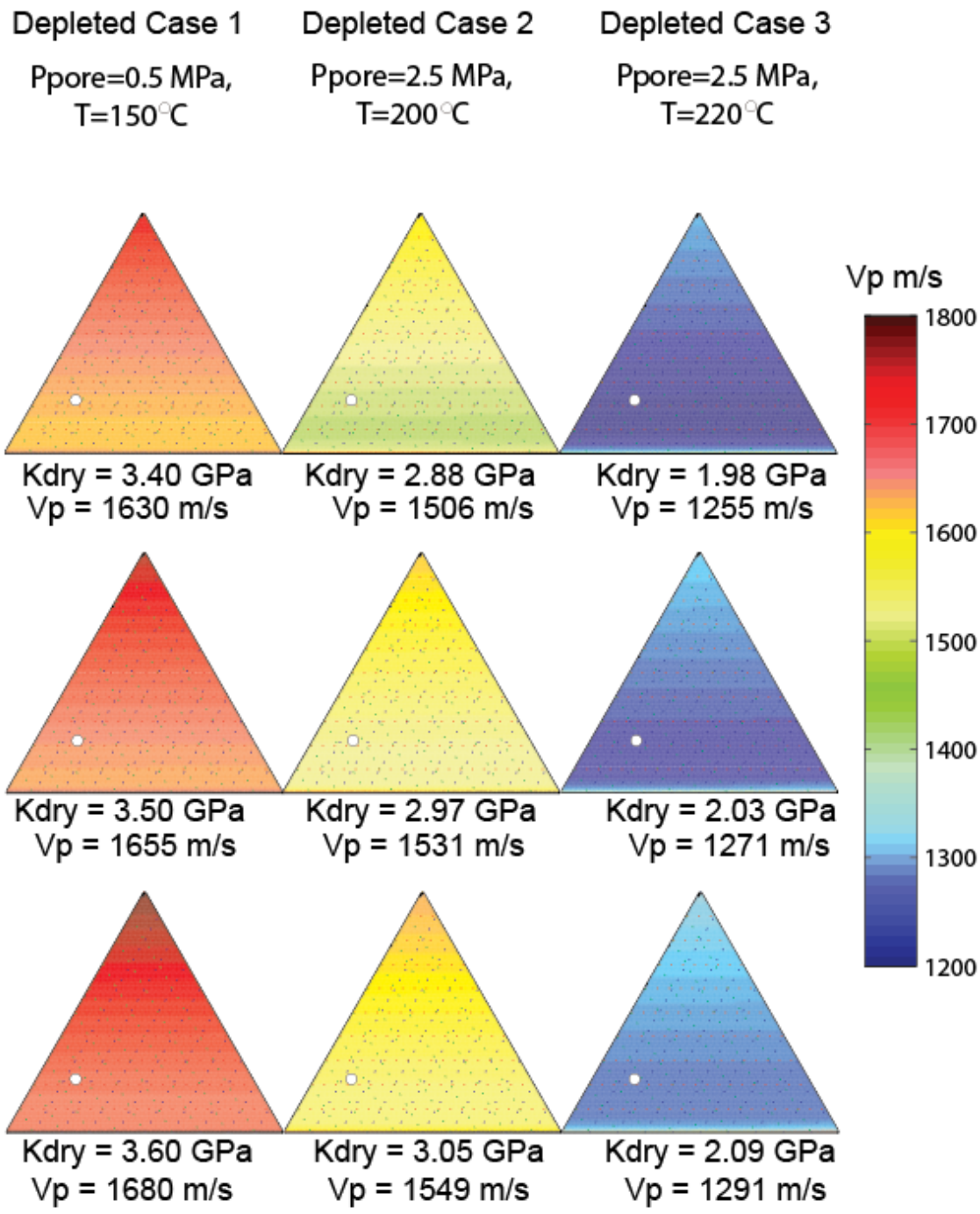

FIG. 3.13. Ternary diagrams for the oil-water-steam reservoir system with K_d = 3.40 GPa (first row), K_d = 3.50 GPa (second row), K_d = 3.60 GPa (third row), for three different reservoir depletion scenarios (columns). In the calculations displayed here, variations in K_d are estimated based on increased fluid pressure, via the relationship shown in figure 3.7. The velocity variations are a result of both fluid substitution and pore pressure induced rock frame 'softening'. The fluid saturation within typical SAGD chamber (62% oil, 15% water, 23% steam) is indicated by the white circles. Note how increasing fluid injection temperatures and pressures (moving from column 1 to column 3) has a large effect on the frame and velocities drop dramatically.

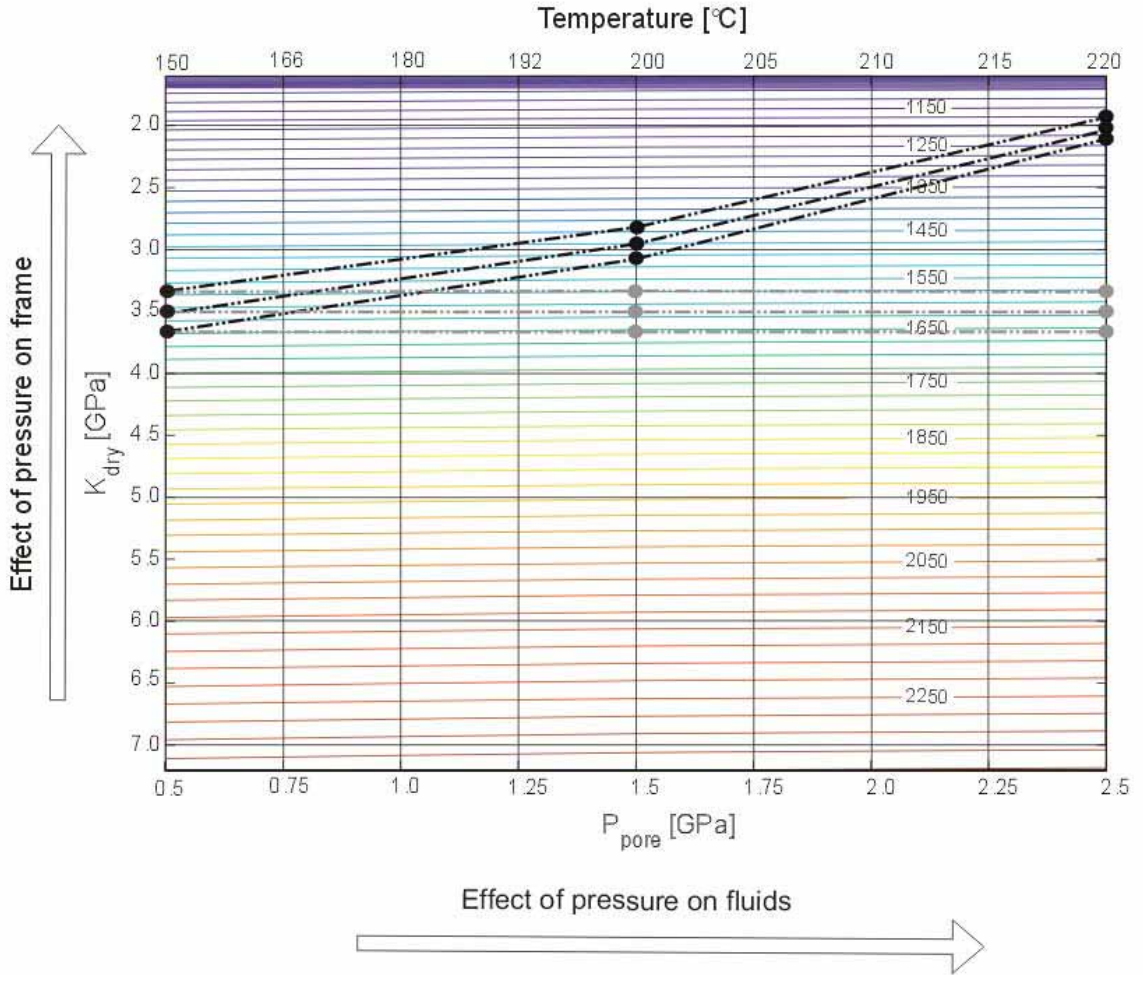

FIG. 3.14. Contour plot of V_{Peff} for a range of pressures affecting the fluids (horizontal axis) and the rock frame (vertical axis) within a model steam zone. Contour labels have units of velocity (m/s). V_{Peff} is calculated with the saturation held constant (at 62% oil, 15% water, and 23% steam invoked by the SAGD process). The gray circles indicate the velocity path a material would experience if its frame were not affected by pore pressure, and the gray dots indicate the velocity path a material would experience if the rock frame does change due in response to changes in pore pressure (i.e. changes in the effective confining stress). The black and gray dots indicate the pore-pressure, temperature, and frame values explicitly illustrated in ternary diagrams in figures 11 and 12.

Figure 3.15A shows a temperature profile of a typical steam chamber contoured from borehole thermocouple measurements. Figure 3.15B shows the computed velocity model obtained from mapping the results of the figure 3.9 onto this temperature profile.

We choose the values from K_d =2.97 GPA at 1.5MPa / 200ºC as it is the mean value.

This corresponds to the ternary plot in the middle of figure 12. There are two distinct

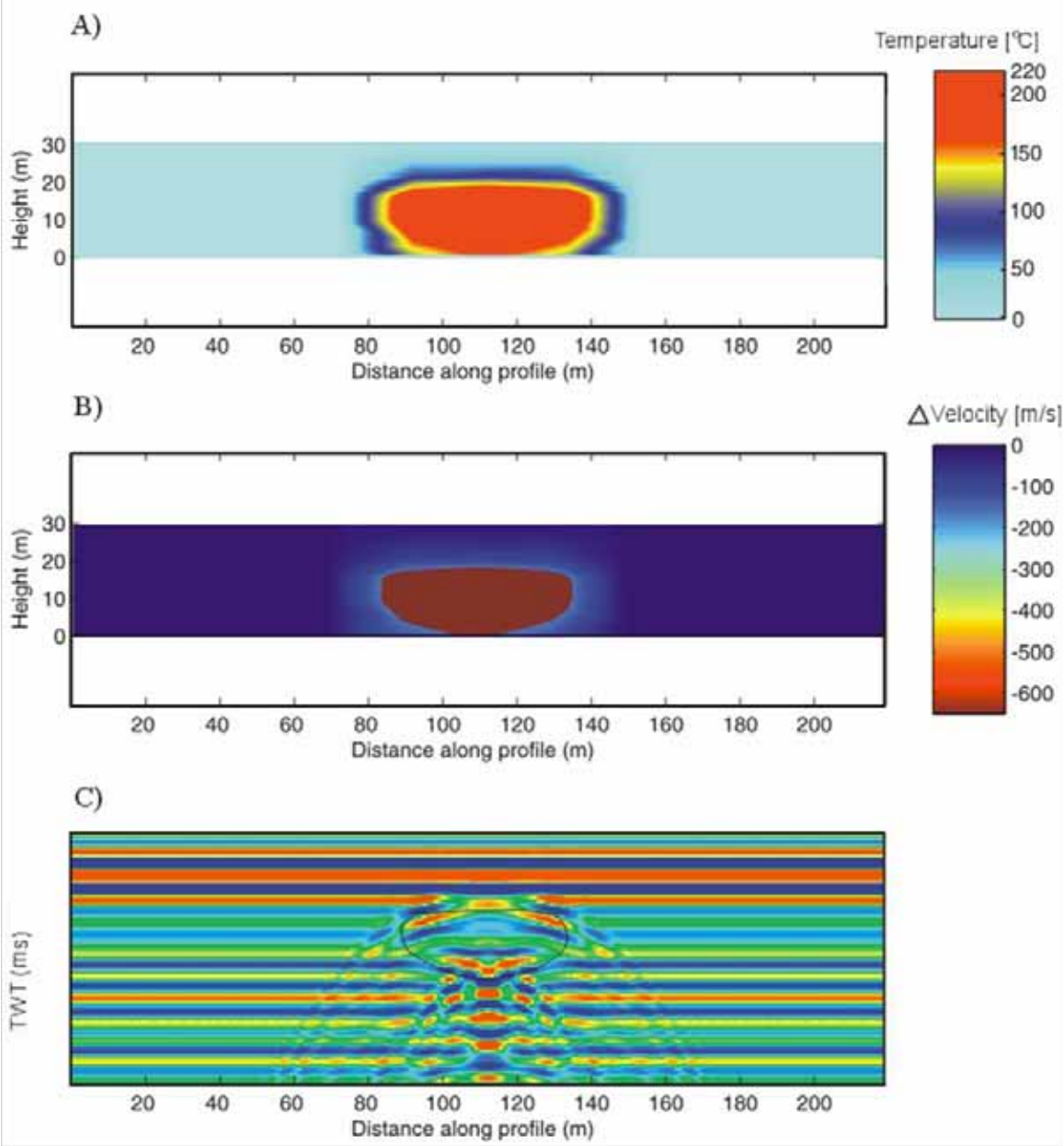

FIG. 3.15. A) Hypothetical temperature profile of a typical steam chamber in Athabasca reservoir B) Computed P-wave velocity anomaly result from rock physics and fluid substitution analysis. C) Un-migrated synthetic seismic profile generated using an acoustic finite difference algorithm. The steam anomaly in B) is superimposed on the background reflectivity determined by closely spaced well logs at the UTF. The offset range used in this stacked section is 48 -142 m.

velocity regions due to the steam chamber. The steam zone itself produces an extreme low velocity anomaly governed by convection, increased pore pressure and fluid substitution. The velocities at the periphery of the steam zone are altered by heat conduction radiating away from the steam chamber, with an area of modest velocity decrease governed by the empirical values of a heated oil sands sample by Mochinaga et al. (2006). For simplification, the periphery of the steam zone is considered to only be affected by a change in temperature (heating of the oil), however the increased pore pressures inside the steam chamber are likely to exhibit shearing strains within the heated zone. The adoption of a pressure-dependant strain gradient profile would more accurately describe the mechanical behavior of the regions just outside the steam zone.

3.8 Seismic attribute analysis

The changes of the velocities and densities of the reservoir zone upon fluid substitution must influence the propagation of the seismic wave field. In this section we examine the changes anticipated in the acoustic response. Although considering the full visco-elastic behavior of wave propagation would definitely be more complete, there is, at this time, inadequate information to address the problem. The analysis of viscosity related dispersion attributes such as seismic waveform distortion are currently not possible due to insufficient information on the physical properties of the bituminous oils. The change in the normal incidence reflectivity at the top of the reservoir, ΔR, and the change in travel time to the bottom of the reservoir, ΔT, are also difficult to measure from waveforms because there is complicated tuning and interference taking place.

To explain the propagation of seismic energy through an oil-depleted steam chamber surrounded by cold, untouched, virgin reservoir, a finite difference algorithm

was employed to calculate the wavefield generated through the acoustic velocity model shown in figure 3.15.B.

Figure 3.15.C shows a seismic profile generated using a finite difference algorithm showing the seismic foot print of the steam anomaly interfering with the background reflectivity structure. The anomaly produced by the steam zone yields an increase in amplitude and large time delay beneath the reservoir, but this example also presents symptoms of a scattering feature. The wave field reverberates and includes diffraction hyperbolae, complicated reverberations and multiple reflections from within the steam zone. The perturbation in the wave field is localized about the steam zone and it appears that internal multiples persist beneath the thickest part of the steam zone (~108 m to ~118 m along the profile in figure 3.15.C). Depending on resolution limits of the seismic data, this may be difficult to detect, let alone outright image, if, the shot and receiver spacing is too sparse. Such modeling of relatively small scale features such as steam chambers can aid in long term survey planning and optimizing monitoring programs. The substantial changes in the seismic signal suggest that seismic monitoring of SAGD at the Athabasca reservoir should be feasible when the subsurface is sufficiently sampled. This result is in agreement with the strong signals observed by Schmitt (1999) where 1 m CMP spacing (admittedly ultra-high spatial resolution) allows for adequate sampling of this steam chamber system even with a relatively low center frequency (<40Hz) probing the reservoir.

3.9 Discussion - Pressure induced shearing and permeability

One of the important parameters in assessing the feasibility of seismic monitoring is the frame bulk modulus K_d. The values used in this study were obtained using well

logs. For this reservoir we used the inverted Gassmann equation (5) to determine the elastic frame properties from density and sonic logs. We note that the value of K_d determined from sonic logs can be larger than for seismic frequencies due to dispersion effects. Such effects are typically on the order of 5 % and as such have been ignored, as this will not substantially change our results.

Due to the lack of velocity data measured at different effective pressures we can only extrapolate the effects due to pore pressure changes on K_d based on the Hertz-Mindlin contact theory. Increasing pore pressures in these unconsolidated materials cause the velocities to decrease significantly. However, we consider these results rather preliminary as the range for the velocity variations on pressure used here is not yet well constrained.

When steam is injected, reservoir temperatures and pressures are raised. These elevated temperatures and pressures reduce the bitumen's viscosity and change the rock stresses enough to cause shear failure within and beyond the growing steam chamber. Once individual sand grains are shifted and rotated, there is an increase in bulk volume caused by an increase in porosity. The associated increase in absolute permeability can be a factor of 10 (Collins, 2007). The term absolute permeability is actually a misnomer because the "absolute" permeability of an oil sand is bound to increase with shearing and disturbance of the grains. What is important is not the original permeability that exists, but how much permeability is required, and how much pressure and temperature is required to obtain it.

The dislocation of sand grains and mechanical enhancement of permeability is desired for the SAGD process given that analytical models show that the rate of

production is proportional to the square root of permeability (Butler, 1997). Therefore, increasing permeability by a factor of 10 should increase production rate by a factor of 3. Typically, however, the optimal injection pressure for maximizing permeability is higher than pressures being currently implemented by many operators (Collins, 2007). Low-pressure SAGD (LPSAGD) has been preferred because higher injection pressures and temperatures invoke additional costs and challenges. The supporting argument for LPSAGD is that a low pressure steam carries a larger percentage of latent heat than high pressure; however, LPSAGD misses all the advantageous geomechanical disturbances that high pressures induce. It presumes that permeability is independent of injection pressure.

3.10 Conclusions

In the past the feasibility of seismic monitoring for thermally enhanced oil recovery has been based on the substantial decrease of an oil saturated sample's P-velocity when heated. Such a scenario does not fully represent the SAGD process where oil is not only heated but also replaced by steam and water at elevated pressures and temperatures. This invasive fluid actually shears the material and frees the viscous bitumen cement that holds the sand grains together. The rock physical modeling presented in this paper tries incorporate all of these effects. Therefore, this approach, carried out for the first time to simulate the rock physical impact by a SAGD program, should more accurately represent the real situation. The largest seismic response will occur when the frame bulk modulus is sufficiently small and, secondly, when high pressure steam is injected to shear and deform oil sands in the reservoir.

To assess the feasibility of seismic monitoring we have qualitatively analyzed seismic attributes generated from an acoustic finite difference algorithm, but the full results will be explored in the next chapter. The tuned synthetic seismograms, which more accurately represent the physics of wave propagation, present a more complex footprint than seen with traditional 1-D modeling

	Undepleted	**Depleted: Case 1** low pore pressure	**Depleted: Case 2** mid pore pressure	**Depleted: Case 3** high pore pressure
T [ºC]	8	150	200	220
P confining [MPa]	3			
P pore [MPa]	0.5	0.5	1.5	2.5
P effective [MPa]	**2.5**	**2.5**	**1.5**	**0.5**
K dry [GPa]	3.40 - 3.60†	3.40 - 3.60	2.88 - 3.6	1.98 - 3.6
μ dry [GPa]	1.48 - 1.52†	1.48 - 1.52	1.25 - 1.52	0.91 - 1.52
K solid [GPa]	36			
μ solid [GPa]	45			
ρ solid [kg/m3]	2650			
φ [%]	32			
K oil [GPa]	2.70	1.20	0.75	0.65
K water [GPa]	2.28	1.95	1.50	1.35
K steam [GPa]	0.002	0.001	0.002	0.003
ρ oil [kg/m3]	1020	910	860	827
ρ water [kg/m3]	1000	915	870	835
ρ steam [kg/m3]	2	3	10	12
S oil [%]	89	62*	62*	62*
S water [%]	11	15**	15**	15**
S steam [%]	0	23**	23**	23**

† Determined from borehole measurements

* represents 30% recovery

** represents 30% recovery

Table 3.1. Relevant parameters used for fluid substitution.

References

Bachrach, R., Dvorkin, J., Nur, A., 2000, Seismic velocities and Poisson's ratio of shallow unconsolidated sands: *Geophysics*, 65(2), 559-564.

Christensen, N., Wang, H., 1985, The Influence of pore pressure and confining pressure on dynamic elastic properties of Berea sandstone: *Geophysics*, 50(2), 207.

Dvorkin, J., and Nur, A., 1996, Elasticity og High-Porosity Sandstones: Theory for Two North Sea Datasets: *Geophysics*, 61, 1363-1370.

Eberhart, D., Han, D-H., Zoback, H., 1989, Empirical relationships among seismic velocity, effective pressure, and clay content in sandstone: *Geophysics*, 54(1), 82-89.

Lemmon, E. W., McLinden, M. O., and Friend, D. G., 2003, Thermophysical properties of fluid systems, in NIST chemistry webbook, NIST standard reference database number 69, edited by P. Lindstrom and W.G. Mallard, National Institute of Standards and Technology (http://webbook).

Hornby, B. E., and Murphy, W. F., 1987, V_p/V_S in unconsolidated oil sands: Shear from Stonely, *Geophysics*, 54, 502-513.

Makse, H. A., Gland, N., Johnson, D. L., and Schwartz, 1999, Why effective medium theory fails in granular materials, *Phys. Rev. Let.,* 83, 5070-5073.

Mavko, G., Mukerji, T., Dvorkin, J., 1998, *The rock physics handbook*, Cambridge University Press.

Mindlin, R. D., 1949, Compliance of elastic bodies in contact: Trans. *ASME*, 71, A-259.

Mochinaga, H, Onozuka, S., Kono, F., Ogawa, T., Takahashi, A., Torigoe, T., 2006, Properties of Oil sands and Bitumen in Athabasca, CSPG, CSEG, CWLS joint conference, Calgary, AB.

Murphy, W.F., Winkler, K.W., Kleinberg, 1986, Acoustic relaxation in sedimentary rocks: Dependence on grain contacts and fluid saturation, *Geophysics*, 51, 757-766.

Nur, A., Mavko, G., Dvorkin, J., Glmudi, 1998, Critical porosity: a key to relating physical properties to porosity in rocks, *The Leading Edge*, 17, 357-362.

Terzaghi, K., and Peck, R.B., 1967, Soil Mechanics in engineering practice: John Wiley and Sons, Inc. 729p.

Theune, U., 2004, Seismic monitoring of heavy oil reservoirs: rock physics and finite element modelling, Ph.D. thesis, University of Alberta, 209 pages.

Toskoz, M. N., Johnston, D., Timur, A., 1979, Attenuation of seismic waves in dry and saturated rocks, *Geophysics*, 42, 950-956.

Rottenfusser, B. A., Palfreyman, J. E., and Alwast, N. K., 1998, Geology of the AOSTRA underground test facility site, in Int. conf. on heavy crude and tar sands, vol. 2, p. no 115, UNITAR/UNDP, Edmonton.

Wang, Z., and Nur, A., 1998, Effect pf temperature on wave velocities in sands and sandstones with heavy hydrocarbons, in Seismic and Acoustic Velocities in Reservoir Rocks, edited by A. Nur and Z Wang, vol. 1 of Geophysics reprint series, pp. 188-194, Soc. Expl. Geophysics.

Wang, Z., and Nur, A., 1990, Wave velocities in hydrocarbon-saturated rocks: Experimental results, *Geophysics*, 55, 723-733.

Wang, Z., Nur, A., and Batzle, M. L., 1990, Acoustic velocities in petroleum oils, *Jour. Petr. Tech.*, 42, 192-200.

Chapter 4

Application of a finite difference method to the acoustic wave equation

4.1 Introduction

To assist in the preparation, interpretation, and verification of real geophysical surveys, numerical simulations have become increasingly important in the past decades. Because seismic surveys are often parsimoniously sampled in space, and recorded waveforms are band-limited, predicting the distribution of geological and reservoir properties can be ambiguous, and this results in a model of the subsurface that is generally non-unique. To validate predictions about the material properties of the earth, simulated seismic surveys can be carried out on an approximate model of the earth. This is commonly referred to as the forward problem. If such synthetic data agree sufficiently well with real seismic observations, the model can be considered a valid representation of the reality. An application of forward modeling is the optimization of a survey design; where to place sources and receivers in order to maximize the quality of the data. This is especially important if the structure is already understood, as it is often the case in repeated or time-lapse experiments. In this Chapter, the physics of two-dimensional acoustic wave propagation is studied in the context of the effects steam zone footprints caused by the SAGD process.

Seismic waves can be described approximately by an acoustic wave equation. The acoustic wave equation is the simplest expression approximating wave propagation phenomena in fluid-like environments. During the reflection of a P-wave, part of the incident energy is reflected as a P-wave, part is transmitted as a P-wave and other parts are converted to S-waves (e.g. figure 1.4). As the acoustic wave equation does not account for shear waves, the reflected P-wave amplitudes can tend to be larger than when shear waves propagation is taken into account.

A complete description of wave propagation in earth materials can be studied using the full visco-elastic wave equation however this method is much more computationally extensive. Additional in order to generate synthetic seismic data through a visco-elastic earth, a continuous model of the earth must be built with parameters for P-velocity, S-velocity, density, and absorption / dispersion (attenuation) effects. At this time, there is insufficient knowledge about the shear wave and attenuation properties of oil sands materials in order to build a useful visco-elastic model.

The objectives of this numerical seismic experiment are the following: (1) accurately predict the surface recorded wavefield response manifested from the subsurface geology and the encroaching footprint caused by steam chambers throughout their evolution, (2) assess the feasibility of seismic monitoring by studying the sensitivity to velocity anomalies in the steam chamber, (3) understand the resolution limitations of the time-lapse seismic data signals, and (4) carry out survey planning with regard to the logistical confines of cost, time, resources, and geological aspects.

4.2 Modeling the physics of the SAGD process

4.2.1 - Description of the geologic setting: a motivation for modeling

Because the UTF Phase B site was an experimental test facility, the observation wells were positioned with an unusually close spacing (figure 4.1). It is rare that a geological area of interest in intersected with such a high density of boreholes. The well logs indicate a high degree of semblance from one well to the next and major transitions in the log curves are found only the vertical direction. For this reason, it was deemed appropriate to construct an acoustic velocity model with the same resolution as the sonic logs. Therefore, a two-dimensional acoustic velocity model was created by directly interpolating between the well logs, and it is assumed that this is a suitable and sufficiently detailed representation of the earth.

The geologic neighborhood for the McMurray Formation is similar in all areas; it is underlain by high velocity Paleozoic carbonates and overlain by the marine deposits of the Clearwater formation, which are mainly composed of thin silts and shales (Strobl, et al., 1997). Also, within the study area, 2-3m thick low velocity gas-saturated sandstone named the Wabiskaw gas-sand directly overlies the McMurray formation (figure 4.1). It can be seen clearly on the wireline logs and by its extremely low velocity and serves to be an important marker horizon for geologic correlation and seismic imaging. The reservoir has porosities ranging from 30 – 42% (Chalaturnyk, 1996) with a bitumen saturation $S_o \approx 89\%$. In the Athabasca region, the bitumen is common referred to as a semi-solid and it is thought that the bitumen actually supports the matrix grains. This is because the rocks are young and the timing of the oils into these rocks happened before the fluvial deposits were given a chance to undergo lithification. The vertical

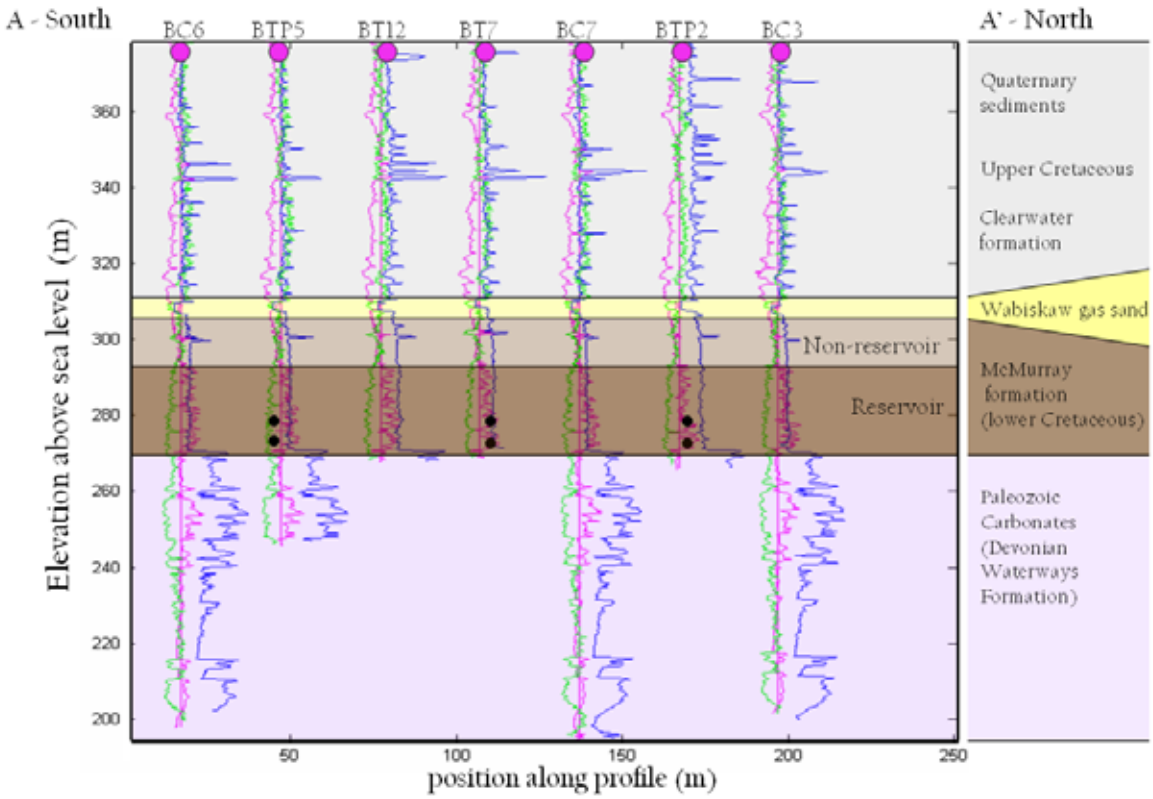

FIG. 4.1. Well log cross-section running south to north across the 3-well pairs at UTF. Gamma-ray is green, resistivity is pink, and P-sonic is blue. The observations wells are spaced approximately 40 m apart and the greater stratigraphy seen from the log curve signatures are incredibly consistent across the short distance shown here. The approximate positions of the horizontal well pairs are indicated by the black circles (coming into and out of the page).

permeability of the highest quality reservoir averages to k ≈ 4D, a parameter that makes the SAGD process possible. Viscosity of bitumen can vary dramatically due in part to the state of biodegradation history and hydrological contact, but is around 18 Pa·s. The oil is virtually immobile at virgin reservoir temperatures of 8ºC (7, 000, 000 cP) but can begin to be mobile at 38 ºC (7,000,00 cP) (Chalaturnyk, 1996). The reservoir is riddled with abrupt facies transitions and discontinuities, whereby laminations of siltstone and mudstone within the reservoir can act as vertical or lateral permeability barriers for steam

expansion. Barriers may cause permeability anisotropy in both the steam chamber expansion and oil recovery drainage patterns.

The study area is relatively small and there is exception high density coverage of wireline logs across the site. Observation wells are spaced approximately 40 m apart, and adjacent wireline curves (particularly in the McMurray formation and in the underlying carbonates) are virtually identical one to the next. This is not to say that the McMurray formation lacks heterogeneity, in fact, Chapter 2 served to deliberate at length the internal complexity of the reservoir system. There are probably minor hetereogenieties and lithological variations over short distances, but in this setting, the wireline logs do not show large features such as mud-filled channel plugs or abrupt lateral discontinuities. There is slightly more variability in the Quaternary sediments closer to the surface. Given the density of the well log sampling, it is believed that a 2-D geologic model can be built with sufficient detail and resolution in order to accurately study the effect of a steam zone on seismic data.

4.2.2 Building an acoustic velocity model

The work of chapter 3 served to estimate the effective change in P-wave seismic velocity due to an ideal steam injection case within this reservoir. The exact shape of a steam chamber created during a SAGD program within a reservoir is generally unknown but it can be expected to be complicated. As there are currently no results from reservoir simulations or field observations publicly available, only geometrically simple and schematic models can be used to describe the distribution of pressures, temperatures, oil, water, and steam saturations.

The simple model employed here is based on the assumption that the hot and low density steam rises to the top of the reservoir and then spreads out laterally. The heated oil then slides down the walls of the steam chamber along a sharp thermal gradient between heated and cold reservoir. A temperature cross-section was created by interpolating borehole thermocouple measurements through a single idealized steam chamber (figure 4.3). The maximum width and height of this steam chamber is 48 m and 20 m respectively. In this temperature profile, the transition from red to yellow marks the boundary of the steam chamber; inside is the zone of depleted reservoir with steam in the pore space, outside is undepleted reservoir being heated through conduction. The magnitude of the velocity anomaly in the center of the steam zone has been taken from the intermediate pressure / temperature scenario from Chapter 3 (figure 3.13).

The impregnation of the lower P-velocities from depleted reservoir into the original background velocity model is shown in Figure 4.4. Here, it is seen that the velocities anomalies are indeed large with respect to the background velocities. Because the UTF facility has three well pairs in close proximity, studying the steam zone effects from one well pair in isolation might be too simplistic. A survey is first computed over a simple case with just one steam zone in the reservoir (A). Second, we consider the more complicated case when 3 steam zones are spaced closely together (B). The well pairs (or centers of steam zones) are spaced 70 m apart, which is identical to the borehole positioning in the field.

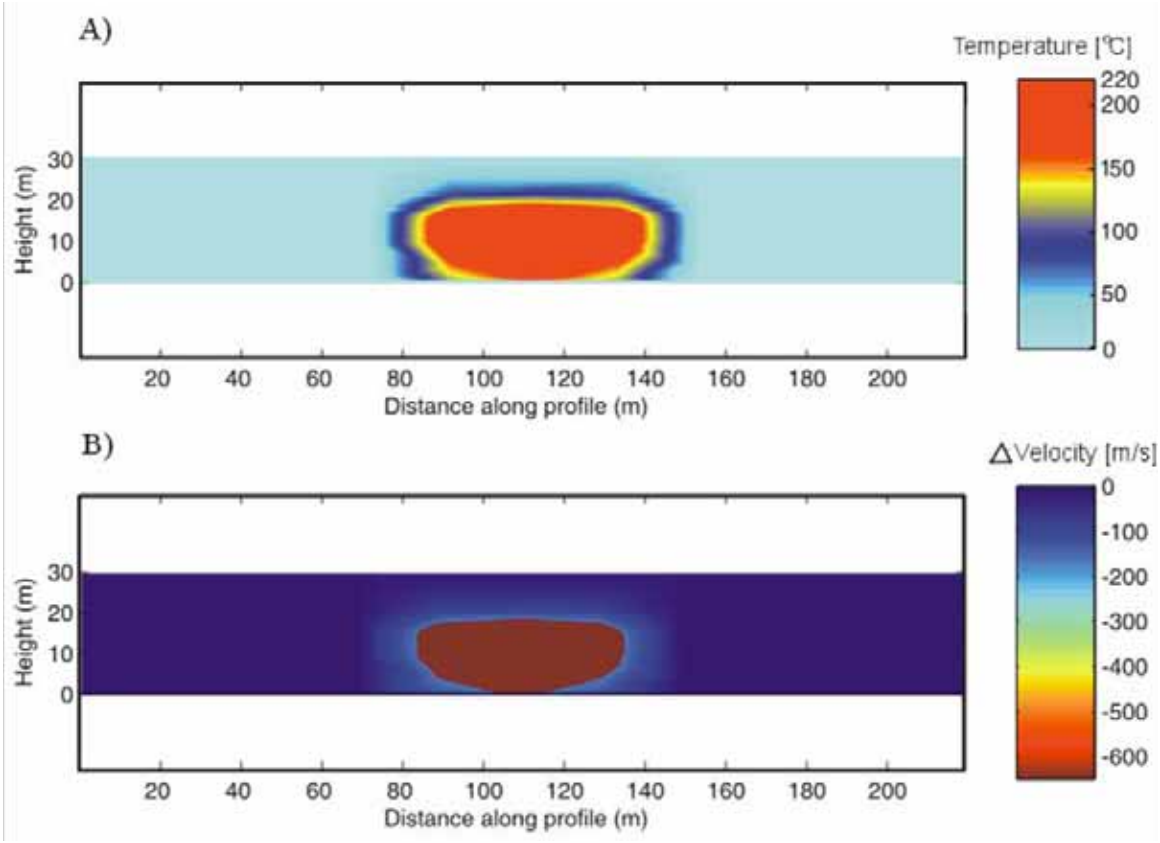

FIG. 4.2. A) Hypothetical temperature profile of a typical steam chamber in Athabasca reservoir B) Computed P-wave velocity anomaly result from rock physics and fluid substitution analysis from Chapter 3. The maximum width of the steam zone is 48 m wide.

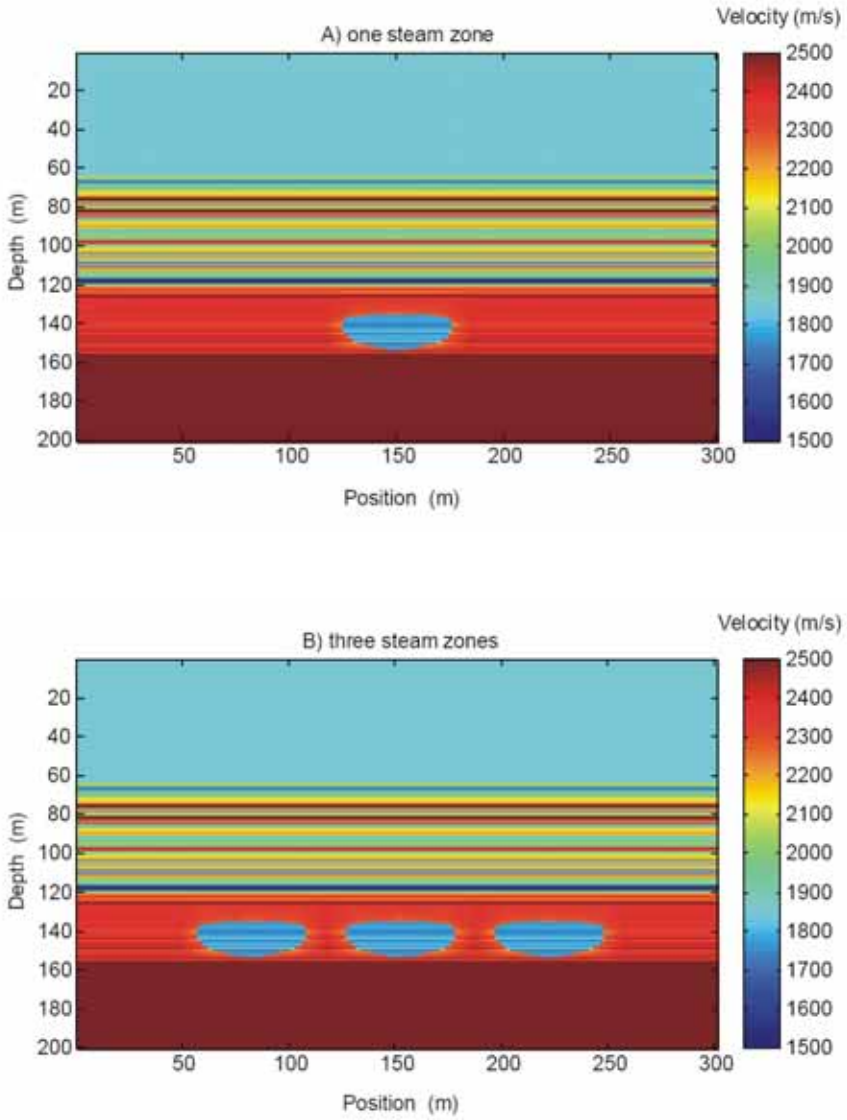

FIG. 4.3. Cross-sectional velocity models used in generating synthetic seismic data. A 'reference' or 'baseline' data set was computed without the steam zone anomaly, using the background velocities only. These two velocity models represent a snapshot in time after steam chambers have developed.

4.3 Notes about the velocity model for numerical methods

4.3.1 Near surface inconsistency

Many of the challenges associated with land-based seismic acquisition stem from variations in topography and velocities of the near surface. In the field, unconsolidated soils or shallow weathering layers can decrease the ability to send and receive high fidelity seismic waves into and from the earth. Furthermore, near surface velocities are seldom sampled by well logs because steel casing tubes are placed in the top of boreholes used to sturdy the open pathway to the surface. The velocity model shown in Figure 4.3 shows a 60 metre constant velocity layer of 1850 m/s in the shallowest part of the subsurface. It is likely that the actual near surface velocities are much less than this. For instance, Bachrach et al. (1998) performed a series of shallow seismic experiments on a sandy beach and found that velocities were less than a few hundred metres per second. This experiment is an extreme case of completely unconsolidated material with no confining pressure. The inability of such materials to resist deformation places a limit on the quality of signal that can be sent into the earth. Additionally, Miller and Xia (1998) demonstrated the intractable nature of low velocities in the near surface by quantifying extremely large gradients in velocities on conventional shot gathers. For the numerical experiment presented here, the near surface must be simplified in order for the algorithm to work properly. The entire seismic pulse or initial wavefield must be established at time zero without being in contact with discontinuities in the model in order for the numerical algorithm to be stable. So in fact, even if wireline logs actually recorded measurements all the way up to the surface, this information would still need to be

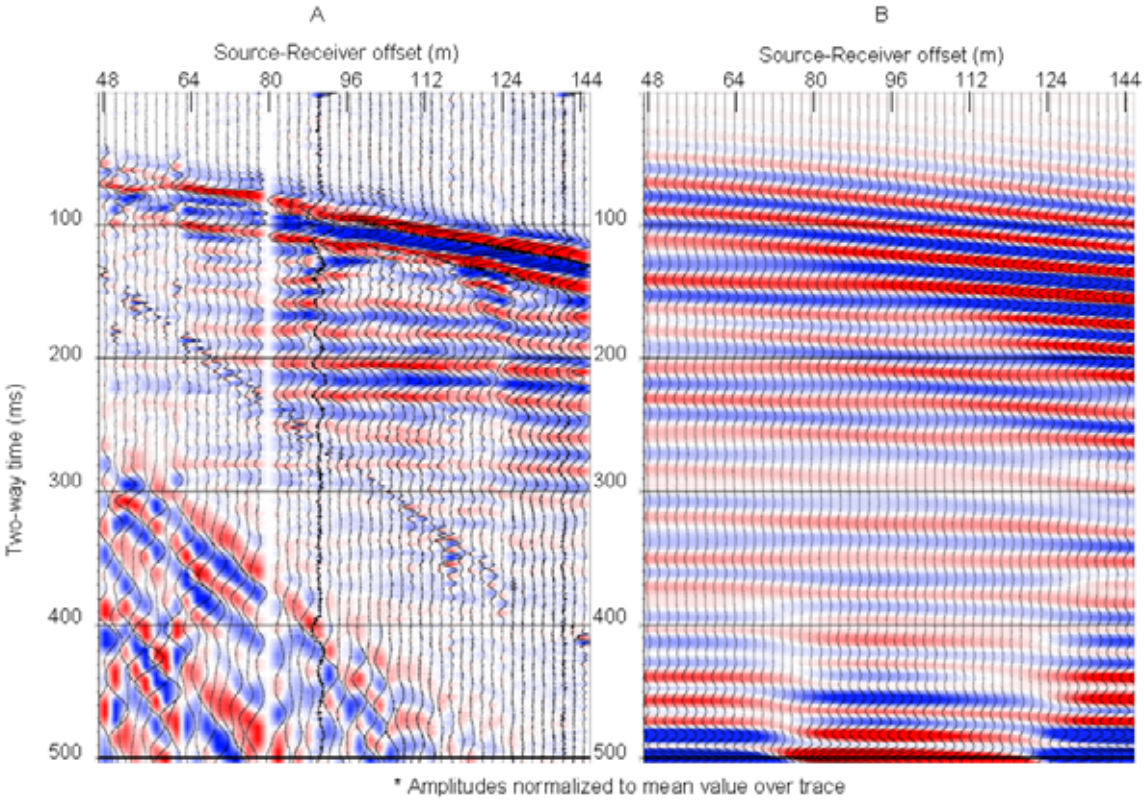

FIG. 4.4. Comparison between shot gathers generated in the field (A) and numerically (B). The finite difference approach fails at producing the near surface refractions (seen at near offsets in the left panel at ~80 ms), the ground roll and airwave (seen at near offsets on the left panel at ~300 ms), but generally does an acceptable job at estimating reflections within the region of interest (~125 - 250 ms).

omitted from the physical model. It is recognized that the near surface portion of the data set will be subject to the most disagreement with reality. Finally, of course ground-roll surface waves and air wave noise are signals generated by physical phenomena that cannot be reproduced by this numerical algorithm (figure 4.4).

4.3.2 Sonic to seismic

The physical earth models used in the generation of the synthetic seismic data sets are limited in two fundamental ways. First, the interval velocities that seismic waves experience with relatively low frequencies may not be identical to those measured at the

borehole walls by the sonic tool. Schmitt (1999) overlaid measurements of interval velocities made by a VSP (Vertical Seismic Profile) with measurements collected by a wireline sonic tool at the UTF site. There was a significant difference between the two within the oil sands interval which was partially attributed to dispersion and attenuation. The second fundamental limitation is, because this algorithm is based on the acoustic wave equation, only P-wave velocity information can be invoked. The ideal treatment would be to build a full visco-elastic physical model of the earth, however the spatial distribution of S-velocities, and dispersive / attenuation properties of the earth not known with sufficient detail to solve this problem. Furthermore, the development of a functional visco-elastic numerical algorithm is beyond the scope of this investigation and would come with dramatically increased computational costs. Others have been successful in developing finite-difference simulators to model wave propagation in visco-elastic media (e.g. Robertsson et al., 1994, and Stekl and Pratt, 1998) however these algorithms have been tested on only relatively simple physical models. With the recognition that the SAGD process has a profound effect on P-wave velocities alone, it is justifiable to stay within the confines of the simpler acoustic treatment and look towards more realistic simulations in the future.

4.3.3 Boundary Conditions

Boundary conditions for most finite difference algorithms are usually inserted to mediate unwanted reflections off the edges of the model. For simplicity reasons, no boundary conditions were incorporated into these simulations, instead the velocity model was simply extended laterally outward and vertically downward so propagating energy

never actually reaches the boundary of the model over the length of time that the wavefield is recorded. The effective study area is only about 150 metres on either side of a single steam chamber, but the model was extended to a total horizontal length of 2000 metres to avoid unphysical reflections off of the model boundary. This is a rather crude, but effective, method for eliminating model edge effect problems.

4.3.4 How was the data collected?

The seismic data was admittedly over-collected in terms of receiver and shot placements. 200 shots were collected every 2 metres along the profile and 300 receivers were placed (with 1 m spacing) both in front of and trailing the source shot position. This geometry yields a common-midpoint (CMP) spacing of 1 metre far beyond the area of interest. It was not until the data was analyzed prior to processing and imaging, that traces with source-reciever offsets less than 150 metres were selected for analysis and imaging. The record length of each shot was time duration of 512 ms.

4.4 Numerical experiment results – simulating the SAGD process

4.4.1 The use of color to emphasize seismic data attributes

In this section, there will be examples shown when the choice of color scheme will significantly benefit certain characteristics of the seismic data. When a "rainbow" color-bar scheme is chosen herein, the reader will be guided to focus on amplitude variations with the data. When a "red-white-blue" color-scale is shown, it is with the intention to emphasize reflection character or layering of the peaks and troughs of within the data.

4.4.2 Raw shot gathers

It was initially thought that a single raw shot gather could provide a wealth of information about the time-lapse evolution of steam zones. The process of stacking seismic events assumed to be reflecting off the same point in the subsurface has been one of the most widely and successfully applied tools in geophysics for increasing the signal to noise ratio. The problem, of course, is that any information that is critical to a specific path that the seismic wave has traveled is lost when multiple signals are smeared together. An example of such a signal that might vanish is shown in figures 4.5 and 4.6. Here are traces recorded from single shot records for a case where, A) no steam anomaly is present beneath the shot, and B) a small (10%) steam anomaly is present beneath the shot (the shape of which is shown in figure 4.7). The raw data collected here is much higher bandwidth than could ever be collected in the field however a bandpass filter can be applied to the final processed image to match the frequency content of real field data. In figure 4.5, the moveout and curvature of the reflection events are seen to be distorted with the presence of even this small velocity anomaly. There is a small amount of travel time delay experienced by the seismic waves that pass through this zone, but elsewhere the reflections remain undisturbed. The subtle signals contained within specific recorded offsets will be most likely be lost if stacking is performed. Also, if receivers are spaced too coarsely, the anomaly may be insufficiently sampled or entirely missed altogether.

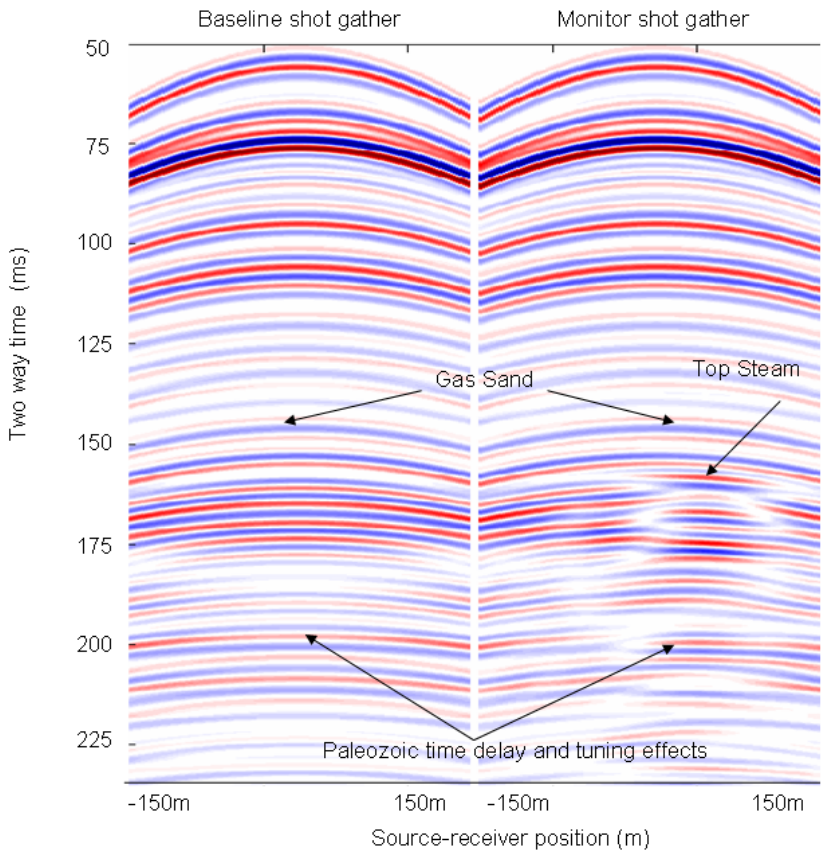

FIG. 4.5. Baseline shot gather (right panel) and monitor shot gather (left panel) generated from finite difference algorithm. For numerical stability reasons, a broadband Ricker wavelet, comprised of frequencies from 10-200 Hz was used as the seismic source. The monitor survey in this figure is shot over the very small velocity anomaly shown in figure 4.6. Blues are troughs, reds are peaks.

Geophysicists often take two or more seismic surveys and make their signals uniform or "equalized" (e.g. Rickett, 1997, and Ross et al., 1997) in order to extract quantitative time-lapse information. The need for such pre-processing is demonstrated here, when the difference is taken between a baseline shot record and a monitor shot record (before and after the velocity anomaly has been inserted into the model) over the same area. The difference panel in figure 4.6 is unfortunately not a clear and concise

image of the steam chamber, and no longer do the signals contain quantitative information about the time-lapse anomaly.

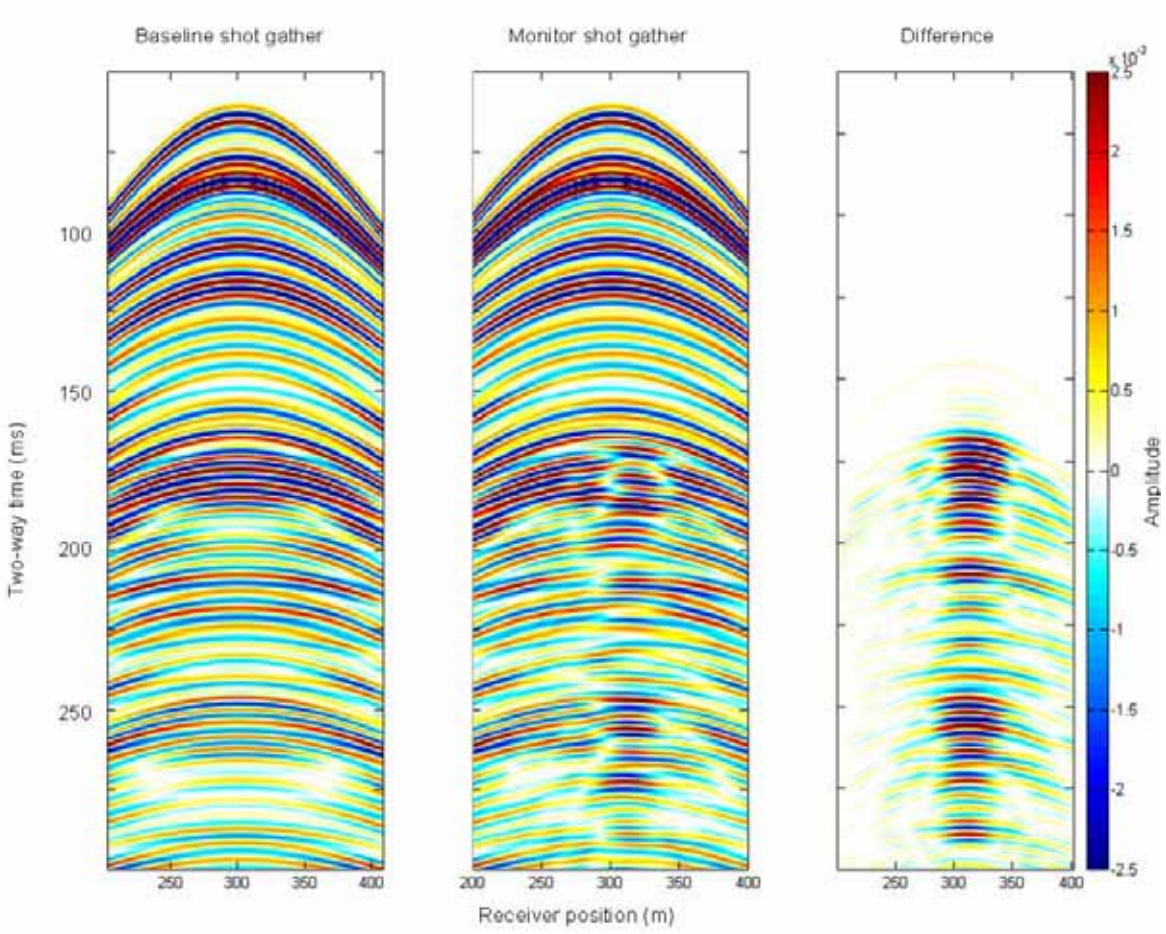

FIG. 4.6. Taking the difference between time-lapse surveys may provide unphysical reflection signals.

4.4.3 Model space waveform snapshot

One of the lures of finite difference modeling is that the wavefield can be recorded at any point in space, not just at the surface. Perhaps a more intuitive representation of wave propagation through a steam zone can be achieved by taking a

snapshot of the wavefield propagating through the model space (figure 4.7). Here the reflections coming off the down-going pulse for the baseline (A) and monitor survey (B) can be directly juxtaposed against the reflectivity model (C) in depth. Here, one can directly see the energy that radiates upwards from each layer or discontinuity in the model. These snapshots were taken shortly after the seismic pulse travelled through the reservoir and into the underlying carbonates. The reflection from the Paleozoic unconformity underlying the reservoir is the largest as well as the deepest reflection returning to the surface. The steam anomaly is seen to be affecting the entire train of reflections from the top of the reservoir to the base of the reservoir. Actually, as will be further illustrated in stacked profiles, the steam zone acts somewhat as a local waveguide, whereby internal multiples radiate and continue to distort reflections returning from deeper in the model. The anomaly shown here is only a 10% decrease relative to the background, and the disturbance produced is still profound.

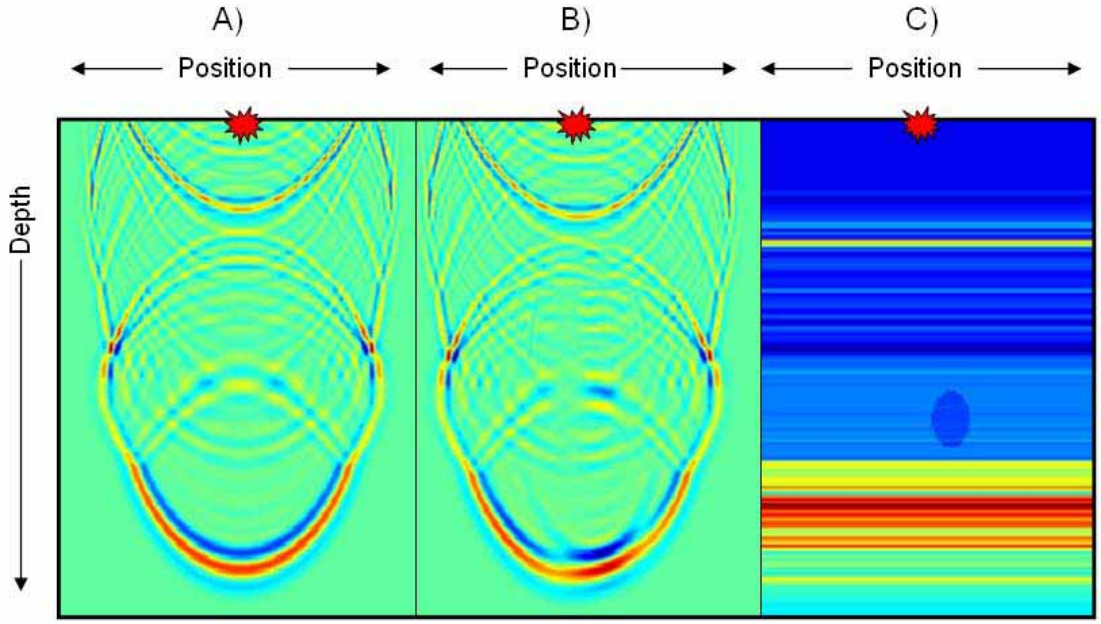

FIG. 4.7. Snapshots of the numerically generated acoustic wavefield taken after the shots have been fired. The bright arcuate transmitted pulse has propagated down into the Paleozoic carbonates at the time the snapshot was taken. In A, the wavefield propagates through the velocity model (C) without a steam anomaly inserted. In B, the wavefield is that through the velocity model (C) with a small elliptical velocity anomaly inserted as shown. The ellipse is 15 m wide and 20 m high, and the velocities within the ellipse are 90% of the surrounding background. This is 10% decrease in velocity indicative of a heated zone. The red values on the wavefield snapshots are compressions (peaks) and the blue values are dilatations (troughs). In the velocity model (C), the 'cold' blue colors are low velocities, and the 'hot' yellow and red colors are fast velocities.

4.4.4. Seismic Processing Workflow and Imaging

Data generation

The wavefield simulation experiement was divided up and processed on 4 parallel processors on *WestGrid*. The data was collected shot by shot, where each file corresponded to a different shot position along the profile, and because the velocity model is horizontally symmetric about the center vertical axis, shots were computed over only half of the model. The second half of the data set was reconstructed using

reciprocity. The finite difference program was written and implemented by S. Kaplan (Ph.D. Candidate at the University of Alberta).

Velocity analysis, NMO correction and Stacking

A semblance[5] plot (figure 4.8) through a CMP[6] gather shows smearing of the energy maxima which present an unclear picture of the RMS velocities. The RMS or stacking velocity maxima on the semblance plots at the depth of the steam zones were not significantly shifted from those away from the undepleted region, only the maxima were smeared. The maxima on the semblance plots at the depth of the steam zones did look much more smeared laterally, presumably from small scale internal multiple events.

4.4.4 Processed seismic profiles

In this section, a number of comparisons are presented between various processed steam anomalies and real seismic data collected at the UTF site. A more

---

[5] Semblance is a quantitative measure of the coherence of seismic energy from multiple channels. RMS velocities can be estimated from velocity spectra obtained from a CMP gather (or multiple adjacent CMP gathers). This is often called 'velocity analyses'. Semblance is defined as:

$$Semblance = \frac{1}{n}\frac{\sum_t s_t^2}{\sum_t \sum_i w_{i,t}^2}$$

where s_t is the amplitude of stacking defined by,

$$s_t = \sum_{i=1}^{n} w_{i,t}$$

n is the number of traces along a moveout corrected CMP gather, w is the amplitude value on the *i-th* trace and two-way travel time t. Semblance is a measure of coherency and is tested for a range of velocities. The position of the semblance maxima are located at the best RMS velocity values that define the hyperbolic shape of the travel time moveout of the reflection events with offset.

[6] CMP stands for 'common-midpoint', and is used to denote the horizontal position along a profile at which seismic ray paths of different offsets converge at the same imaging point in the subsurface. The term CMP is used somewhat interchangeably with CDP – 'common depth-point' or CRP – 'common reflection point'.

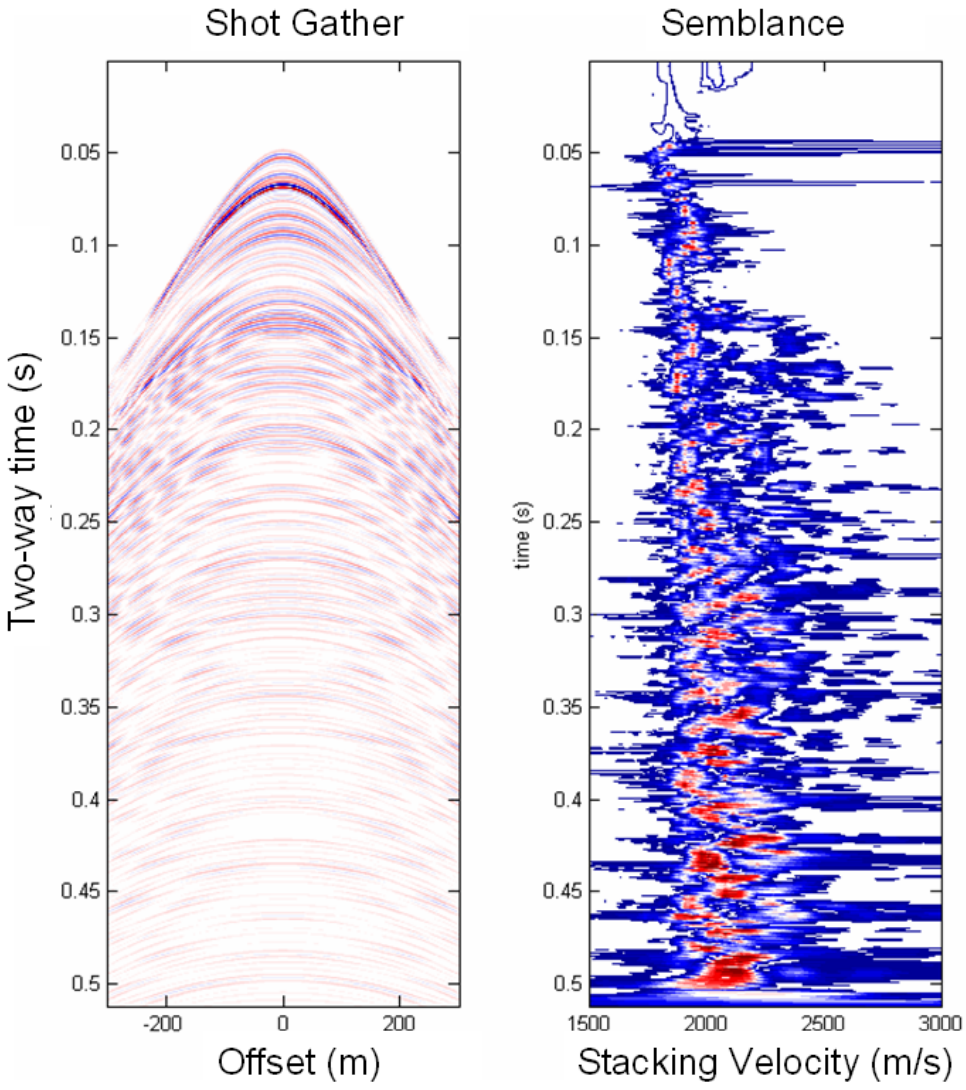

FIG. 4.8. Shot gather image and semblance profile showing reflection maxima.

complete description of the real seismic data is presented in the following Chapter. In this section several figures are shown in duplication; the first figure is stripped of any annotation or interpretation, whereas the second is presented with key surfaces and features identified. The intention is for the reader to be directed to the rather ambiguous seismic images first, in order to discover the complexity contained within the captured

signals. The challenge will be, such as it is in the field, to justify the seismic data prior to having reference to the physical earth model from which it manifests.

Most geoscientists create single-trace synthetic seismograms from well logs in order to link a well log in depth to a real seismic trace in two-way time. This is done by taking a well log-derived reflectivity series and convolving it with a wavelet chosen to match the frequency and phase contained in the real seismic data. On one hand, it can be thought of as an erroneously simple model that fails to account for the proper physics of wave propagation. But on the other hand, it can be thought of as the ideal record of the reflecting layers within the earth; an invariant traveling seismic pulse that is ignorant to the complications of noise, attenuation, multiples, or scattering phenomena. In fact, achieving a "convolution-like" seismic trace in real data has been the goal of extensive migration and internal multiple removal research within the seismic industry. Figure 4.9 shows a comparison between the perfect seismic image (one-dimensional convolution) and an imperfect seismic image representative of 2-dimensional acoustic wave propagation. The panel on the left portrays 3 intuitive seismic effects of a steam zone. First, the top of the steam zone corresponds to a strong trough event, and this event is bound by symmetric side lobe peaks of a zero-phase seismic pulse. The top of the steam zone is a trough because a negative reflection coefficient exists at this upper boundary. Second, the base of the steam zone causes a localized increase in amplitude because of the larger positive reflection coefficient created at the interface between the base of the reservoir and the top of the Paleozoic carbonates. And last, a significant time delay is observed beneath the steam zone due to the fact that the seismic waves travel slower though the depleted zone than the undepleted zone.

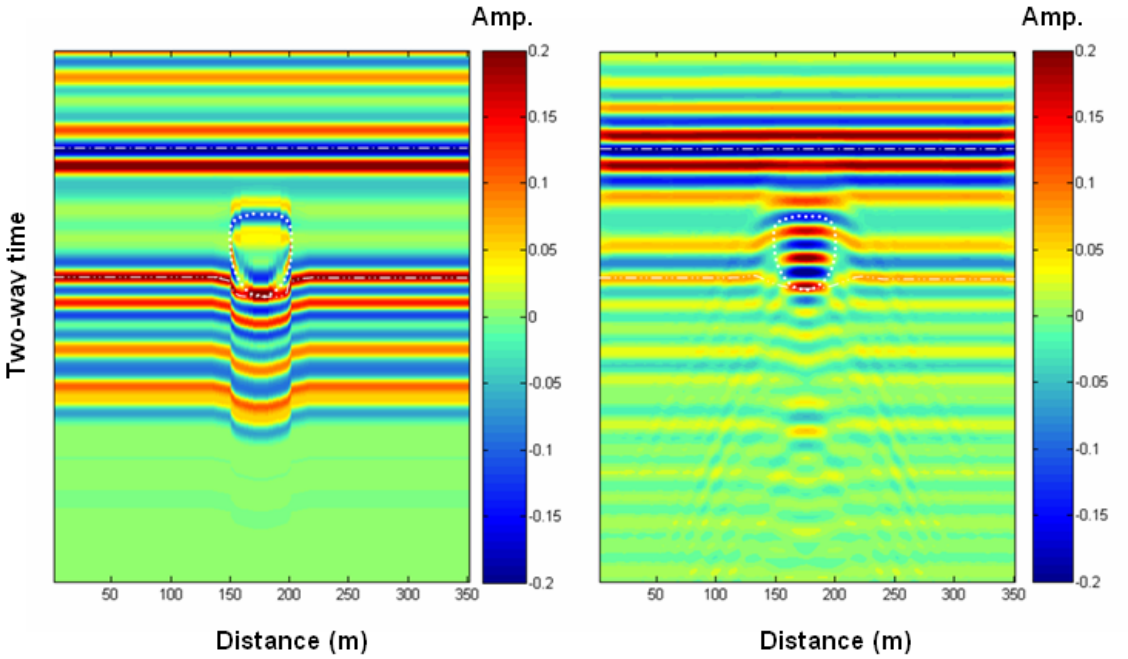

FIG. 4.9. Comparison between an 'ideal' seismic profile (left), and a more realistic seismic profile over one steam zone (right).

We see all of these attributes (amplitude decrease at the top of steam zone, amplitude increase at the base of the steam zone, and travel-time pull-down) in the right hand panel as well; however the picture is not as clear. In this image, the top of the steam zone is also marked by a strong trough however it is slightly curved and is larger than the actual steam zone itself (dashed line). Additionally, the amplitude increase at the base of the steam zone is significantly greater than on the left panel, however it appears to be smaller in size than the velocity anomaly. Also, we see that the travel-time pull down is identical for both cases. Furthermore, both the top and base of the steam zone act as a scatterer, portraying independent sets of remnant diffractions that remain after NMO correction and stacking have been applied. The two sets of diffractions actually have different curve shapes, the top set is faster (shallow hyperbolae), and the bottom set is

slower (steeper hyperbolae). It is possible that the bottom set of diffractions are retarded through propagation within the low velocity steam zone, whereas the top set is not and is merely diffracting off the surface of the steam zone. Fomel et al. (2007) have demonstrated the ability to perform migration on data using diffraction information alone and there may be some promise to using their method to actually extract quantitative time lapse information from them.

The next images (figures 4.10 and 4.11) illustrate the sensitivity of seismic to detect a very small steam zone. The velocity model on the left was impregnated with a elliptical shaped steam zone 15 metres wide, and 20 metres tall, and a constant 10% velocity decrease relative to the background. This is compared to the easily detectable anomaly as shown in figure 4.9. On the left, the top of the steam chamber can barely be seen as the reflection character is distorted only slightly. There is not any significant pull-down or amplitude anomaly associated with the reflection at the base of the reservoir, but diffractions are still detected. If would be difficult to detect such a small anomaly in the field in the presence of noise.

It would be incorrect to consider one steam zone in isolation when the actual case at the UTF site has three steam zones operating simultaneously. This is investigated in a couple of ways. A serious pitfall in upgrading a one-steam-zone model into a three-steam-zone model would be encountered if the three steam zones were surveyed, each in isolation, and subsequently stacked. This approach is displayed in Figures 4.12 and 4.13

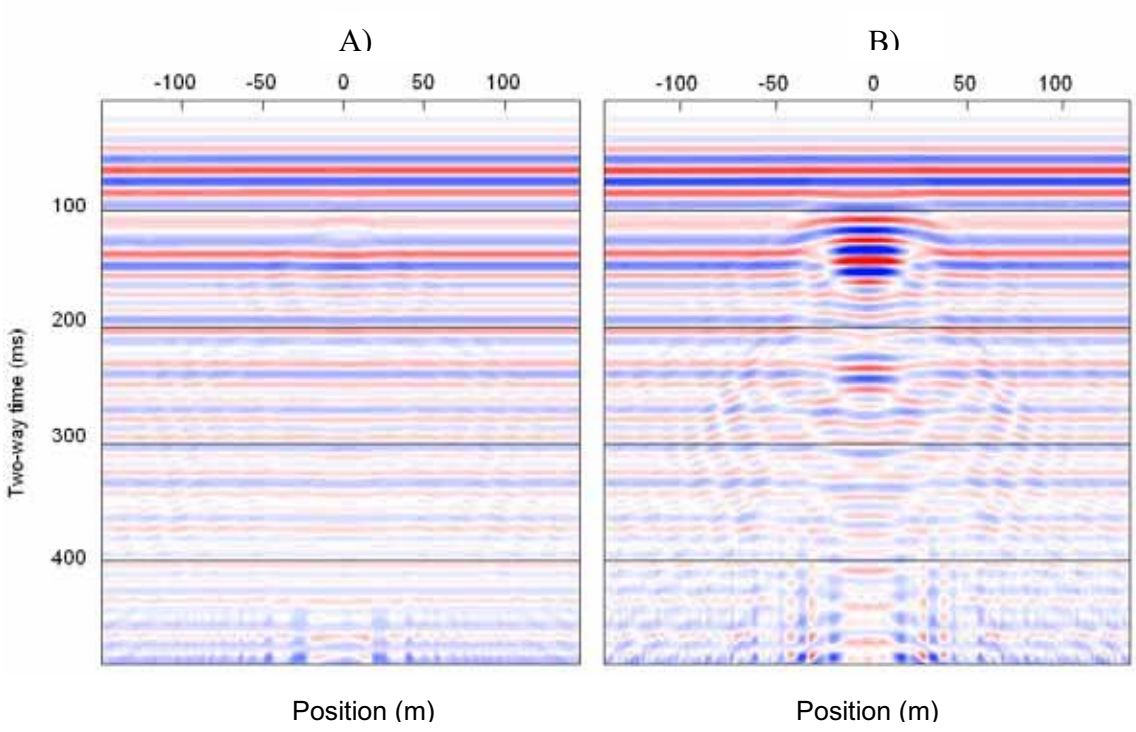

FIG. 4.10. Post-stack synthetic seismic section showing steam chamber anomaly with velocities decreased by A) 10% relative to the background velocity model, and B) 35% relative to the background velocity model. The offset range used in these stacked sections is 48 -142 m. No migration or deconvolution has been applied in the processing of these data. Note, these data have been filtered after stacking with a bandpass filter with corner frequencies 0-5-55-70. Blues are positive amplitudes and red are negative amplitudes. Furthermore, a t^{α}-style gain has been applied ($\alpha = 1.5$) in order to highlight the diffractions at later travel times.

and it can be thought of as an erroneous way to extend a one-steam zone model. It is shown here for illustrative purposes. The top panel is the seismic data for one-steam zone, and the bottom panel is the shifted summation of the top panel three times. In this model, the seismic waves have no physical interaction between one steam zone and the next, and although it is incorrect, it shows some interesting results. Since the three-steam zones are so closely spaced, the diffractions off the top of one steam zone interferes with the adjacent steam zone and the overall seismic anomaly is decreased. These diffractions are so prominent that they actually force the re-positioning of the unconformity reflection

event, making it shallower in time than the true model (Figure 4.13B). In this case, the travel-time pull down is too small and is not consistent with the strength of the anomaly. It was not clear at the time that this data was calculated that the stack of three independent steam zones data sets would look different than one data sets collected over a simple model impregnated with three steam zones. Admittedly, the forced generation of this data is too parsimonious. It is now clear that there is no shortcut for modeling the full interaction of the seismic wavefield with three steam zones in the reservoir.

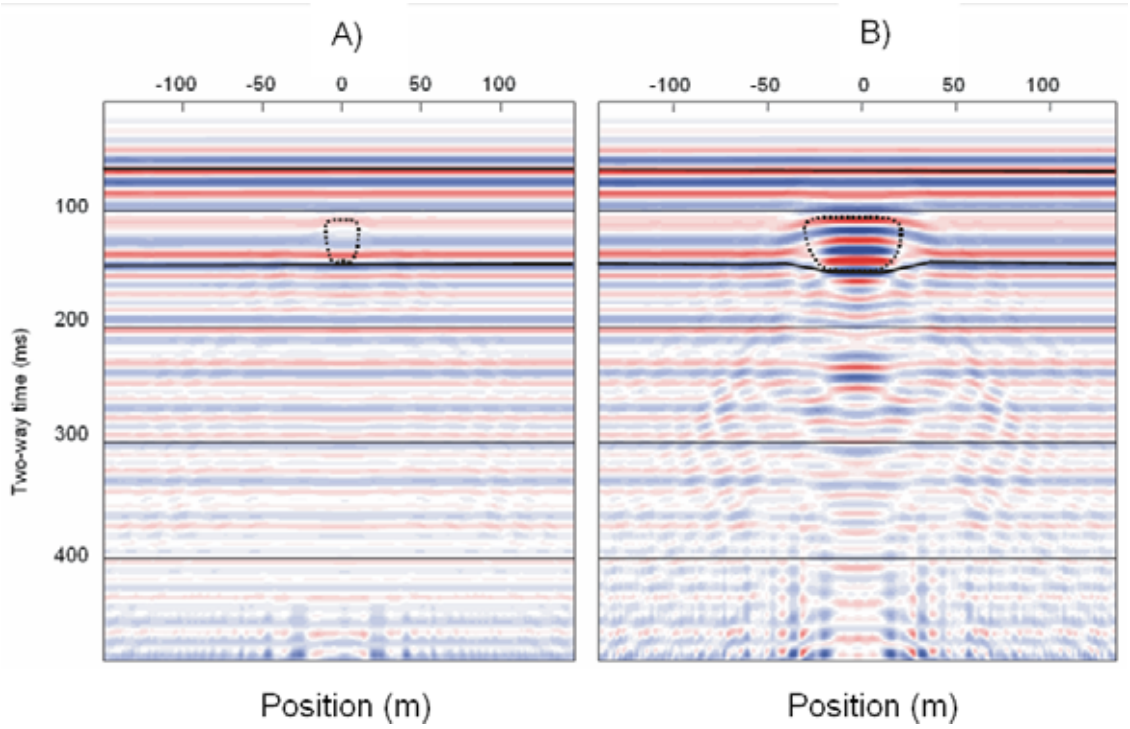

FIG 4.11. Annotation of steam zone anomaly on seismic section. The true vertical thickness of the steam zone in B) is the same as the true vertical thickness as the steam zone in A). The apparent elongation of the steam zone is due to the increase travel time delay through the zone. The steam zone have the same shape, however the width of the steam zone in B (48 m) is three times wider than the steam zone in A (16 m).

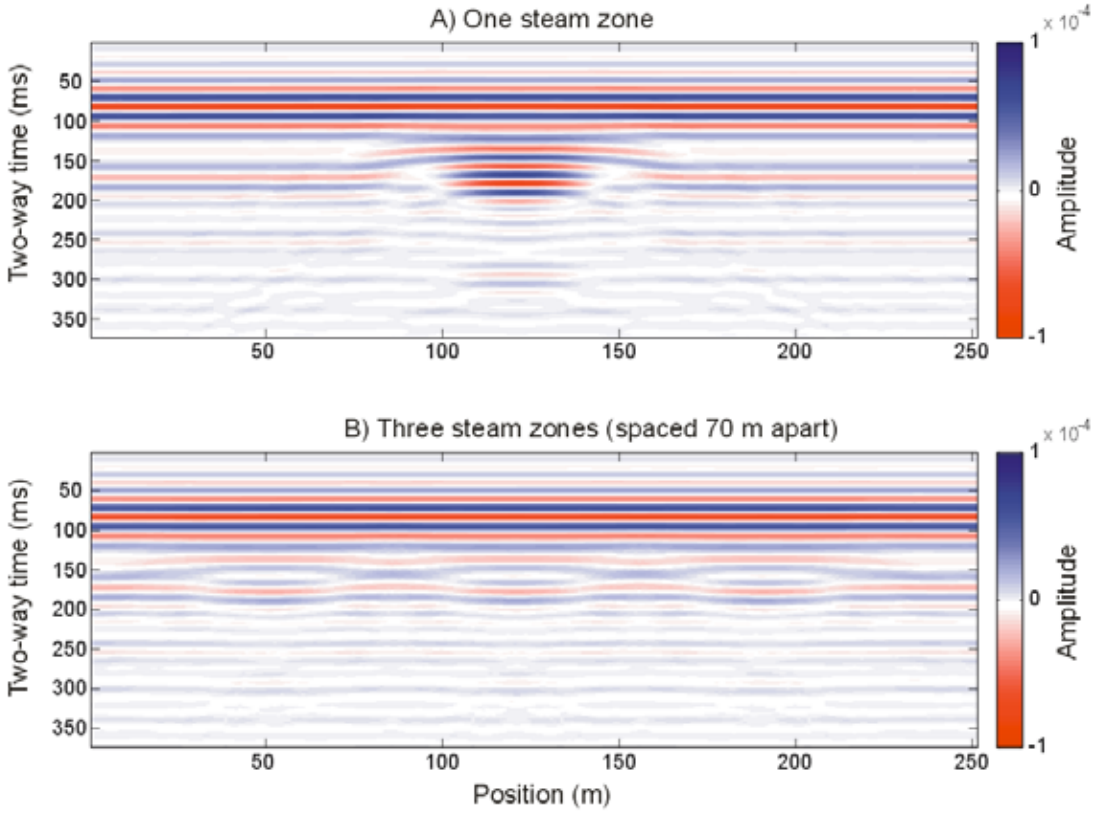

FIG. 4.12. The trivial summation of one steam zone shifted three times does not take into account the 2-D superimposing of diffracted energy and generated intra-steam zone reverberations. The three-steam zone model in B) was created by shifting the center steam zone seismic data (at 120 m) to make three independent steam zones models (with centers at positions 50, 120, and 190 m) and subsequently summed. Such interference can make time-lapse imaging problematic, but this model is too simplistic. Although the strength of the anomalies in B is significantly diminished relative to the anomaly from a single steam zone, the true physics of three steam zones is not accurately determined.

Figures 4.14 and 4.15 compare the seismic footprint of one steam zone in isolation with three steam zones spaced 70 metres apart as they are at the UTF project. Here, the intra-steam zone interaction are fully recovered and create a unclear picture of the velocity anomalies and make it very difficult to interpret the boundaries of the steam zone. The overall brightness of the anomaly is decreased, which was similar to the trivial model just discussed, and the top and base of the steam zone is not easily picked as it is in

the single-steam zone case. Furthermore, the supposition that the amount of travel-time pull down of the reflection peak caused by the Paleozoic unconformity is proportional to the thickness of steam zone above is incorrect in this case as well. Here, the maximum "pull-down" is actually beneath undepleted reservoir, equally spaced between adjacent the steam zones.

This seismic anomaly is not actually a true "pull-down" at all, but is the result of diffraction interference and scattering. Care must be taken then, when using the travel-time shift below the reservoir as a proxy for total steam thickness. Finally, the center steam zone anomaly is perfectly symmetric; however the outer steam zones have asymmetric anomalies because they are affected only on one side. Because of this interference, the center steam zone anomaly is smaller in size and would presumably be interpreted as less total steam, even though it stems from the same physical shape as its peripheral neighbors.

These observations are critical in diagnosing the complex signals contained within the real time lapse data at UTF. The top panel in Figure 4.17 shows the first seismic line collected in 1995, which is after about three years of steaming. Just as was shown in the previous model, the maximum travel-time of the Paleozoic reflection does not correspond to the location of the 3 well pairs. In this figure, the well pairs are located at 30, 120 and 190 meters. The dominant frequencies contained with the field data are significantly less than those in the numerical data, however the major features have been successfully reproduced.

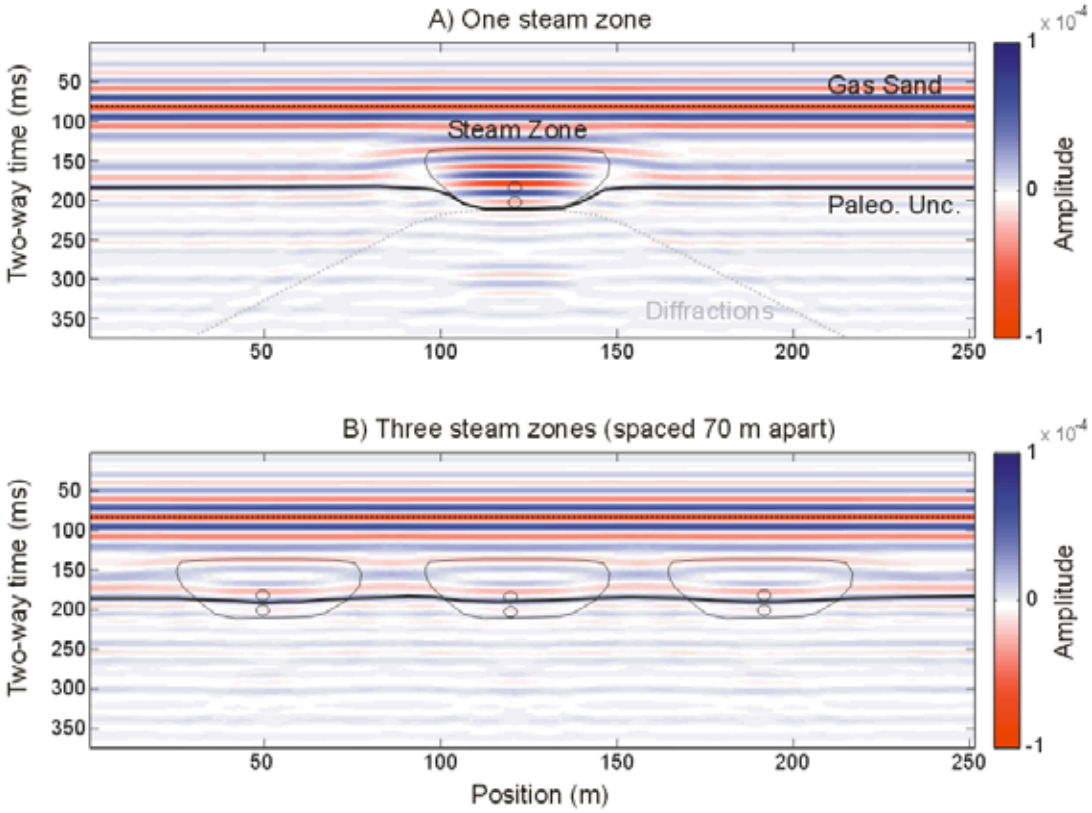

FIG. 4.13. Annotation of key horizons and features within synthetic steam zone model. In A, a maximum travel time delay in A of 55 ms, and the local increase in amplitudes are clear indicators of the steam zone. The top of the steam zone is marked by a clear trough event, and the bottom of the steam zone is delayed and shows tuning with the Paleozoic Unconformity. In B, the maximum travel time delay along the Paleozoic Unconformity horizon is 4ms. Caution must be taken when picking Paleozoic Unconformity event as a travel time reference marker. The true position of the 3 steam zones (drawn in travel time) is not resolved by the reflection events in B).

A slightly higher quality line collected in 1999 shows a better fit with the numerical simulation. This data set has generally greater bandwidth. Although, at this time there is no way of determining the actual distribution of steam zones due to the inaccessibility of the geotechnical information, it is evident that the anomalies chosen for the ideal velocity model present a strikingly comparable footprint on the seismic data. In

fact, the real data shows subtle hints of diffraction hyperbolae, especially beneath the center steam zone, even though the data appears to be significantly aliased below 250 ms.

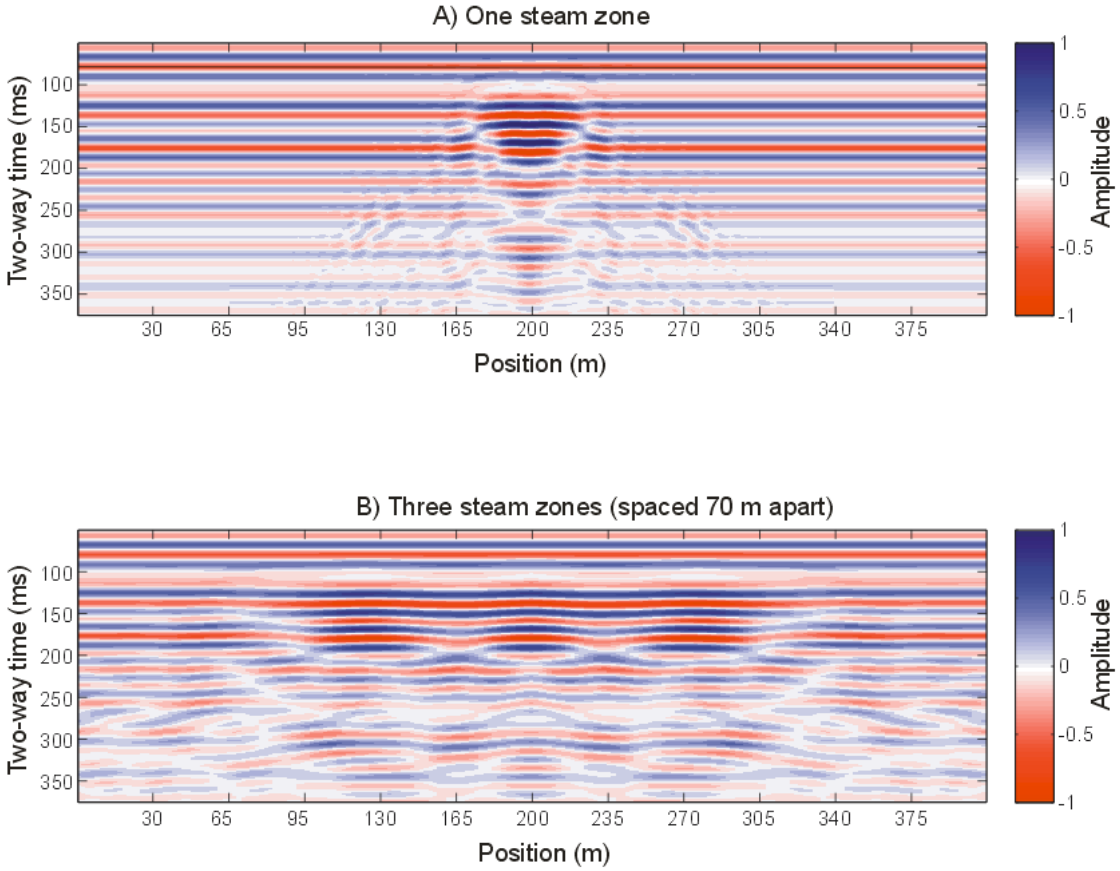

FIG. 4.14. The seismic profile generated over one steam zone (A), cannot be used as a trivial proxy for three steam zones closely spaced (B). The complicated smearing and blurring of the waveforms caused by multiple steam zones can make time-lapse interpretation problematic.

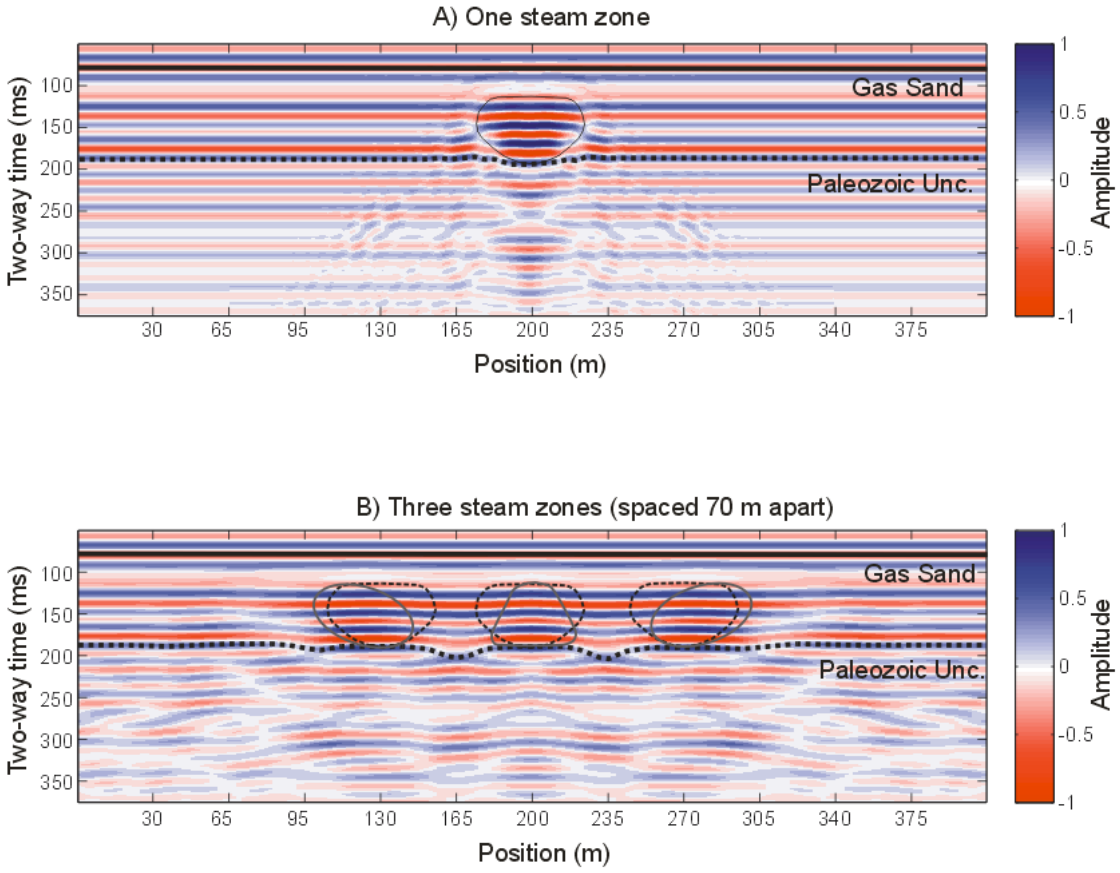

FIG. 4.15. Annotation and interpretation of key horizons and features within synthetic steam zone model. The seismic profile generated over one steam zone (A), cannot be used as a trivial proxy for three steam zones closely spaced (B). The complicated smearing and blurring of the waveforms caused by multiple steam zones can make time-lapse interpretation problematic. In this case mapping the travel-time delay on the Paleozoic Unconformity would lead to an incorrect estimate of the steam distribution, whereby the maximum pull down does not coincide with the thickest part of the steam chamber.

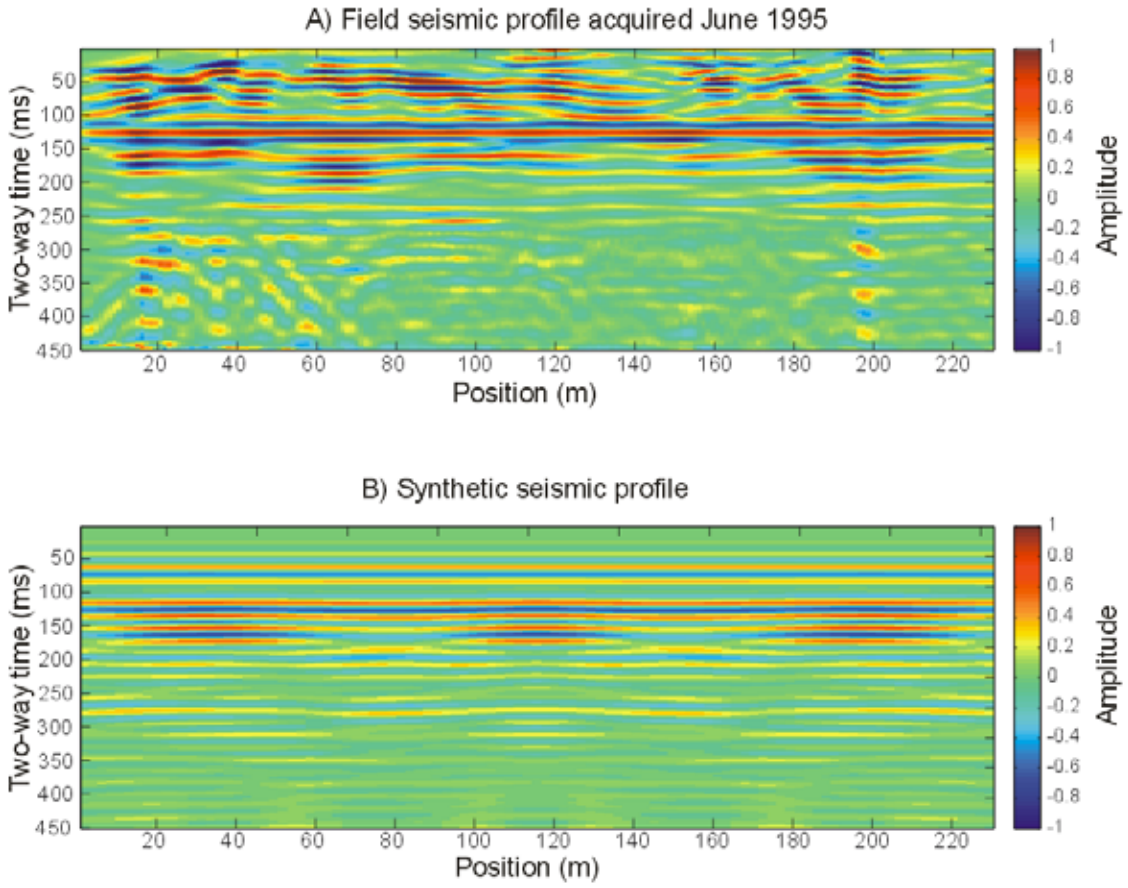

FIG. 4.16. Comparison of real seismic data collected after 3 years of steaming at UTF versus numerical seismic data of 3 symmetric steam zones. The numerical model accurately predicts the extended travel time pull-downs in undepleted reservoir between the steam zones, and this region might be erroneously be interpreted as a depleted portion of the reservoir filled with steam.

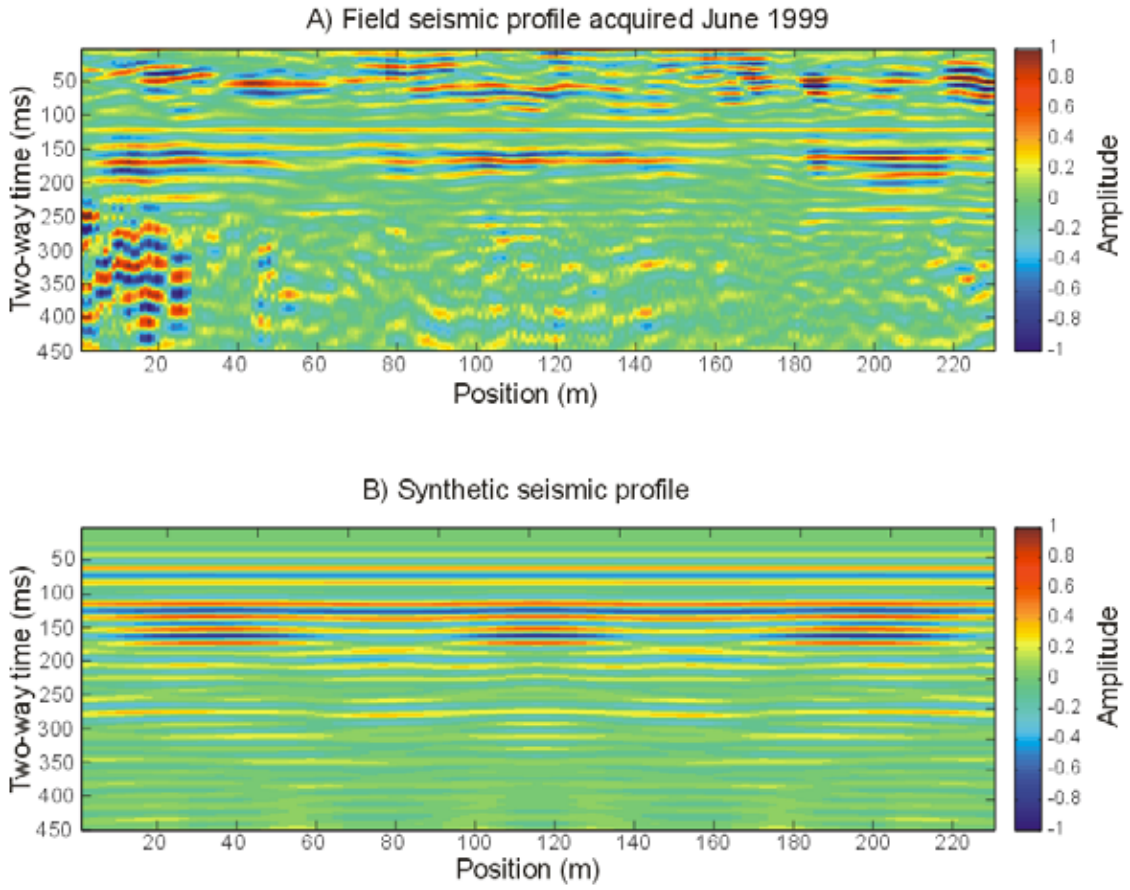

FIG. 4.17. Comparison of real seismic data collected after ~7 years of discontinuous steaming at UTF versus numerical seismic data of 3 symmetric steam zones. This 1999 data set has higher overall bandwidth and higher vertical resolution than in 1995. The numerical model accurately predicts the extended travel time pull-downs in undepleted reservoir between the steam zones, as this region might be erroneously be interpreted as a depleted portion of the reservoir filled with steam.

4.5 Discussion

The objective of this chapter was to simulate the effect of a steam chamber on surface seismic reflection data. It was shown that two-dimensional wave propagation obscures the capacity to make high resolution images of local velocity anomalies in the earth. In the absence of migration, post-stack seismic data exhibit remnant diffraction hyperbolae from steam zone anomalies. If at all possible migration algorithms should be employed when processing real field data sets. It was also shown that caution must be taken when using travel-time pull-down beneath the steam zone as a proxy for the total steam zone thickness. This is especially true when multiple parallel zones are adjacent to one another.

Although the critical limit of resolution was not investigated here, sampling the earth with midpoints spaced every 1 m along the profile was indeed sufficient to capture the anomaly from a steam zone 50 m in width. This data could be decimated in the future to ascertain the minimum CMP sample spacing (maximum trace spacing) capable of capturing this anomaly. Conventional land surveys that have 10 m or 20 m bin intervals are likely too coarse to image the steam chamber.

Given the computational expenses needed to run these synthetic experiments, these results are rather preliminary. However, the results of this simple modeling approach suggest that seismic monitoring of steam chambers is not trivial. Wave motion in real media is in many respects different from motion in an ideal acoustic solid. Effects such as wave attenuation and dispersion significantly affect the amplitude and travel time

of the wavefield. The next step is to build visco-elastic models of the subsurface and use the visco-elastic wave equation to solve this problem.

The resolution potential of seismic methods is usually determined by the half-width w, of the first Fresnel zone (e.g. Yilmaz, 1987), which is defined as

$$w = \sqrt{\frac{1}{2}\lambda z}\,, \tag{4.1}$$

with λ being the dominant wavelength of the wavelet and z the depth to the reflector. For an extremely short wavelength of 5 m and depth of 150 m from the model the width becomes w = 19.4 m. We find that our ability to resolve lateral discontinuities in the seismic data is much better than this estimate and is on the scale of only a few metres.

These simulations in this Chapter showed that seismic monitoring for SAGD programs is possible if the steam chamber has grown to a sufficient size. A 5 m wide steam zone would not be resolvable in this reservoir with significant noise levels, but it might be detectable. The simulations showed that, in theory, seismic methods should be able to distinguish between subtle changes in the reservoir over time. This type of work should be carried out prior to embarking on a multi-year monitoring program as it will expedite survey planning with regard to the logistical confines of cost, time, resource, and geological aspects. The next Chapter will correlate and contrast these modeling results with the real field surveys in more detail.

References

Chalaturnyk, R.J., Geomechanics of the steam assisted gravity drainage process in heavy oil reservoirs, Ph.D., University of Alberta, 1996.

Christensen, N.I., and H.F., Wang, 1985, The influence of pore pressure and confining pressure on dynamic elastic properties of Berea sandstone, *Geophysics, 50*, 207-213.

Eastwood, J., 1993, Temperature-dependant propagation of P- and S-waves in Cold Lake oil sands: Comparison of theory and experiment, *Geophysics*, *58*, 863-872.

Foinaven 4-D: Processing and analysis of two designer 4-Ds, pp. 1456–1459, Soc. of Expl. *Geophysics*., 2000.

Fomel, S., Landa, E., and Taner, M. T., 2007, Post-stack velocity analysis by separation and imaging of seismic diffractions: *Geophysics*, v. 72, 89–94.

Fomel, S., E. Landa, and M. T. Taner, 2006, Post-stack velocity analysis by separation and imaging of seismic diffractions: Presented at the 76th Annual International Meeting, *Soc. of Expl. Geophys*.

Li, G., G. Purdue, S. Weber, and R. Couzens, 2001, Effective processing of nonrepeatable 4-d seismic data to monitor heavy oil sagd steam flood at east senlac, saskatchewan, canada, *The Leading Edge*, *20*, 54–63.

Li, L., Z. Chen, Y. Mu, and X. Chen, 2004, 4d seismic time differences extracted from pre-stack seismic data, *J. Geophys. Eng.*, *1*, 143–146.

Miller, R. D., and Xia, J., 1998. Large near surface velocity gradients on shallow seismic reflection data: *Geophysics*, 63, 1348-1356.

Pullin, N., L. Matthews, and K. Hirsche, 1987, Techniques applied to obtain very high resolution three-dimensional seismic imaging at an athabasca tar sands thermal pilot, *The Leading Edge*, *6*, 10–15.

Rickett, J., Bandwidth-equalization and phase-matching of time-lapse seismic datasets, in *SEP-Report*, vol. 94, pp. 33–43, SEP, 1997.

Ross, C. P., and M. S. Altan, 1997, Time-lapse seismic monitoring: Some shortcomings in nonuniform processing, *The Leading Edge*, *16*, 931–937.

Strobl, R.S., Muwais, W.K., Wightman, D.M., Cotterill, D., Yuan, L.P., Application of outcrop analogues and detailed reservoir characterization to the AOSTRA underground test facility, McMurray Formation, North Eastern Alberta, Petroleum Geology of the Cretaceous Mannville Group, Western Canada, *CSPG, Memoir 18*, 1997

Theune, U., Seismic monitoring of heavy oil reservoir: rock physics and finite element modelling, Phd, University of Alberta, 2004

Wang, Z., and A. Nur, Effect of temperature on wave velocities in sands and sandstones with heavy hydrocarbons, in Seismic and Acoustic Velocities in Reservoir Rocks, edited by A. Nur and Z. Wang, vol.1 of Geophysics reprint series, pp. 188-194, *Soc. of Expl. Geophys.*, 1998.

Wang, Z., A. M., Nur, 1990, Wave velocities in hydrocarbon-saturated rocks: Experimental results, *Geophysics*, 55, 723-733.

Wang, Z, A. M., Nur, and M.L. Batzle, 1990, Acoustic velocities in petroleum oils, *Jour. Petr. Tech., 42*, 192-200.

Chapter 5

High resolution time-lapse monitoring of the SAGD process at the Underground Test Facility (UTF) site

5.1 – Experimental methodology and practical considerations

The nature of the relatively shallow target at the UTF facility poses several challenges for successful seismic imaging. The information-carrying capacity of all seismic reflection data is directly proportional to reflection-frequency bandwidth, but the use of high frequencies is especially necessary to resolve shallow reflections (Steeples, 1998).

11 2-D seismic lines were collected by the University of Alberta between 1995 and 2000 over the UTF Phase B site using a weight-drop source. The dates of each survey are shown in table 5.1. The profile was placed over the middle part of the well pairs and intersects 8 vertical observation wells as shown in figure 5.2. Although the ideal time-lapse experiment would execute each survey at even time intervals, a number of operational and external factors made this difficult. The longest time interval between surveys is 3 years and the shortest time interval between surveys is 33 days.

SURVEY	DATE
1	July 15, 1995
2	July 22, 1998
3	Aug 13, 1998
4	Oct 19. 1998
5	May 13, 1999
6	June 16, 1999
7	Aug 04, 1999
8	Oct 20, 1999
9	May 11, 2000
10	July 14, 2000
11	Oct 01, 2000

Table 5.1. Dates of repeat seismic surveys.

A single shot record is shown in figure 5.3 and highlights some of the practical challenges associated with shallow seismic surveying. 48 channels were used for the acquisition of the seismic data (except for the first survey in 1995; only a 12 channel system was used) and these channels had to be optimally spaced such that the reflections of interest were free from other sources of coherent noise. There is only a ~130 ms 'noise-free' window that exists between the near surface refractions and the high amplitude ground roll. For this reason, the offsets range selected was 48 - 142 m, which allows for high spatially sampling and the optimal capture of unobstructed signal.

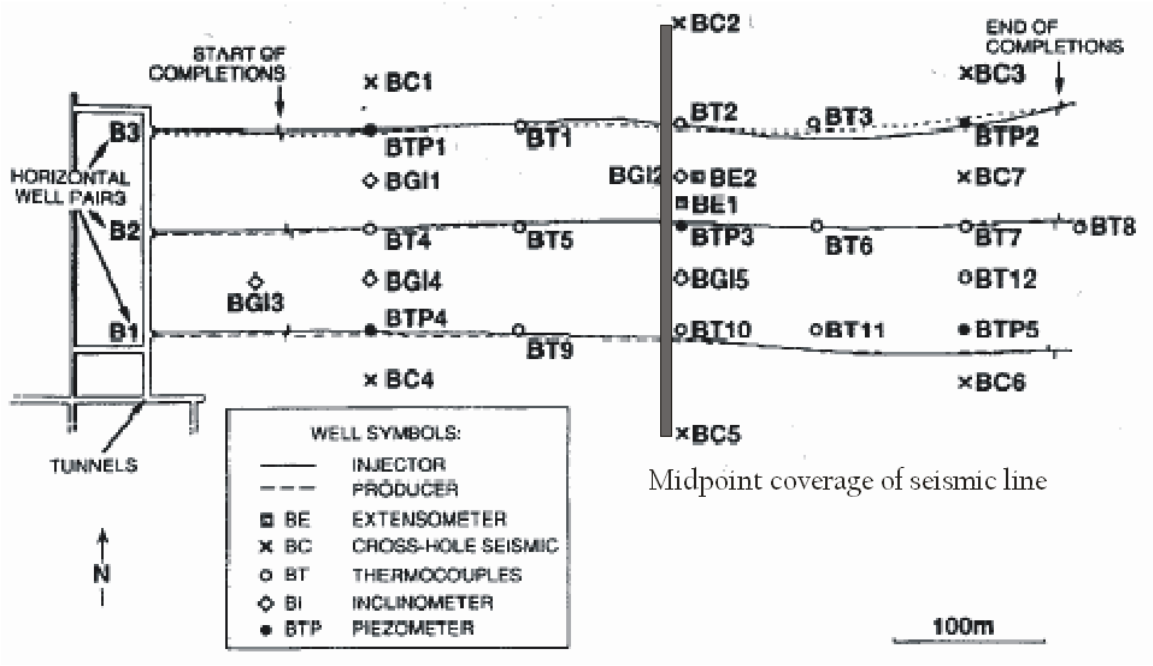

FIG. 5.2. Midpoint coverage of seismic profiles collected over the study area at UTF. Collins (1997)

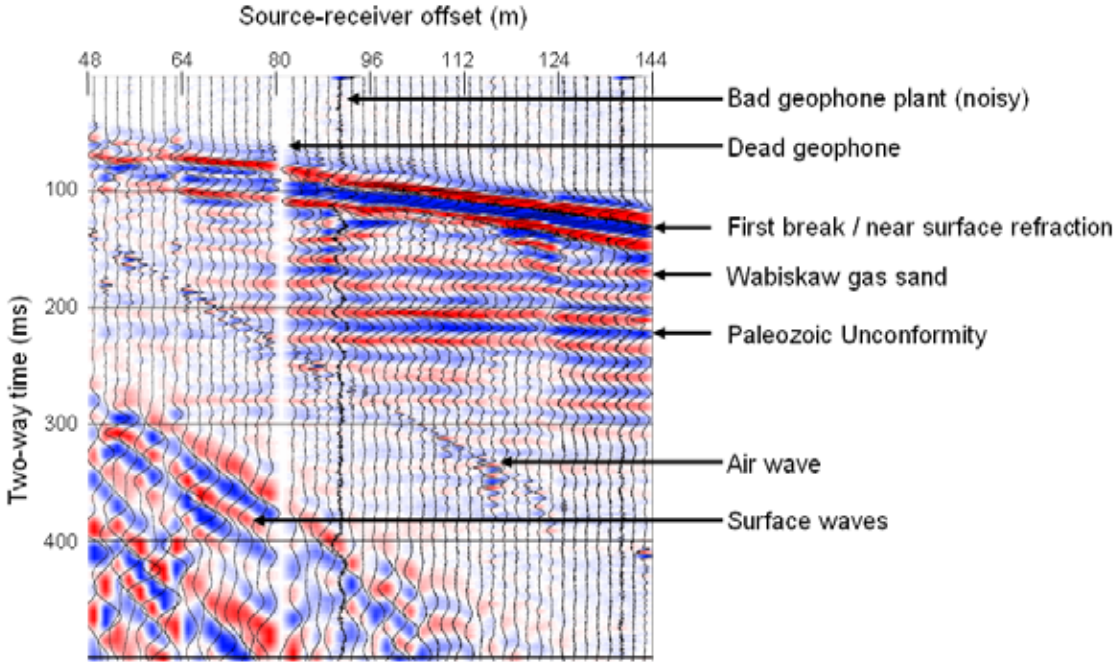

FIG. 5.3. Raw shot gather at UTF. An example of the effect of first arrivals, surface waves and air waves on the seismic reflection data. Energy arriving at times of less than 120 ms is primarily refraction energy, but some shallow reflections can be seen at short offsets. Note the lower apparent frequency and the apparent dip of the refractions. The true reflections at times between 120 and 250 ms show higher frequency and a flat structure. Data have been normalized by the mean value over each trace for display purposes in this figure.

Ground Roll

The ground roll in this data set is characterized by low frequency, high amplitudes, and low velocities. Because the ground roll in this setting tends to mask the reflection signals, it has presented a dilemma. Traditionally in shallow surveys, reflections are within 300 ms of the surface have dominant frequencies that are nearly double that of the ground roll. Ground roll can be decreased by applying frequency filtering or a combination of frequency filtering, spectral balancing, and *f-k* filtering. Minimizing ground roll by applying digital filtering assumes that the instantaneous dynamic range of the recording equipment is large enough to allow the reflected energy to be recorded and superimposed on the presence of high amplitude noise. This was not assumed in this experiment. Even using systems featuring state of the art electronics and high precision analog-to-digital conversion, reflected energy cannot always be recorded successfully (Steeples and Miller, 1998). Instead of dealing with ground roll in the processing stages, it was avoided at the acquisition stage by selecting an appropriate geophone array in the field. The first geophone was positioned such that the onset of ground roll arrived after the area of interest had been sampled. This ensured that the time window of interest was free of ground roll, and it could be removed by surgical muting.

First Break / Near Surface Refraction

Separating shallow reflections from shallow refractions can be challenging. The near surface refractions seem to have frequency content close to that of very shallow reflections. In this data, refracted waveforms change quite rapidly from mid offsets (at 48 m) to far offsets (142 m) and they slightly interfere with the reflection of interests only

at the largest offsets. This change is ubiquitous across the profile and seems to be predominantly a function of offset, but may also be controlled by variations in near-surface velocities. Also, the near surface refractions appear to have been attenuated, whereby the arrivals closer to the source have generally higher frequencies (and higher noise levels) than at farther offsets.

Air Wave

Because the data was collected with a hammer drop source, the resulting recorded air wave is minimal compared to other sources. It is characterized by high frequency, and low velocity. Note the linear move-out of ~340 m/s; the speed of sound in air in figure 5.3. This wave is easily removed using a low pass filter passing frequencies below 200 Hz.

The geophone array is not ideal in the sense that no data is collected at vertical or near vertical offset, but this is never the case in any real land survey. However, there is not a significant amount of moveout across the reflections of interest across a shot gather or CMP gather. This makes NMO correction slightly more robust because only a small correction is needed to flatten the reflections of interest. This has been the motivation behind the development of the shift-stack method carried out by Schmitt (1999), and has proved to work quite well in this situation.

5.2 – High resolution "fit-for-purpose" seismic monitoring experiment

5.2.1 Site and Survey design

It was decided that the best profile to image the steam injection process is a line perpendicular to the well pairs and expectedly parallel to the migration and expansion of

the steam chamber. Although a 3-D survey would provide a more complete picture of the subsurface, it was not feasible with the equipment, and time that was available on-site. In fact, for small scale time-lapse applications where the subsurface properties are changing relatively quickly, it may not be possible to carry out a small 3D survey more than once every few years.

The intention of this seismic experiment was to obtain close trace spacing while collecting a considerable range of source-receiver offsets in the seismic data. For costs and logistical reasons, traditional land 3-D surveys typically are collected with arrays that amount to processed data traces (or bins) that are between 10 and 25 m apart. As was shown in Chapter 4, this may be far too coarse in order to image the steam chamber. In this experiment, a CMP spacing of 1 m was obtained by shifting both shot points and receivers 2 m along the line from south to north.

5.2.2 Conventional processing workflow and practical considerations

The reflections of interest within the seismic data do not conform to a smooth hyperbolic travel-time relationship. As such, NMO-correction fails to align events at their normal incidence travel time. This has required a modification of conventional seismic processing using the NMO-method.

The processing procedure included (1) true amplitude recovery on shot records, with application of de-biasing, (2) removal of dead traces and surgical muting of ground roll noise field file by field file (figure 5.5), (3) f-k velocity filter to remove the air wave, (4) sorting of data into CMP gathers, (5) derivation of stacking velocities (NMO velocities) from semblance analysis, and (6) NMO-correction and stack or shift-stack.

The shift-stack method employed by Schmitt (1999) is preferred to the NMO-method because of the significant static problems in the data and the non-hyperbolic character of the reflections. This is due to the fact the reflections have very little curvature or moveout across the offsets that were recorded. No physical time-lapse information is thought to be obtained from semblance velocity analysis that can be interpreted in a meaningful from one survey to the next. The primary objective of flattening the reflections can be achieved with the shift-stack method and it eliminates static problems caused by a large topographic variations and velocity heterogeneities in the near surface (figure 5.6).

The shift-stack processing procedure (Schmitt, 1999) takes a minimalist approach to processing, and due to its simplistic nature, lends itself more agreeably to time-lapse analyses of multiple data sets.

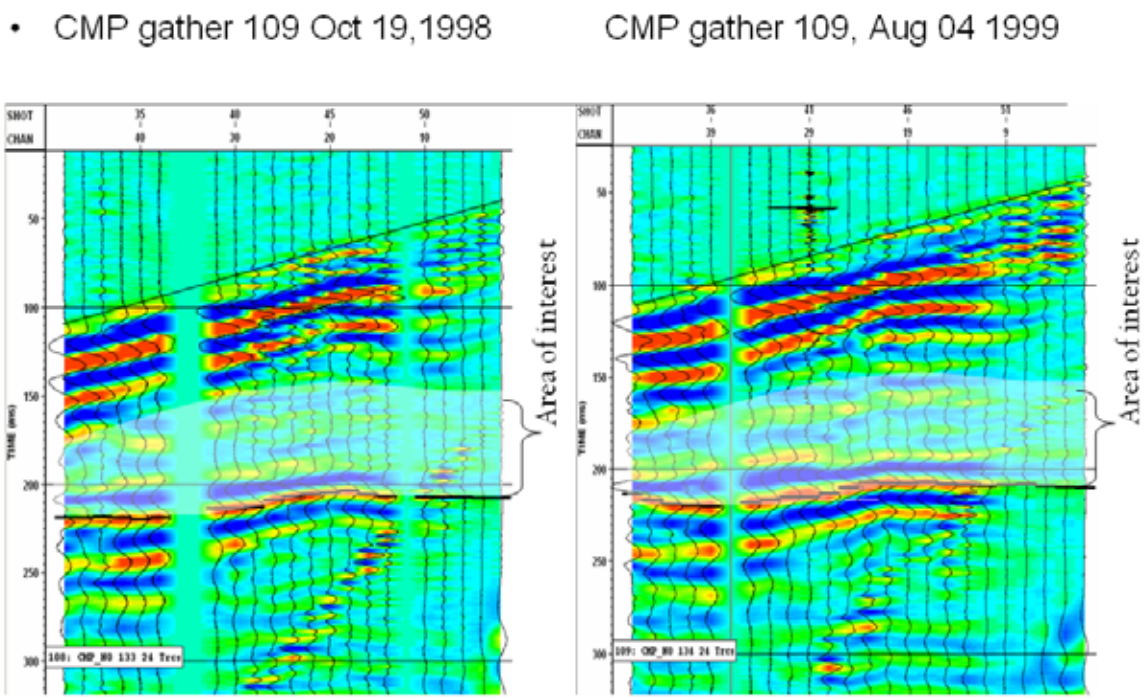

FIG. 5.4. Non-hyperbolic reflections caused by large near surface velocity variations and static shifts. NMO-correction fails to align reflection events because events do not follow smooth travel-time hyperbolae. The repeatability between these two CMP gathers (collect one month apart) is notable.

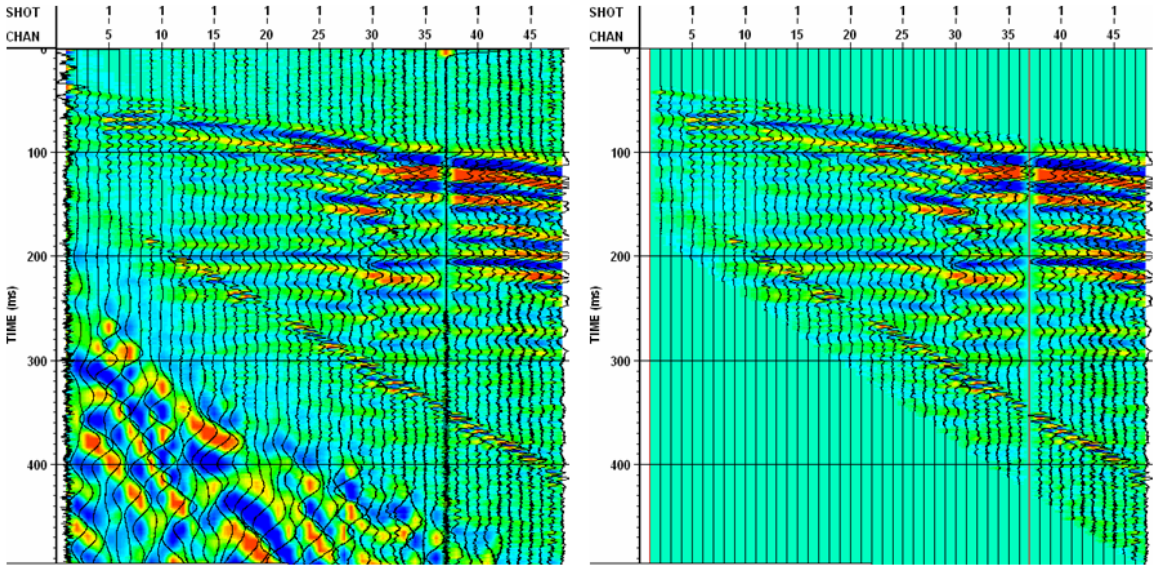

FIG. 5.5. Raw shot gather example (left) is cleaned after surgical muting and removing the bad traces (right).

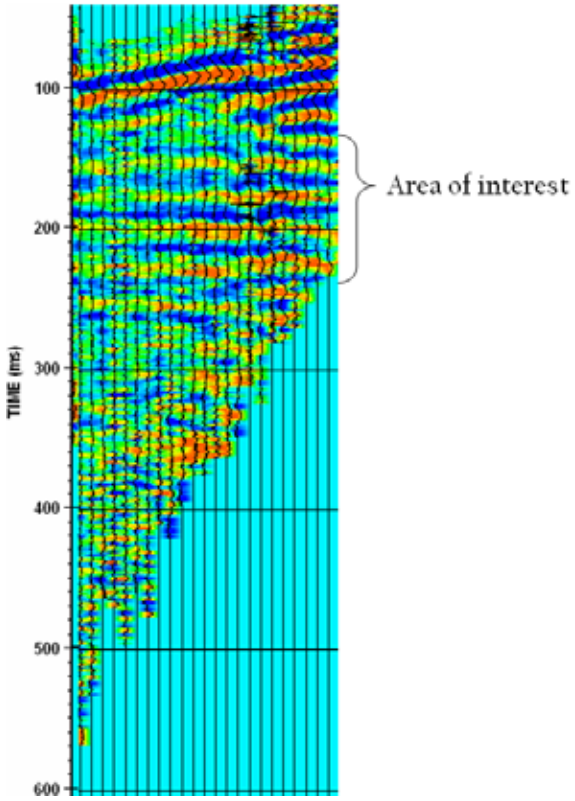

FIG. 5.6. Example CMP gather after application of shift-stack to flatten the reflections in the area of interest.

5.2.3 2D Seismic profiles

Figure 5.7 shows the processed seismic section for all 11 profiles collected between 1995 and 2000. With the exception of surveys 3 and 4 that were not carried as far to the North, the profile has been successfully repeated over a number of years. Positioning was generally within 10 cm, as verified by GPS measurements and was not investigated in a quantitative or statistical sense. Also, the hammer generated source signal was not recorded, so that source repeatability could not be investigated, although attempts to record land based source signatures have not, to our knowledge, been successful. These data show amplitude anomalies that correspond to the extent of the active steam chambers in the ground. The largest amplitude changes are found between the 3-year gap between survey 1 and survey 2, and all the other remaining surveys (3-11) undergo much more subtle changes. Of particular note are the oscillations of the middle and right steam chamber and the gradual loss of amplitude at survey 11. Also, the leftmost well pair is located at 50 m along the profile and the related seismic amplitude anomalies are certainly not symmetrical about that vertical position. In fact, it appears that the amplitude anomalies have settled only to the south.

3D volume visualization

Another way to look at more than one profile at a time is to place each as a panel front of the previous to create a 'calendar cube' of the data. In figure 5.8, such a three-dimensional representation of the 2-D time-lapse data is shown. In this image, the largest amplitudes (both positive and negative) have been rendered as translucent volumes shown in green.

Since recorded waveform amplitudes oscillate above and below zero, the zero crossings do not provide a clear picture of the energy distribution across the profile. In order to minimize this effect the Hilbert transform has been applied to the data along each trace (figure 5.9). Here, the effect of the wavelet is essentially removed whereby an 'envelope' of the seismic energy remains. The peaks and troughs in figure 5.8 have been replaced by more generalized zones of high and low amplitudes. It is proposed here that this method of visualization may be suitable for extracting detailed and quantitative time-lapse information. The bright zones in this figure serve as a proxy for the saturation and magnitude of steam in the reservoir; the brighter zones indicate a greater amount of total steam thickness. Here it seems that the area of the steam chamber actually decreases in each of the three zones between 1998 and 1999 and this could be indicative of the cessation of the process (Yee and Stroich, 2004). This is particularly evident in the middle anomaly.

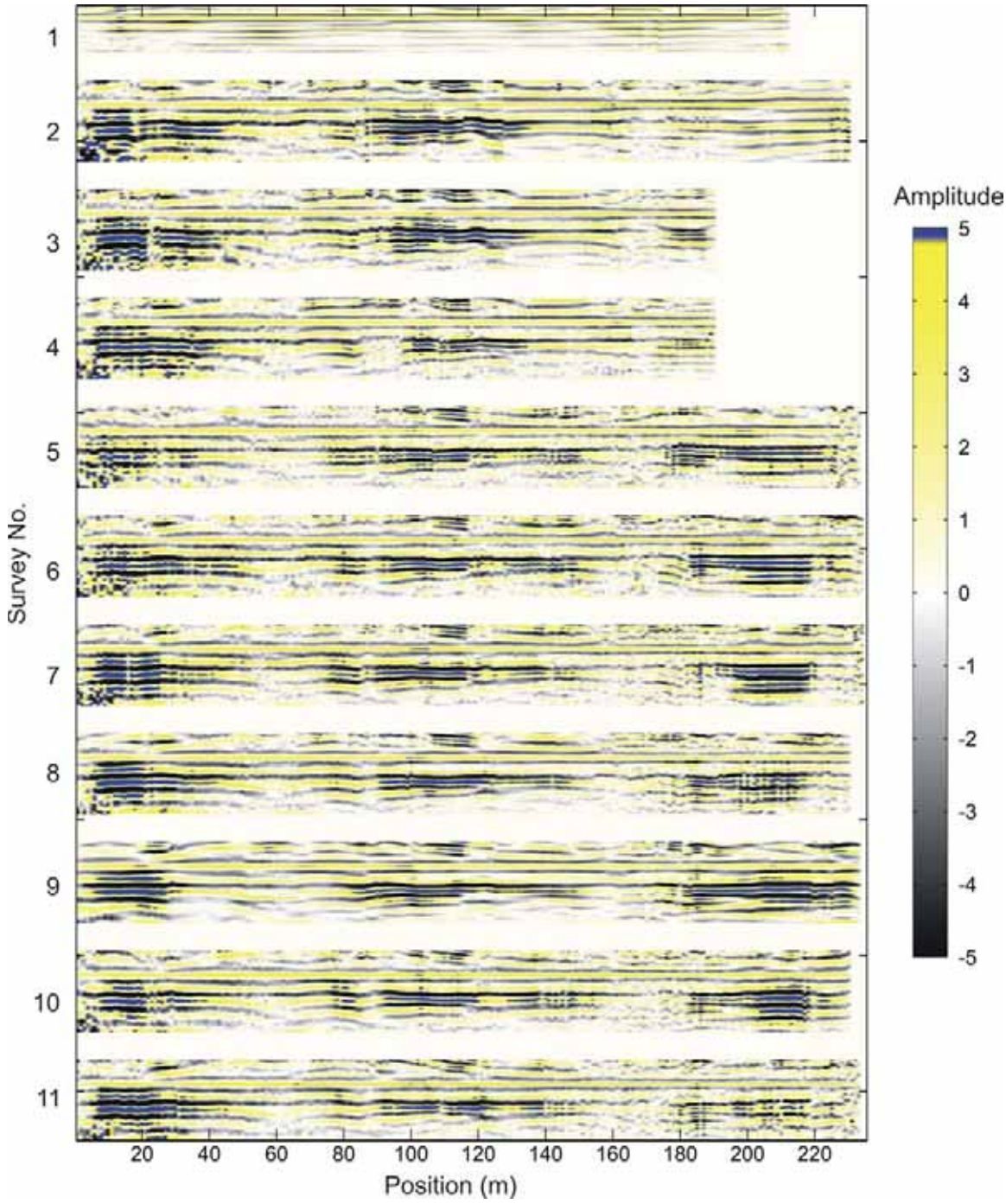

FIG. 5.7. 11 time-lapse data profiles over three well pairs at UTF. Injector / Producer well pairs are located at 50m, 120m, and 190m along the profile. The largest positive amplitudes have been colored blue and they are located at the positions of the steam zones.

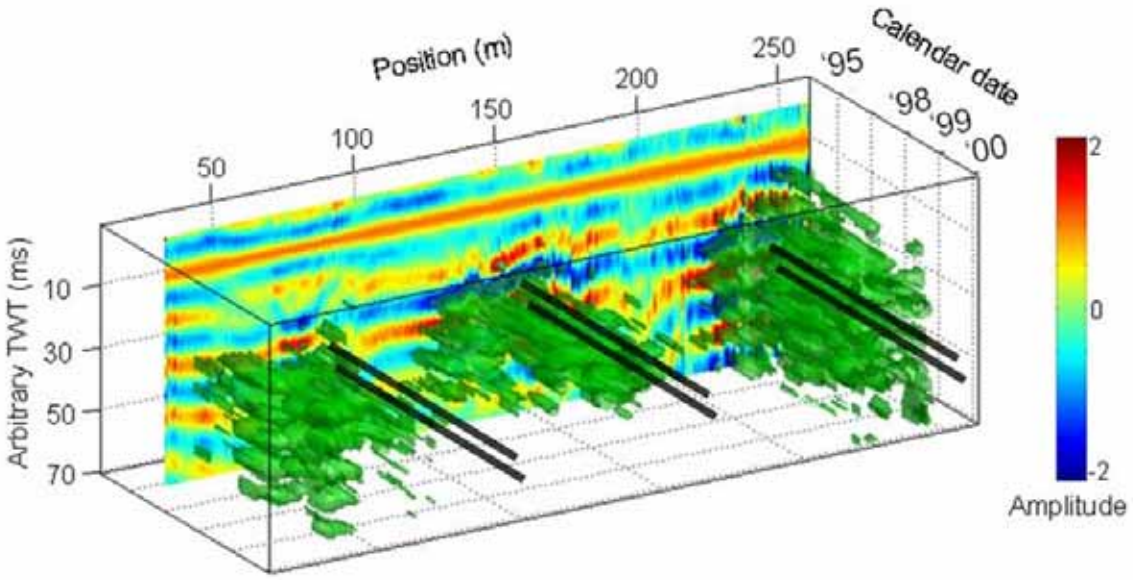

FIG. 5.8. 3-dimensional representation of repeated 2-D seismic (time-lapse) data collected over 3 steaming horizontal well pairs at UTF. Position and two-way-travel time are on plotted the x and y axes respectively, and the volume of data is given a 'depth' perspective by stacking the repeated sections along the z-axis (in ascending calendar date). The 'brightest' amplitudes (both positive and negative) have been rendered as semi-transparent '*iso-surfaces'*. These *iso-surfaces* are thought to be indicators of the lateral extent of the steam chambers. The reverberations are proportional to the magnitude of steam in the reservoir and coincide with the modeled reverberations in Chapter 4. The approximate location of the well pairs are indicated by the black lines, however their size and vertical separation are not to scale.

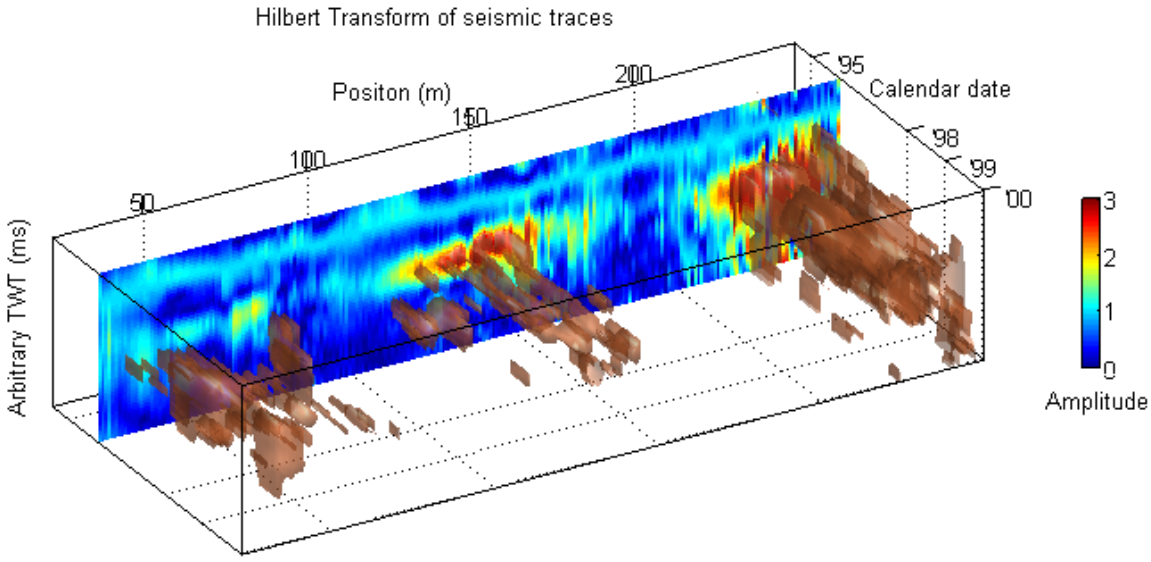

FIG. 5.9. Energy envelope generated by trace by trace Hilbert transform of data in figure 5.8. Largest values are rendered in brown. Well pairs are located at 70 m, 150 m and 220 m along the position axis.

5.2.4 Attribute analysis

Performing a specific calibration from one or several seismic attributes (such as amplitude, travel-time, frequency, or phase) to one or several reservoir attributes (such as steam content, temperature, pressure, or viscosity) is a difficult task. This is due to the complicated path of the reflection amplitudes and the band limited nature of seismic body waves. A seismic model may indicate that a certain amount of steam in the reservoir may contribute to a certain travel-time delay; however we have shown in Chapter 4 that the coherent events upon which travel times are picked can be distorted or smeared as the scale of the steam zones are close to that of the insonifying wavelengths. The problem arises from the fact that travel-time and amplitude are essentially two separate seismic attributes, and they are traditionally measured independently, yet they inherently tune together with regards to the small velocity anomalies being studied here. At this time

there is no simple rule that can be assigned pertaining to the conversion between band-limited seismic attributes and the sought after reservoir parameters.

The onset of appreciable changes in seismic response occurs once steaming has established heat communication between the injector and producer wells. The seismic anomalies produced by the steam are about 50 m wide and stand out against the otherwise homogeneous image of the background reflections. Just as was demonstrated in Chapter 4, there is not a significant time delay due to the presence of steam, whereas the prominent response is in strong variation in amplitudes. The Hilbert Transform of the seismic data provides sharper cut-offs between high and low amplitudes and it appears that the onset of steam occurs much later for the northern-most well pair. This information was not clear with the standard seismic image.

5.2.5. Attempts at unconventional processing

Careful equipment installation and data acquisition allows data reproducibility and permits time-lapse analysis on a trace by trace basis. In this case, data has been sorted into constant offset gathers in order to, (1) examine the continuity and variability of reflections at a specific offset, and (2) investigate pre-stack amplitude calibration based on the near surface refraction (first-breaks).

Beaty et al. (2000) performed a series of small scale surface wave experiments and demonstrated that Rayleigh waves can be highly repeatable over time and are predictable in the same location. At the UTF site however, the surface waves are not consistent from one survey to the next and this could be due to either inconsistencies with the hammer source, the degree of coupling with the ground, or variations in temperature,

moisture content, and other seasonal changes in the weathering layer at the surface. As such, surface waves could not be used for amplitude calibration at this site.

An alternative approach to calibrating amplitudes is normalized the seismic traces based on the near surface refraction or first-breaks in the data. Interestingly, the first-break refraction arrivals are very well-behaved and for the most part, are repeatable from one survey to the next. Figure 5.10 shows a constant offset stacked profile (with source-receiver offsets of 100 m) for three different calendar times. Notice how the first-breaks are quite variable from South to North along each profile however the character of a single trace location is impressively reproduced for these three data sets. The remaining 8 data sets did not show this remarkable similarity and as such, amplitude calibration could not be performed equally to all 11 profiles. For some reason, the near surface refractions in some of the data were not systematically repeated at all offsets. Again, this may have been due to inconsistencies with the weight drop source source to create the signal or some other systematic reason.

The waveforms associated with the near-surface refractions on a constant offset gather (COG) show extraordinary repeatability at different calendar times which puts great confidence in the integrity of the signal at later travel times. The near surface is highly variable from south to north, however, the near-surface refraction provides a robust marker by which individual pre-stack traces can be normalized prior to stack or other imaging processes. Single-fold data may be a cost effective alternative which can be acquired much more frequently than expensive multi-fold 3D or 2D data sets currently employed over thermal recovery projects. Figure 5.11 and 5.12 illustrate the repeatability issue and show that both reservoir changes and near surface changes can cause a time-

lapse effect. Without the appropriate geotechnical measurements it is difficult to say whether the near surface variations are actually caused by an underlying expansion and upheaval of the reservoir zone, or if these are noise problems associated with the weathering layer changing over time.

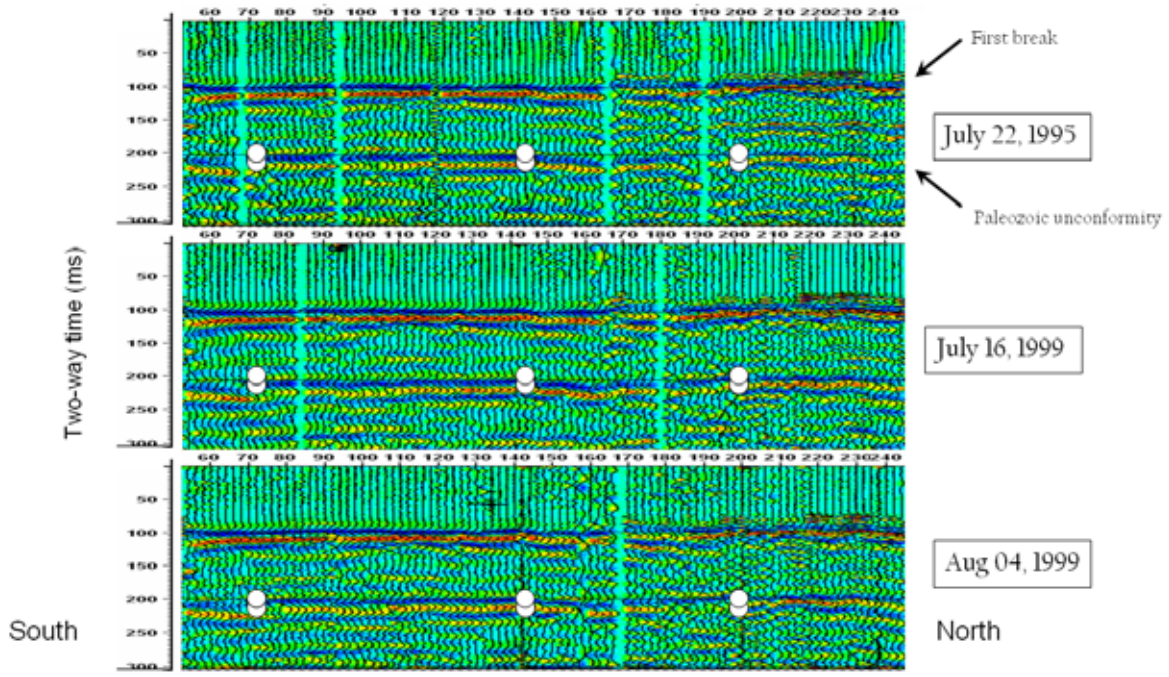

FIG. 5.10. Single-fold data showing constant offset gathers (100 m source-receiver separation). Gaps show bad channels where the traces have been removed, and although there is a large amount of "noise", reflections and refractions are clearly seen and methodically reproduced at different dates. The first arrival (near surface refraction) occurs at ~110 ms for all traces, and the subtle variability of the waveform character from south to north is systematic from one survey to the next.

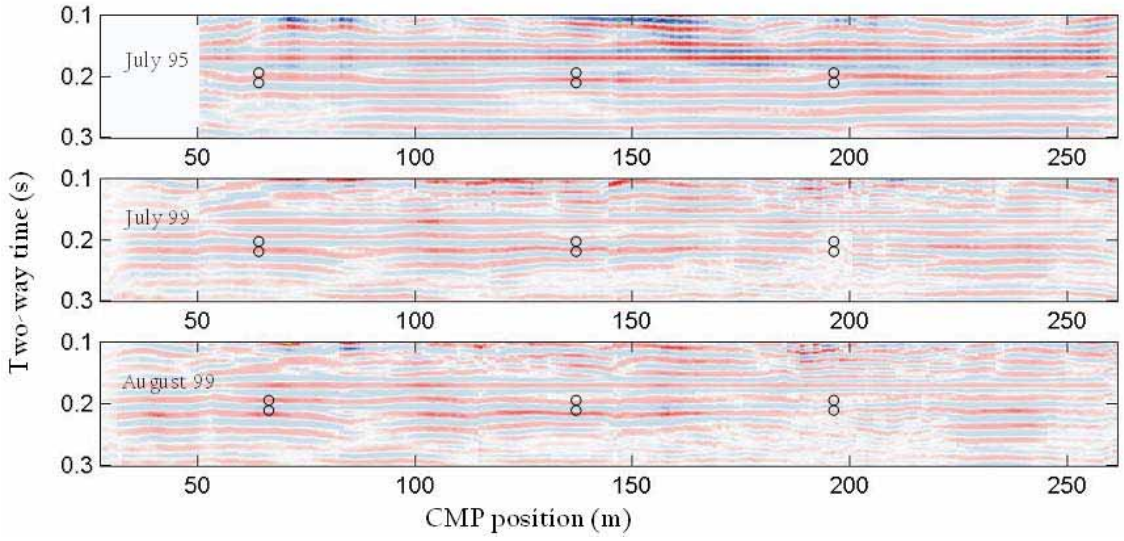

FIG. 5.11 Constant processing and amplitude normalization on the Wabiskaw gas sand for 3 data sets.

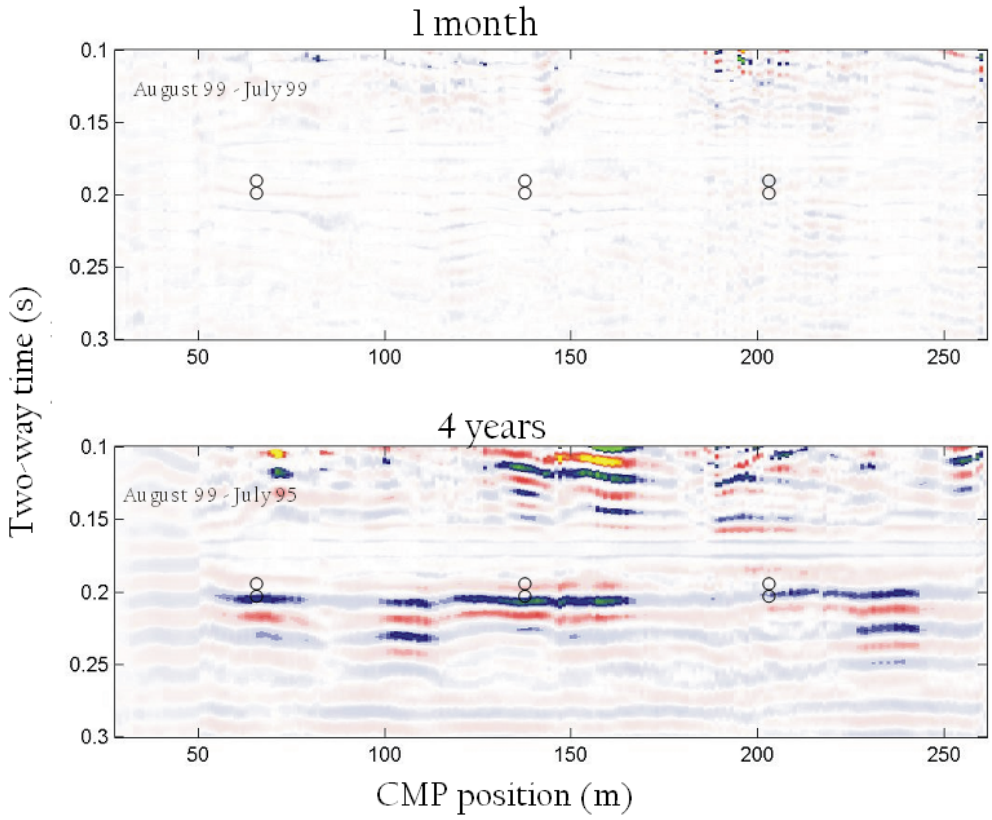

FIG. 5.12. Seismic time lapse difference over one month (top) and 4 years (bottom).

5.3 Correlating discrete time-lapse seismic data with insufficient reservoir data

The results from the rock physics and numerical seismic simulations in Chapter 3 and 4, respectively, suggest that the feasibility of seismically monitoring steam zones does not only depend on the mechanical related changes associated with steam injection, but also on the scale of the anomaly itself. The velocity models constructed in Chapter 4 were inherently simplistic due to a lack access to the true temperatures and pore-pressures in the borehole as a function of time. Presumably, a better match between the synthetic and real data sets could be obtained if the true temperature and pore pressure

profiles were used to construct a synthetic seismic profile for every step through time. At this writing, unfortunately, these data remain unavailable. Furthermore, the field data was not collected at constant increments say, every 6 months, and that makes extracting time-lapse information more challenging.

Due to a number of confidentiality and proprietary prohibitions, the set of engineering measurements, production and injection data, and monitoring instrumentation has not yet been released by the site operators. Thus, at this time, it is nearly impossible to correlate the extensive seismic observations with the suite of in-situ measurements that were collected such as: temperature, pore-pressure, mechanical strain, and surface heaving. An ideal workflow would involve generating a synthetic seismic data set derived from the precise borehole measurements matching the date at which each field survey was collected. Shy of this ideal situation, we are left to make inferences based on existing published knowledge about the UTF Phase B process and can piece together coarse observations from comments and statements in the literature. The next section will discuss some major events in the life cycle of phase B and their timing in relation to our discrete seismic measurements.

A Brief and Incomplete history of UTF Phase B production

Unfortunately, the earliest seismic survey was collected in July 1995 which was in fact, 3 years after steaming began in 1992. In most SAGD projects, an initial soaking phase occurs (between 20 and 60 days) in order to establish heat communication between the wells. Steam is injected into both the injection well and the production well at high pressures in order to produce a melted pathway to promote the drainage of bitumen and the expansion of the steam chamber.

In an update report from O'Rourke at al. (1999), it was stated that, "after producing for two years at peak rates exceeding 300 t/d [tonnes per day] these underground wells started to decline at the end of 1995. As of March 1997, [the] three well pairs have produced about 380,000 tonnes (or 2.4 million barrels) of bitumen. . . recovery to March, 1997 is ~55% of OOIP [original oil in place] in the pattern. Because of better than expected performance, the shut in of steam injection has been postponed from August 1996 to the end of 1997."

This report also mentioned: "the plant plans to close or reduce steam to Phase B by early 1998 . . ., because the steam to oil ratio (SOR) will rise as high as 3.5 in which time it will be more economic to put this steam into new well pairs." There is no telling if this did in fact happen, but if it did, then every seismic survey collected after this time would be sampling the reservoir during a period of shut down or cooling. Beginning in April 1998 a small amount of natural gas was added continuously to the steam injection (Yee and Stroich, 2004) in order to sustain high reservoir pressure to continue bitumen production. With the implementation of this gas injection technology into the reservoir system it is highly complicated and unlikely that seismic data will be able to reasonable predict the steam zones due to these secondary effects. At this point, the reservoir material has been so completely altered from its original state, it is nearly impossible to estimate its seismic and mechanical properties. Temporary periods of shut-in (discontinued steaming) correspond to instantaneous drops in the amount of bitumen being produced. Surely, the shut-off and ramping-up of steam injection over time invokes a complicated history of strains on the oil sand that is too difficult to predict. It may be feasible to comprehend the effect of simple fluid substitution in the reservoir, but

the real case likely consists of transient oscillatory interactions of fluctuating fluid pressures and volumes. Furthermore, engineering models estimate that once steaming has been terminated, ~70% of the heat still remains in the reservoir (O'Rourke et al., 1999). The effects of conduction might be larger than initially thought and perhaps the whole reservoir system today is depleted, partially depleted, or partially molten. The seismic amplitude anomalies associated with the 3 well pairs do not seem to be connected to each other, which suggest that there has not been steam leaked between steam zones. Such steam break-through, from one steam chamber into the other, would cause a temporary disruption in the pore pressure in the injection well and could be monitored accordingly.

The efficient recovery of all the stored heat will have a substantial impact on the overall energy budget and success of the process. It is not yet fully understood how to properly wind down these thermal recovery projects in order to recover the heat stored in the reservoir and ideally collect additional bitumen from secondary recovery process. This seems not to have ever been considered. For the seismic monitoring experiment, the last 10 seismic surveys may be poised to monitor the winding down of the process, rather than the onset of steam injection into a virgin reservoir, and would be surveying the combined rock physical changes imposed by sudden pressure changes (figure 5.12) and subsequent gas injection. With this in mind, the amplitudes falling off during the later surveys in 1999 and 2000 may represent the steam zone shrinking in size. How a steam zone shrinks is not well understood, but it may have to do with (1) the cooling of the reservoir, (2) the condensation of steam on the periphery, (3) the relaxation of pore pressure induced weakening of reservoir frame modulus, and (4) the gravitational flow of

water to the bottom of the reservoir. More studies are needed to model the rock physical changes associated with the cooling down and later stages of the SAGD process. Such work would allow operators to target zones of untouched reservoir after the process has ended.

5.4 Discussion

The ideal case for monitoring steam injection would be to have continuous and constant injection rate without interruptions or shut-ins. It is challenging enough to estimate the rock properties changes within oil sands material during steam substitution let alone taking into account the stresses and relaxations of episodic and intermittent steam injection. In the field however, operational changes and disruptions are bound to occur and may take precedence in light of adhering to ideal and stable conditions for reservoir monitoring. For this reason, it is thought the seismic data collected at UTF is insufficient at detecting weekly or daily invoked rock property changes imposed by engineering operations at Phase B. In the future, seismic monitoring studies need to be synchronized with the operations of the SAGD process as much as possible, and operational tinkering; shutting in steam, varying the rate of steam injection, etc., should be kept to a minimum in order to reliably predict the reservoir changes between surveys. This can only be accomplished if optimal production parameters are known ahead of time; many of the challenges associated with UTF was that it was the first full-scale test facility of its kind, and supposedly a variety of enhanced oil recovery methods were tested which results in complicating and contorting of the reservoir rock properties to

oblivion. Greater communication between the engineering and the geophysical studies could have assisted both greatly.

Qualitative time-lapse interpretation is possible for all three well pairs along the profile. It is anticipated that a 3-D survey of the same spatial sampling would allow for a concise delineation of the volume and shape of the depleted zones. Significant change in amplitude and instantaneous frequency is observed in the data and travel-time pull-down is not as large as originally expected for such a large decrease in velocity. The frequency variations can be explored in further studies with viscosity and attenuation measurements and modeling. Interpretations of these attributes remain highly ambiguous due to an incomplete record of the historical variations in physical properties over the life of the project, however there is huge potential to use this type of surveying to track the evolution of fluids in the subsurface over time.

Obviously a single chamber would be easier to monitor than 3 or 4 adjacent zones. There may be a time in which injector boreholes are inserted perpendicular to production boreholes to establish a 3D drainage mesh opposed to independent cylindrical chambers (M. Hall, 2007, personal communication).

References

Beatty, K., 2000, Determination of near surface variability using Rayleigh waves, M.Sc. Thesis, University of Alberta.

Evison , F. F., 1952, The inadequacy of the standard seismic techniques for shallow surveying, *Geophysics*, 17, 867.

O'Rourke, J. C., Begley, A. G., Boyle, H. A., Yee, C. T., Chambers, J. I., and Luhning, R. W., 1999, UTF Project Status update, May 1997, *Journal of Canadian Petroleum Technology*, 38(9), 44-54.

Saatçilar, R., Canitez, N., 1988, A method of ground-roll elimination: *Geophysics*, 53, 7, 894-902.

Steeples, D. W., 1998, Shallow seismic reflection section – Introduction: *Geophysics*, 63, 4, 1210-1212.

Steeples, D. W., and Miller, R. D., 1998, Avoiding pitfalls in shallow seismic reflection surveys, *Geophysics,* 63, 4, 1213-1224.

Varela, O., Torres-Verdin, C., Sen, M., Roy, I., 2006, Using time lapse seismic amplitude data to detect variations of pore pressure and fluid saturation due to oil displacement by water: a numerical study based on one-dimensional prestack inversion, *Journal of Geophysics and Engineering*, 3, 177-19

Yee, C., and Stroich, A., 2004, Flue gas injection into a mature steam chamber at the Dover project (formerly UTF), *Journal of Canadian Petroleum Technology*, 43, 54-61.

Yilmaz,O., 1987, Seismic data processing: Investigations in geophysics, 2, Soc. Expl. Geophys.

Chapter 6

Conclusions

Thermal enhanced oil recovery projects are intricate systems whereby old and stable natural earth materials are abruptly altered and changed by engineering processes. Even drilling a well into a reservoir invokes a strain on the surrounding rock, and a given piece of reservoir material is bound to experience a complex array of physical and chemical changes corresponding to each step in the process. Geophysicists can take advantage of these changes by measuring their effects on seismic reflections over a period of time. It is imperative for operators and geoscientists to synchronize their specialties in order to maximize the efficiency of the processes and add value to the life of these projects.

Chapter 1 - was a review of the rock physics relationships that are relevant to seismic exploration and how rock physics can provide a link to reservoir parameters such as porosity, saturation, pore pressure or temperature. The mechanics of the SAGD process was also described in detail as it relates to the deformation and alteration of the physical properties in the reservoir.

Chapter 2 – explored the variety of tools and measurements available in order to characterize oil sand material and its prominence in its geologic environment. Through cross-plotting borehole derived elastic properties, oil sand reservoir can be uniquely

identified apart from mudstones, shales and other lithologies. The ability to discriminate between different facies types within the McMurray formation motivates adapted inversion algorithms that allow spatial mapping of facies distributions along seismic lines. This has been in practice for some time within this part of the world and it is shifting the way in which geophysicists use seismic data. No longer does an interpretation involve abstract seismic attributes such as travel-times and amplitudes of peaks and troughs, but can now involve more intuitive geological and petrophysical parameters that describe earth materials. The concept of elastic impedance and shear wave elastic impedance variations as a function of angle provides another useful tool for discriminating oil sands material from other facies. The remaining challenge is to extend this information beyond the borehole and extrapolate these attributes between wells through seismic inversion schemes.

Chapter 3 – investigated the rock physics of steam injection into the oil sands reservoir. Due to the unconsolidated mineral grains, the fluid substitution problem cannot be addressed with tradition Biot-Gassmann theory and was modified by incorporating a pressure dependence on the rock frame. When a pore pressure-dependant frame bulk modulus is incorporated into the fluid substitution calculations, the resultant material is elastically weaker than if a rigid frame is considered. Ternary diagrams were helpful in exploring the range of elastic properties that exist for all the possible saturation combinations of the three component (oil, water, steam) pore fluid for a variety of pore pressure and injection temperatures for steam. The product of these detailed calculations is a descriptive understanding of the seismic properties of oil sands material subjected to the steam injection.

Chapter 4 – takes the results of Chapter 3 and assembles synthetic seismic experiments to investigate the seismic footprint left by a steam anomaly. Seismic processing and imaging discovered that idealized steam zones behave like scattering features and a number of attributes and signals associated with this phenomenon may be useful for quantitative time-lapse interpretation

Chapter 5 – presented the processing, analysis, and results of the high resolution time-lapse seismic experiment collected at the Underground Test Facility. In many ways the amplitude behavior, frequency, and travel-time behavior of the steam zone anomalies match the observations from the numerical model, but the real data was burdened with near surface variations, low bandwidth, higher noise levels, and source "un-repeatability" that limit the utility of all 11 profiles. In light of these challenges, the seismic anomalies associated with steam zones are extremely pronounced and any adequately sampled monitoring experiment will be able to track the general movement of steam and delineate the expanding boundary of the depleted oil zone throughout time.

The cumulative infrastructure being installed to exploit the Athabasca oil sands ranks as one of the greatest engineering feats in the history of the mankind. As the exploitation of oil sands resources continues to ramp-up in Western Canada, monitoring programs are going to be deployed in a more systematic fashion over the life of a steam injection project. Time-lapse signals can be dramatically improved by permanently installing sources and receivers and would essentially eliminate equipment set up time between surveys. In practice, it is difficult to acquire an extensive 3D survey, process the data and interpret the results in less than one year. More automated workflows will be

adopted in the future to provide information in a more timely fashion to drive "real-time" operational decision making.

Another key proponent of time-lapse seismic in the oil sands lies in the area of contamination monitoring. A large freshwater aquifer overlies the McMurray Formation in much of Northern Alberta and it could be compromised if the reservoir seal is breached. In this respect, reservoir surveillance does not only have economic implications, but may prevent serious societal and environment catastrophes.

In the future, hybrid version of thermal and chemical solvent aided recovery processes will evolve to match the expect growth and demand for this resource. As SAGD technology improves, and geophysical inversion techniques provide more accurate predictions of the subsurface geology, time-lapse monitoring within the oil sands will shift focus away from the start-up phase and more study will be done on the cooling-down phase of projects. Study of subsurface biodegradation of crude oil and the nature of the deep subsurface biosphere raises the possibility that, if it can be accelerated, natural microbes could provide methane, or even hydrogen, from spent oil fields (Jones et al., 2008). Although this technology is still speculative, it could provide methane or hydrogen (fuels that are much preferable to coal and heavy oil) without major changes in the infrastructure or supply chain systems already established by the petroleum industry.

References

Jones, D., Head, I., Gray, N., Adams, J., Rowan, A., Aitken, C., Bennett, B., Huang, H., Brown, B., Oldenburg, T., Erdmann, M., Larter, S., 2008, Crude-oil biodegradation via methanogenesis in subsurface petroleum reservoirs, *Nature*, 451, 176-180.